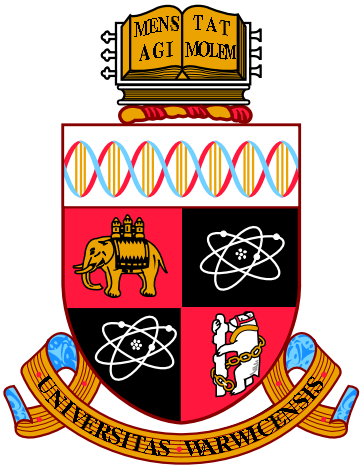

Development of Piezoelectric and Electrodynamic Flexural Transducers for Air-Coupled Ultrasonics

by

Tobias Johan Robert Eriksson

Thesis

Submitted to the University of Warwick

for the degree of

Doctor of Philosophy

Department of Physics

September 2016

THE UNIVERSITY OF WARWICK

Contents

List of Tables

List of Figures

Acknowledgments

I would like to thank Professor Steve Dixon and Dr. Sivaram Ramadas for their supervision and continuous support throughout my PhD. A big thank you also to Dr. Rachel Edwards, who first suggested doing a summer project in the ultrasound group during my undergraduate studies.

I would also like to acknowledge the entire ultrasound group. Special mentions go to Kevin McAughey for making me a part of the group when I first started, Andy Clough for the cricket results, Sam Hill for passing on his circuit marking skills and for helping me keep up my caffein level, Mike Laws for all our happy travels across the world, Matt Clough for the terrible puns and for getting all the obscure movie references, and Claire Thring for the rock climbing.

Finally I would like to thank my parents and my wonderful wife Alexandra, who has stood by me through all the hard work.

Declarations

I declare that the work presented in this thesis is my own except where stated otherwise, and was carried out entirely at the University of Warwick during the period between September 2012 and September 2016, under the supervision of Prof. Steve Dixon. The research reported here has not been submitted, either wholly or in part, in this or any other academic institution, for admission to a higher degree. Parts of this work have appeared in journal papers and conference proceedings, listed below.

Peer-reviewed journal articles:

- T.J.R. Eriksson, M. Laws, L. Kang, F. Yichao, S.N. Ramadas and S. Dixon, "Experimental evaluation of three designs of electrodynamic flexural transducers," *Sensors* **16**(9), 1363, 2016.
- T.J.R. Eriksson, S.N. Ramadas and S. Dixon, "Experimental and simulation characterisation of flexural vibration modes in unimorph ultrasound transducers," *Ultrasonics* **65**, 242–248, 2016.
- O. Trushkevych, T.J.R. Eriksson, S.N. Ramadas, S. Dixon, R.S. Edwards, "Ultrasound sensing using the acousto-optic effect in polymer dispersed liquid crystals," *Appl. Phys. Lett.* **107**(5), 054102, 2015.

Conference proceedings (reproduced in Appendix A):

- T.J.R. Eriksson, S.N. Ramadas, A. Unger, M. Hoffman, M. Kupnik and S.M. Dixon, "Flexural transducer arrays for industrial non-contact applications," in 2015 *IEEE Int. Ultrason. Symp.*, pages 1–4, oct 2015.

- T.J.R. Eriksson, S.N. Ramadas and S. Dixon, "Metal cap flexural transducers for air-coupled ultrasonics," in *41st Rev. Prog. QNDE*, pages 1287–1291, Boise, jul 2015.

- T.J.R. Eriksson, M. Laws, S.M. Dixon, and S.N. Ramadas, "Air-coupled flexural electrodynamic acoustic transducers," in 2014 *IEEE Int. Ultrason. Symp.*, pages 1021–1024, sep 2014.

- T.J.R. Eriksson, S.N. Ramadas and S. Dixon, "Flexural mode metal cap transducer design for specific frequency air coupled ultrasound generation," in 2013 *IEEE Int. Ultrason. Symp.*, pages 1602–1605, jul 2013.

Abstract

Phased array ultrasound transducers could offer significant benefits over single element transducers in flow metering technology. By steering the ultrasonic beam transmitted through the flow, a single pair of phased array transducers have the potential to replace several pairs of traditional single element transducers. A first step in researching the potential for phased array transducers in flow meters is to investigate a suitable array element.

Flexural ultrasound transducers use the bending modes in a thin plate to generate ultrasound waves in low impedance media, such as liquids and gases. The behaviour of piezoelectric flexural transducers was studied using theoretical modelling, finite element (FE) modelling and experimental techniques. Some focus was put on characterising the passive layer of the transducer, which was shown to be largely responsible for the flexural behaviour. That is, the dimensions of the passive layer largely determined the resonance frequencies of the flexural vibration modes of the transducer. Also, the viability of flexural transducers for flow applications was assessed.

A new method of constructing air-coupled ultrasound phased array transducers was suggested. A 3×3 array was constructed and tested. The individual elements of the array behaved as single element flexural transducers, but the system as a whole could be improved to allow for better beam shaping.

A novel electrodynamic flexural transducer (EDFT) for air-coupled ultrasonic transduction without use of piezoelectric materials was proposed, developed and experimentally tested. The transducer combines the contactless coupling method

used by electromagnetic acoustic transducers (EMATs) with the flexural vibration modes of a thin plate to transmit and receive ultrasound waves in air. The output pressure of the transducers was high, with SPLs over 100 dB, but the sensitivity was low compared to piezoelectric transducers.

Abbreviations

ACU	Air-Coupled Ultrasonics
CMUT	Capacitive Micromachined Ultrasonic Transducer
CW	Continuous Wave
EDFT	Electrodynamic Flexural Transducer
EMAT	Electromagnetic Acoustic Transducer
FE	Finite Element
FWHM	Full Width at Half Maximum
NDT	Nondestructive Testing
PMUT	Piezoelectric Micromachined Ultrasonic Transducer
PZT	Lead Zirconate Titanate
SNR	Signal to Noise Ratio
TOF	Time of Flight
TX-RX	Transmit-Receive

Chapter 1

Introduction

Flow measurements are important in different industries, for example in the oil and gas industry for measuring production volume. Ultrasonic flow meters can be used to measure volumetric flow rate by measuring the time of flight of waves traveling at an angle to the flow upstream and downstream between pairs of transducers. To get an accurate value of flow rate many pairs of transducers with different paths through the flow are used. It could be advantageous to replace these multiple pairs with a single pair of phased array transducers. The phased array transducers have many individual elements of ultrasound transceivers and would be able to steer the ultrasonic waves, which enables them to perform the tasks of multiple normal ultrasound transducers. Hence a single pair of phased array transducers could sample the flow along many different paths. Fig. 1.1 shows a simplified ultrasonic flow measurement setup, with two phased array transducers used to transmit and receive waves along two different paths through the flow.

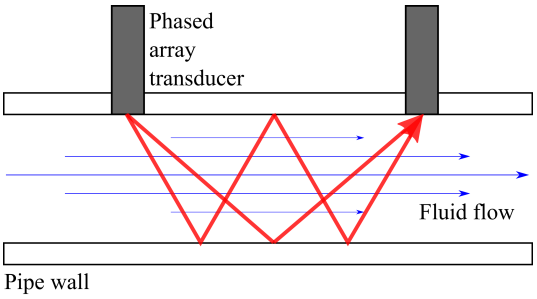

Figure 1.1: Schematic diagram of a flow measurement setup using two phased array transducers.

A first step in researching the possibility of phased array technology for flow measurements is to investigate the individual element that makes up the array.

There are many requirements on the transducer as a whole that have to be met, but many of them can be translated to requirements on the individual element that make up the array.

Ultrasound is defined as acoustic waves with a frequency above the range of human hearing ($f > 20$ kHz). It is an incredibly versatile tool that finds applications in many different areas, ranging from neonatal scans to car parking sensors. Air-coupled ultrasonics (ACU) is the field of ultrasound that concentrates on the generation and detection of ultrasound waves in air or gases in general. A gas has a low acoustic impedance compared to piezoelectric ceramics (typically by a factor of between 70,000 and 80,000), which are traditionally used as the active element in ultrasonic transducers.

A piezoelectric element converts electrical impulses into mechanical vibrations via the piezoelectric effect, which can be used to produce ultrasound in a medium in contact with the piezoelectric element. Inversely, an incident ultrasonic wave can deform the piezoelectric element, inducing an electric field and hence an electrical signal.

The acoustic impedance of a medium relates a force pushing the medium to the resulting velocity of the medium. It is analogous to electrical impedance, where the force and velocity are replaced by voltage and current respectively. It is an important variable in ultrasonics, as it determines the wave transfer and reflection at a boundary between two different materials. As will be seen in the next section, the greater the difference in impedance between two materials the greater the part of the wave that is reflected at the boundary between them. The ratio between the acoustic impedances of air and a piezoelectric ceramic is on the order of $1{:}10^5$, which can be intuitively understood by the large difference in density and sound speed between a gas and a solid. Even though much of the discussion in this Thesis uses air as an example the technology translates to other gases, and to some extent also to liquids, which also have a much lower acoustic impedance than piezoceramics (1:20), even though significantly higher than gases. This large impedance mismatch means that air-coupled piezoceramic transducers are inherently inefficient, and much of the development of ACU is concerned with increasing the coupling efficiency between the transducer and the load medium.

The motivation behind this research is the increased understanding and further development of flexural transducer for ACU applications, specifically looking at the use of flexural transducers for flow metering applications, which is an area that has not been explored before. Traditionally flexural transducers have been constrained to low frequency (< 70 kHz) proximity sensing applications. However,

they could be designed to operate at higher frequencies, with the potential of being suitable for a range of other applications.

1.1 Ultrasound in Fluids

To gain a proper understanding of the challenges and goals of air-coupled ultrasonics (ACU), an introduction to waves in fluids is necessary. In this section homogenous, isotropic and compressible fluids are considered. In these media only longitudinal waves can propagate, which makes the analysis easier compared to the case of waves in solids. For a more thorough discussion on the topic see [1, 2].

1.1.1 One-Dimensional Analysis of Waves in Fluids

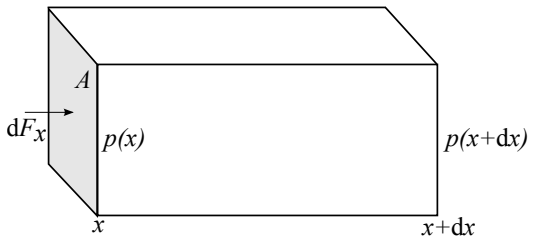

Figure 1.2: Fluid volume element experiencing the force $\mathrm{d}F_x$ producing the pressure p.

Consider a fluid element between x and $x + \mathrm{d}x$, as illustrated in Fig. 1.2. A transducer displacing the fluid along x increases the pressure of the fluid layer relative to the layer to its right. This causes the fluid particles to move along x increasing the pressure in that region, and subsequently the pressure disturbance will propagate in a series of alternative compressions and rarefactions. The force experienced by the fluid element is

$$\mathrm{d}F_x = \left[p(x) - \left(p(x) + \frac{\partial p}{\partial x}\mathrm{d}x\right)\right] A = -\frac{\partial p}{\partial x}\mathrm{d}xA, \tag{1.1}$$

where $p(x)$ is the acoustic pressure, defined as the difference between the absolute pressure and the equilibrium pressure. The mass of the fluid element is $\rho_0 \mathrm{d}xA$. Using Newton's 2nd law gives the equation of motion

$$\frac{\partial p}{\partial x} = -\rho_0 \frac{\partial^2 u}{\partial t^2}, \tag{1.2}$$

where u is the displacement of the fluid particles. The acoustic pressure p can be

expressed in terms of the displacement u and the compressibility χ

$$p = -\frac{1}{\chi}\frac{\partial u}{\partial x}. \tag{1.3}$$

The compressibility is defined as

$$\chi = \frac{1}{V}\left(\frac{\partial V}{\partial p}\right), \tag{1.4}$$

where V is the volume of the uncompressed fluid element. Using equation (1.3) to rewrite the equation of motion (1.2) gives

$$\begin{aligned} \frac{\partial^2 p}{\partial t^2} &= \frac{1}{\rho_0 \chi}\frac{\partial^2 p}{\partial x^2} \\ \frac{\partial^2 u}{\partial t^2} &= \frac{1}{\rho_0 \chi}\frac{\partial^2 u}{\partial x^2} \end{aligned} \tag{1.5}$$

which can be identified as one dimensional wave equations, with wave velocity

$$c = \sqrt{\frac{1}{\rho_0 \chi}}. \tag{1.6}$$

Both forms of the wave equation are equivalent assuming $c =$ constant, i.e. in the linear regime of the compressibility. Solutions to the wave equation take the form

$$u = A\mathrm{e}^{j(\omega t - kx)} + B\mathrm{e}^{j(\omega t + kx)}, \tag{1.7}$$

where ω is the angular frequency of the wave, A is the displacement amplitude of the wave in the forward travelling $(+x)$ direction and B is the displacement amplitude of the wave travelling backwards $(-x)$. Substituting u from equation (1.7) into equation (1.3) gives a useful expression for p

$$p = -\rho_0 c^2 \frac{\partial u}{\partial x} = j\rho_0 \omega c(u_+ + u_-) \tag{1.8}$$

where u_+ and u_- are the terms from equation (1.7) for the forwards and backwards travelling waves respectively. Because of the factor j, the pressure p leads the displacement u by $\pi/2$.

1.1.2 Three-Dimensional Analysis of Waves in Fluids

The extension to three dimensions is straightforward. The displacement u in the one dimensional mode becomes a displacement vector $\boldsymbol{u}$ in three dimensions. The analysis becomes easier by considering the pressure, since it remains a scalar quantity. Also, experimentally, the acoustic pressure is easier to measure than the displacement of a liquid or a gas. For a continuous surface S, the sum of the displacement and area product must equal the change in volume, in accordance with Gauss' theorem[3], so that

$$\Delta V = \oint_S \boldsymbol{u} \cdot \mathrm{d}\boldsymbol{S} = \int_V (\boldsymbol{\nabla} \cdot \boldsymbol{u}) \mathrm{d}V, \tag{1.9}$$

where the divergence of the displacement $(\boldsymbol{\nabla} \cdot \boldsymbol{u})$ is known as the dilation.

Newton's 2nd law in three dimensions is

$$\boldsymbol{\nabla} p = -\rho_0 \frac{\partial^2 \boldsymbol{u}}{\partial t^2}. \tag{1.10}$$

To express the equation in terms of pressure, $\boldsymbol{u}$ can be eliminated by using equation (1.3). By doing this the three-dimensional wave equation for p is obtained:

$$\nabla^2 p = \frac{1}{c^2} \frac{\partial^2 p}{\partial t^2}, \tag{1.11}$$

where $\nabla^2 = \boldsymbol{\nabla} \cdot \boldsymbol{\nabla}$ is the Laplacian operator

$$\nabla^2 = \frac{\partial^2}{\partial x^2} + \frac{\partial^2}{\partial y^2} + \frac{\partial^2}{\partial z^2}. \tag{1.12}$$

By analogy with the one-dimensional case the wave equation for $\boldsymbol{u}$ is

$$\nabla^2 \boldsymbol{u} = \frac{1}{c^2} \frac{\partial^2 \boldsymbol{u}}{\partial t^2}, \tag{1.13}$$

with solutions of the form

$$\boldsymbol{u} = \boldsymbol{u}_0 \mathrm{e}^{j(\omega t - \boldsymbol{k} \cdot \boldsymbol{r})}, \tag{1.14}$$

where $\boldsymbol{r} = (x\hat{\mathbf{i}} + y\hat{\mathbf{j}} + z\hat{\boldsymbol{k}})$ is the position vector and $\boldsymbol{k}$ is the wave number, which gives the direction of propagation. The magnitude of the wave number is related to the wavelength λ by

$$|\boldsymbol{k}| = \frac{2\pi}{\lambda}. \tag{1.15}$$

So far the solutions to the wave equation (1.14) have a constant amplitude $\boldsymbol{u}_0$ in both time t and space $\boldsymbol{r}$. In reality we know that the acoustic pressure decreases with distance from the source, a phenomenon which is known as attenuation. Atten-

uation occurs as the propagation medium absorbs part of the acoustic energy from the wave. The absorption is caused by different physical phenomena, such as fluid viscosity, thermal conductivity and molecular relaxation[4]. The attenuation can be incorporated into the solution by making the wave number complex $k = k' - j\alpha$, so that the wave amplitude decreases exponentially

$$\boldsymbol{u} = \boldsymbol{u}_0 \mathrm{e}^{j(\omega t - \boldsymbol{k'} \cdot \boldsymbol{r})} \mathrm{e}^{-\alpha |\boldsymbol{r}|}. \tag{1.16}$$

Because the fluids considered are assumed to be both homogenous and isotropic the attenuation factor α is a scalar, and the attenuation is a function of the absolute distance $|r|$. Equation (1.16) is still only strictly valid for plane waves. For most real systems the wave source (e.g. the transducer aperture) is finite, which causes additional loss of amplitude over distance due to the geometric spread.

1.1.3 Acoustic Radiation and Beam Directivity

In the analysis in the previous two sections plane wave solutions were considered. Real transducers, due to their finite size, have a finite beam width. The angular distribution of pressure from the aperture of a transducer is known as the beam profile or directivity of the transducer and is important for many applications. There is however no optimal beam profile, as different applications have different requirements in terms of directivity.

Acoustic Radiation from a Point Source

To predict the directivity from a transducer first consider the acoustic pressure from a point source. Since spherical waves radiate from a point source it is convenient to use spherical coordinates. The transformation from cartesian coordinates takes the form

$$\begin{aligned} x &= r\sin(\theta)\cos(\Psi), \\ y &= r\sin(\theta)\sin(\Psi), \\ z &= r\cos(\theta), \end{aligned} \tag{1.17}$$

and the Laplacian operator becomes

$$\nabla^2 = \frac{\partial^2}{\partial r^2} + \frac{2}{r}\frac{\partial}{\partial r} + \frac{1}{r^2\sin(\theta)}\frac{\partial}{\partial \theta}\left(\sin(\theta)\frac{\partial}{\partial \theta}\right) + \frac{1}{r^2\sin^2(\theta)}\frac{\partial^2}{\partial \Psi^2}, \tag{1.18}$$

where θ is the polar angle and Ψ the azimuthal angle. The wave equation is then given by

$$\frac{\partial^2 p}{\partial t^2} = c^2 \left(\frac{\partial^2 p}{\partial r^2} + \frac{2}{r} \frac{\partial p}{\partial r} \right), \tag{1.19}$$

noting that the acoustic pressure is uniform in all directions and hence does not depend on θ and Ψ. Solutions take the form

$$p = \frac{f_d(ct - r)}{r} + \frac{f_c(ct - r)}{r}, \tag{1.20}$$

where f_d describes diverging waves and f_c converging waves. For radiation problems the diverging solution is mainly useful.

To get a relation between pressure and displacement we use Newton's 2nd law

$$\frac{\partial p}{\partial r} = -\rho_0 \frac{\partial^2 u_r}{\partial t^2}, \tag{1.21}$$

where u_r is the particle displacement in the radial direction. Integrating twice with respect to time gives the displacement

$$u_r = \frac{1}{\rho_0 \omega^2} \frac{\partial p}{\partial r}. \tag{1.22}$$

For harmonic solutions the pressure and displacement are

$$p = \frac{A}{r} \mathrm{e}^{j(\omega t - kr)}, \tag{1.23}$$

$$u_r = -\left(\frac{1}{r} + jk \right) \frac{p}{\rho_0 \omega^2}. \tag{1.24}$$

It is seen that the expression for the pressure wave now has a factor $\frac{1}{r}$, which reduces the amplitude of the wave as it spreads out from the point source. It can be shown that the pressure amplitude A for a small spherical (point) source with radius a is given by [5]

$$A = j\rho_0 ck a^2 v_0, \tag{1.25}$$

where v_0 is the velocity amplitude of the surface of the spherical source in the radial direction.

Acoustic Radiation from a Piston

To calculate the pressure field from a circular piston each point on the radiating surface is assumed to be a point-like source, emitting spherical waves in accordance

with equation (1.23). The contribution from each point can then be summed using Huygen's principle[6]. Each infinitesimal area element produces a pressure dp at a point a distance r away from the source

$$\mathrm{d}p = \frac{j\rho_0 ck}{2\pi r}(\boldsymbol{v} \cdot \mathrm{d}\boldsymbol{S})\mathrm{e}^{j(\omega t - kr)}. \tag{1.26}$$

For a piston, with the entire radiating surface moving in phase and with the same amplitude, the velocity $\boldsymbol{v}$ is parallel to the area element vector d$\boldsymbol{S}$ at all points, which simplifies the expression. The total acoustic pressure p is the integral of equation (1.26). The integral is not analytically solvable without some approximations. In the far-field (Fraunhofer) region $r >> a$ and the distance to the observation point from the transducer surface can be taken as constant across the whole surface. This gives an expression for the pressure

$$p = \frac{j\rho_0 cka^2 v_0}{2r}\mathrm{e}^{j(\omega t - kr)}\left[\frac{2J_1(ka\sin(\theta))}{ka\sin(\theta)}\right], \tag{1.27}$$

where J_1 is the Bessel function of the first order. The factor in square brackets gives the directivity of the piston, as it determines the angular variation of the pressure.

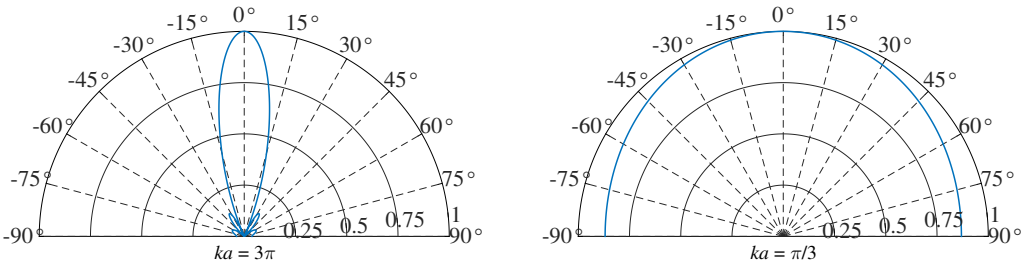

(a) (b)

Figure 1.3: Directivity function from equation (1.27) for (a) $ka = 3\pi$ and (b) $ka = \pi/3$.

Fig. 1.3 shows the directivity plots of a circular piston for $ka = 3\pi$ and $ka = \pi/3$. The beam profile in Fig. 1.3a, associated with the higher value of ka, has two sidelobes, whereas the beam profile in Fig. 1.3b has no sidelobes. In general, for $ka >> 1$ there are multiple sidelobes and for $ka << 1$ the directivity tends towards 1, i.e. if the wavelength is much greater than the radius of the piston it will look similar to a point source in the far-field region. Even though these results were derived from a circular piston, in general the larger the transducer aperture relative

to the ultrasound wavelength, the narrower the main beam.

Acoustic Radiation from an Arbitrary Transducer Displacement Profile

For a circular transducer with arbitrary displacement and velocity across the surface, the expression for pressure cannot be simplified as in previous sections. For continuous wave excitation Harmonic solutions of the wave equation could still be used, but for the general case of pulsed transducers the full time dependent surface velocity $v(x', y', t)$ is required. The resulting integral is known as the Rayleigh integral[7]

$$p = \frac{\rho_0}{2\pi} \frac{\partial}{\partial t} \int_S \frac{v(x', y', t - r/c)}{r} \mathrm{d}S, \tag{1.28}$$

where x', y' are the coordinates of the area element $\mathrm{d}S$ on the transducer surface, r is the distance between the area element with coordinates (x', y') and the point of observation at (x, y, z), i.e.

$$r = \sqrt{(x - x')^2 + (y - y')^2 + z^2}, \tag{1.29}$$

and r/c is the time it takes the ultrasonic wave to travel between the two points. Fig. 1.4 illustrates the transducer surface with denoted coordinates.

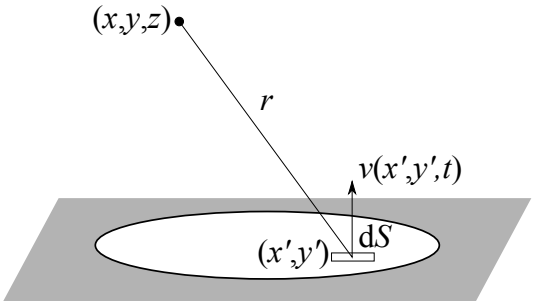

Figure 1.4: Schematic diagram of the geometry, with denoted coordinates, for performing the Rayleigh integral over a surface with an arbitrary velocity profile.

To implement the Rayleigh integral using experimental data for $v(x', y', t)$ equation (1.28) must be discretised. It is common practice when dealing with circular surfaces to use the area element $\Delta S = r' \mathrm{d}r' \mathrm{d}\theta$, where r' is the radial vector on the surface with length $\sqrt{x'^2 + y'^2}$. However, the laser scan system used to obtain the experimental surface displacement takes measurements on a square grid. This makes the area element $\Delta S = \Delta x \Delta y$ more appropriate for integration. The velocity v associated with each area element is given by the discrete differentiation of the displacement. In general then the pressure from discrete displacement data is given

by

$$p = \frac{\rho_0}{2\pi} \sum_i \sum_j \frac{\Delta v_{ij}(t + t_0 - r_{ij}/c)}{\Delta t \, r_{ij}} \Delta S, \tag{1.30}$$

where

$$v_{ij} = \frac{\Delta u_{ij}}{\Delta t}, \tag{1.31}$$

and t_0 is an integer number of time steps added to avoid negative index numbers.

Equation (1.30) allows the pressure to be projected to any arbitrary point or set of points in space. Usually though it is only necessary to find the pressure along an 180° arc, as presented for the piston in Figs. 1.3a and 1.3b, to sufficiently characterise the transducer directivity. To accurately predict the absolute level of the acoustic pressure damping has to be included, as in equation (1.16). Determining the correct damping factor α is treated in [8].

To confirm that p from the numerical Rayleigh method, expressed by equation (1.30), converges with the analytical solution in the far field, the velocity profile of a plane piston undergoing undamped harmonic motion with $ka = 4\pi$ was substituted for v_{ij}, with $i, j = 1, 2, 3, \ldots, 44$. The pressure was projected along an arc of constant radius in the Fraunhofer region. Fig. 1.5 shows the resulting amplitude directivity function as well as the analytical solution from equation (1.27). The figure is plotted in cartesian coordinates in order to better compare the sidelobes. The results are in very good agreement. There is some divergence as the angle approaches ±90°, which is due to the rather coarse discretisation of the piston surface, $\Delta x = \Delta y = a/15$. The value for Δx and Δy was chosen to roughly correspond to the step size used in later sections for experimental data.

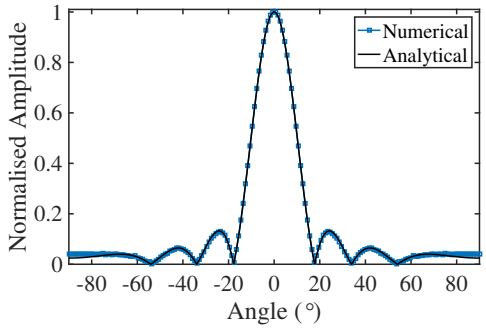

Figure 1.5: Directivity function of a piston with $ka = 4\pi$ from the discrete integral in equation (1.30) (□) and from the analytical expression in equation (1.27) (–).

1.1.4 Waves at Interfaces

When an ultrasonic wave meets a boundary, like the interface between two different media, part of the wave will be transmitted through the boundary and part reflected back. An understanding of the principles of transmission and reflection are essential in any application of ultrasonic waves.

The specific acoustic impedance of a material is[9]

$$Z = \frac{p}{v}, \tag{1.32}$$

where p is the instantaneous acoustic pressure and v is the instantaneous velocity associated with that pressure. The specific acoustic impedance can be positive or negative depending on the direction of the velocity v. Taking the absolute of the specific impedance gives the characteristic impedance, which can also be defined as

$$Z_c = \rho c, \tag{1.33}$$

where ρ is the volume density, and c the sound velocity of the material.

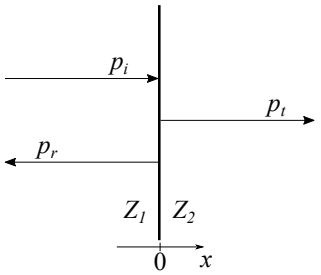

Figure 1.6: Reflection and transmission of an incoming wave from the left at a planar interface at $x = 0$ between two bulk media with acoustic impedances Z_1 and Z_2.

Consider a harmonic wave at normal incidence to the boundary between two media with characteristic acoustic impedances Z_1 and Z_2 respectively, as illustrated in Fig. 1.6. The incident pressure wave is partially transmitted and reflected at the interface, which gives the three waves

$$\begin{aligned} p_i &= A\,\mathrm{e}^{j(\omega t - k_1 x)}, \\ p_r &= AR\,\mathrm{e}^{j(\omega t + k_1 x)}, \\ p_t &= AT\,\mathrm{e}^{j(\omega t - k_2 x)}, \end{aligned} \tag{1.34}$$

where T and R are the pressure transmission and reflection coefficients respectively.

They are the fractions of the incident wave amplitude that is transmitted and reflected. The frequency of the wave is the same in both media, but the change in impedance implies a change in velocity, which then changes the wave number k of the wave. At the interface, assuming it is well defined, continuity of pressure and velocity can be assumed, i.e. for $x = 0$

$$\begin{aligned} p_i + p_r &= p_t, \\ \frac{p_i}{Z_1} - \frac{p_r}{Z_1} &= \frac{p_t}{Z_2}. \end{aligned} \tag{1.35}$$

Using the expressions for the waves in equation (1.34) with the continuity boundary conditions in equation (1.35) gives

$$\begin{aligned} 1 + R &= T, \\ \frac{1}{Z_1}(1 - R) &= \frac{T}{Z_2}. \end{aligned} \tag{1.36}$$

The equations can be rewritten to give the transmission and reflection coefficients in terms of the impedances only

$$T = \frac{2Z_2}{Z_1 + Z_2}, \tag{1.37}$$

$$R = \frac{Z_2 - Z_1}{Z_1 + Z_2}. \tag{1.38}$$

In one extreme, where the impedances of the two materials are the same, the transmission coefficient becomes 1, meaning that there is no reflected energy. Hence, the maximum ultrasound power transmission from one medium to the next occurs when their impedances are equal. It is equivalent to having no boundary between the two regions.

A relevant example to consider is that of ultrasound waves going from a piezoceramic material into air. In this example $Z_1 = Z_{\mathrm{PZT}} \simeq 30$ MRayl, and $Z_2 = Z_{\mathrm{air}} \simeq 430$ Rayl. There is a large difference between the impedances of the two media, which leads to a transmission coefficient $T = 2.9 \times 10^{-6}$, or equivalently a reflection coefficient $R = -0.999997$. To estimate the energy transmitted and reflected these numbers would be squared. In essence, very little energy is transmitted.

1.2 Air-Coupled Transducer Technology

1.2.1 Impedance Matching Layer

The coupling to air and the transduction efficiency can be improved by gradually reducing the acoustic impedance along the path of wave propagation between the piezoceramic and air with a matching layer[10]. The matching layer goes between the piezoelectric element and the air. To optimise energy transmission the matching layer requires an intermediate impedance Z_{ML}. To find the input impedance of the matching layer consider a layer with thickness h between two bulk media, as illustrated in Fig. 1.7.

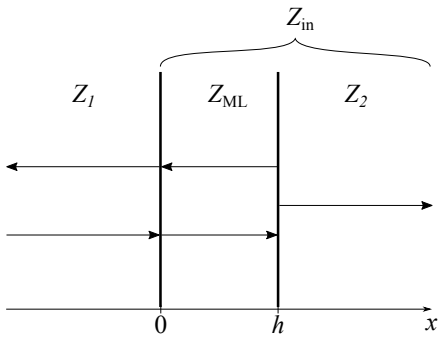

Figure 1.7: Transmission and reflection from a matching layer with thickness h sandwiched between two different bulk media.

The pressure in the matching layer can be written as

$$p_{\mathrm{ML}} = A\,\mathrm{e}^{jk_{\mathrm{ML}}x} + B\,\mathrm{e}^{-jk_{\mathrm{ML}}x}, \tag{1.39}$$

where the time factor $\exp(j\omega t)$ has been neglected as it is common to all terms. Multiple reflections in the matching layer set up forward and backward travelling waves, giving rise to the two terms in equation (1.39). The amplitude coefficients A and B can be found by applying the boundary conditions of continuity of p and v across both interfaces. This gives an expression for the input impedance in terms of Z_{ML}, Z_2 and h:

$$Z_{in} = Z_{\mathrm{ML}}\left(\frac{Z_2 - jZ_{\mathrm{ML}}\tan(\phi)}{Z_{\mathrm{ML}} - jZ_2\tan(\phi)}\right), \tag{1.40}$$

where $\phi = k_{\mathrm{ML}}h$ is the phase change due to the layer thickness.

For maximum output the matching layer should have a thickness $h = \frac{\lambda}{4}$[10], as shown in Fig. 1.8. This ensures that the wave is always in phase in the matching layer, causing constructive interference of reflected waves with wavelength λ.

Substituting this value for h into equation (1.40) gives

$$Z_{in} = \frac{Z_{\mathrm{ML}}^2}{Z_2}. \tag{1.41}$$

By using equation (1.38) the reflection coefficient is given by

$$\begin{aligned} R &= \frac{Z_{\mathrm{in}} - Z_1}{Z_1 + Z_{\mathrm{in}}} \\ &= \frac{Z_{\mathrm{ML}}^2 - Z_1 Z_2}{Z_{\mathrm{ML}}^2 + Z_1 Z_2}. \end{aligned} \tag{1.42}$$

Maximum transmission occurs for $Z_{\mathrm{ML}} = \sqrt{Z_1 Z_2}$, i.e. when the intermediate layer has an impedance equal to the geometrical mean of the other two media, for which $R = 0$. Theoretically then, a $\frac{\lambda}{4}$ matching layer could produce perfect transmission. However, this is only strictly true for vibrations with a frequency corresponding to λ, which will consequently narrow the transducer bandwidth, as waves with this frequency are preferentially transmitted. The overall transmission is therefore reduced from 100% for all real waves which have a non-zero bandwidth.

Using a piezoceramic and air interface as an example, see Fig. 1.8a, an appropriate matching layer would have $Z_{\mathrm{ML}} = 0.11$ MRayl. This is a low value, which can only in general be found in very light and airy materials. Wood cork is a good example, and has an acoustic impedance of 0.12 MRayl. Often materials with a sufficiently low impedance will have other unwanted properties such as high attenuation, environmental instability and difficult machining[11]. For comparison water has an impedance $Z_{\mathrm{w}} = 1.5$ MRayl, which is still significantly lower than that of a piezoceramic.

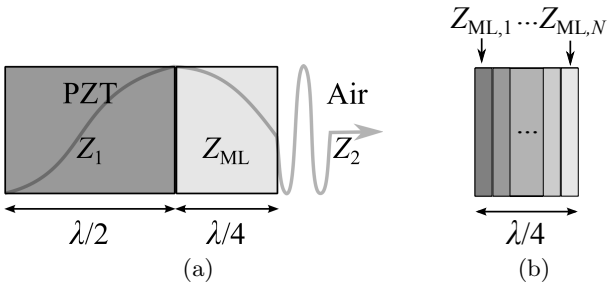

Figure 1.8: Schematic diagrams illustrating the use of acoustic impedance matching, with (a) single $\lambda/4$ matching layer, and (b) multiple matching layers.

It is also possible to use multiple matching layers with a combined thickness

of a quarter wavelength[12], as shown in Fig. 1.8b. The correct impedance $Z_{\mathrm{ML},n}$ for the n^{th} layer of N matching layers is given by[10]

$$Z_{\mathrm{ML},n} = \sqrt[n+1]{Z_1^{N-n+1} Z_2^n}. \tag{1.43}$$

Ideally, a single matching layer with a continuously decreasing impedance from Z_1 to Z_2 would be used. This also serves the purpose of increasing transducer bandwidth. Due to cost and manufacturing difficulties the single quarter wavelength matching layer is still most commonly used for commercial ACU. An effective air-coupled matching layer using a combination of porous materials and rubber material was studied in [13].

1.2.2 Piezoelectric Composite Transducers

Composite transducers are made by embedding a structure of active piezoelectric material in a passive filler[14], such as a polymer, which is more compliant than the ceramic. The composite structure can thus have a much lower acoustic impedance than the corresponding pure ceramic by adjusting the ceramic volume fraction. A 1-3 connectivity composite transducer[15], which comprises an array of piezoelectric pillars separated by the filler (as illustrated in Fig. 1.9), are often used for their ease of manufacturing and electroding. This type of transducer is also suitable for making into an array, by electroding one side with the desired array pattern, since the pillars are naturally insulated from each other. Transducers use the through thickness mode along the z axes of the pillars to generate ultrasound. As the volume fraction is reduced the acoustic impedance is lowered, but because the percentage of active material is reduced the electrical permittivity ϵ_r is also reduced, which lowers the transducer performance in transmit mode (i.e. for generating ultrasound waves). Hence there is a trade off between the relative permittivity and the acoustic impedance. An in depth study of 1-3 connectivity transducers found that the optimal ceramic volume fraction for transmission and reception efficiencies in air are in the ranges 50%-70% and 10%-30% respectively[15].

Although a low volume fraction significantly lowers the transducer's acoustic impedance, it is still several orders of magnitude greater than that of air. It is therefore common to combine the composite transducer with one or more matching layers, which can boost transducer efficiency further[16]. Composite transducers are well matched to water, and are therefore often used for medical applications to couple ultrasound into human tissue[17].

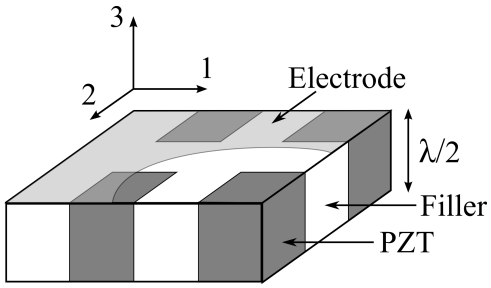

Figure 1.9: Schematic diagram of a 1-3 connectivity composite with square PZT pillars.

1.2.3 Soft Piezoelectric Materials

There are also piezoelectric materials that are naturally more compliant than ceramics, and can therefore be used without matching layers for ultrasound transmission and reception in air.

Cellular electret films, made from polytetrafluoroethylene[18], silicon dioxide[19] or polypropylene[20], have acoustic impedances < 0.1 MRayl and exhibit a pseudopiezoelectric response combined with mechanical flexibility. The electroacoustic response of polypropylene cellular electret films has been investigated in [21], and has been tested as a novel active matching layer in [22]. One of the drawbacks with using these electrets is a large attenuation factor and a lack of robustness, which arises due to the necessary porosity of the material.

In 1969, the polymer material polyvinylidene fluoride (PVDF), which had been stretched and poled at an elevated temperature, was discovered to have piezoelectric properties[23]. A stable d_{31} of 20 pmV^{-1} was observed (more details regarding piezoelectric constants such as d_{31} will be given in section 4.1.1), which can be compared to the widely used piezoceramic PZT5H, which has $d_{31} = -274$ pmV^{-1}. The material has a low acoustic impedance, mechanical flexibility, and a relatively low cost of manufacturing. The electromechanical coupling coefficient of PVDF is also not as high as that of standard PZT ceramics, but this is to some extent compensated by the high electric field strength made possible by the thinness of PVDF films, which enables large displacements for relatively low driving voltages[24]. The use of PVDF to make a curved and cylindrical transducer for ACU is found in [25] and [26] respectively. PVDF has many advantages as the active transducer material for ACU, but it is not environmentally very robust. The material depolarises at the relatively low temperature of 80°C.

1.2.4 Electrostatic Transducers

Electrostatic, or capacitive, transducers, including capacitive micromachined ultrasonic transducers (CMUTs)[27], have shown a lot of promise in various applications requiring ultrasonic transmission into low impedance media. Especially in the medical field CMUTs are promoted as a potential alternative to 1-3 composite transducers [28].

An electrostatic transducer works on the principle of having a thin membrane, which is rigidly stretched by a large bias voltage ($\sim$ 200 V) between the membrane and a backing substrate, as illustrated in Fig. 1.10. An AC signal applied to the top electrode will then cause the membrane to vibrate and hence generate ultrasonic pressure waves in the medium. In receive mode, incoming waves cause the membrane to vibrate giving rise to an electrical signal.

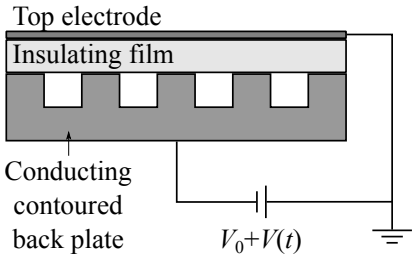

Figure 1.10: Schematic diagram of an electrostatic transducer with a bias voltage V_0.

The use of CMUTs for contactless NDE has been demonstrated in [29], and for flow measurements in [30]. CMUTs have shown excellent performance both in terms of coupling and bandwidth, but have some potential disadvantages compared to piezoelectric transducers. For optimum coupling the bias voltage V_0 has to be close to the breakdown voltage of the capacitive element [31]. A high bias voltage, usually around 200 V, can be a problem in of itself in terms of supporting electronics as well as from an intrinsic safety point of view. Because of these considerations, research into reducing bias voltage, or removing it entirely, is ongoing[32].

Different design philosophies apply to transmitting and receiving CMUTs. A receiving CMUT with a high sensitivity will have a small gap between the membrane and the substrate, whereas a good transmitter needs a larger gap to accommodate large displacement amplitudes. This makes CMUTs to some extent harder to design for pulse-echo applications, where one transducer is used for both transmitting and receiving.

1.2.5 Piezoelectric Flexural Transducers

Flexural transducers use the bending modes of a thin plate to transmit ultrasound to a low impedance medium. Because a thin plate is more compliant than a bulk sample, the effective acoustic impedance is much lower than the characteristic impedance of the material as defined in equation 1.33. Fig. 1.11a shows a schematic diagram of a standard piezoelectric flexural transducer. A thin piezoelectric element is bonded to a passive metal layer. When an electric field is applied the piezoelectric disc expands radially, but because it is constrained at the metal boundary the two layer system bends, as illustrated in Fig. 1.11b. In this way large deflections can be created for a relatively low input voltage. Because the flexural transducer is inherently a resonant system it has a narrow bandwidth, which limits its use for certain applications. In essence, the flexural transducer achieves large signal amplitude at the loss of bandwidth. Mechanical and electronic damping of the transducer can reduce ring down time, and hence increase bandwidth to some extent, but this comes at a cost in overall displacement amplitude.

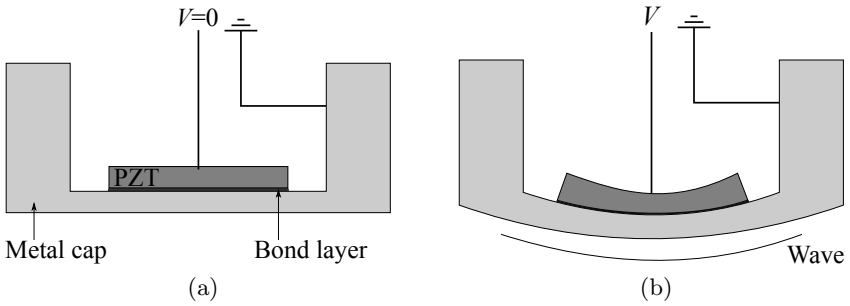

Figure 1.11: Schematic diagrams of a typical flexural transducer, (a) with no applied voltage and (b) with an applied voltage.

There has been more recent development of micromachined, multi-cell flexural transducers, so called piezoelectric micromachined ultrasonic transducers (PMUTs) [33], with obvious parallels to CMUTs as seen in the previous section. Fig. 1.12 shows a schematic diagram of a single cell PMUT transducer. The substrate will typically be machined from silicon, as there exists extensive background knowledge in processing the material for MEMS technology. Similar to standard flexural transducers the operation frequency of a PMUT is not determined by the through thickness resonance of the piezoelectric element, but rather by the combined thickness and diameter of the membrane, electrodes and active film. These can be precisely varied to achieve a wide range of different resonance frequencies. A recent, detailed,

analysis of PMUT behaviour with comparisons to simulation results is found in [34]

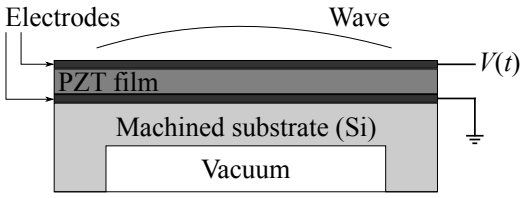

Figure 1.12: Schematic diagram of a crossectional view of a single PMUT cell. Typical dimensions are on the order of tens of microns laterally and on the order of microns in thickness.

For both types of flexural transducers there is a balance between coupling and frequency. A plate or membrane with high compliance, achieved by a large diameter and small thickness, gives the best coupling to low impedance media but also reduces the resonance frequencies of the device. Hence the higher the frequency of the device the lower the coupling efficiency to the load medium.

1.3 ACU Technology Applications

1.3.1 Flow Metering

The measurements and monitoring of fluid flow or flow metering, is crucial for many industries. Flow metering is used in the petrochemical industry to measure the volumetric flow of natural gas and oil [35]. Water companies use metering to keep track of how much water is being used and recycled, as well as for monitoring water levels.

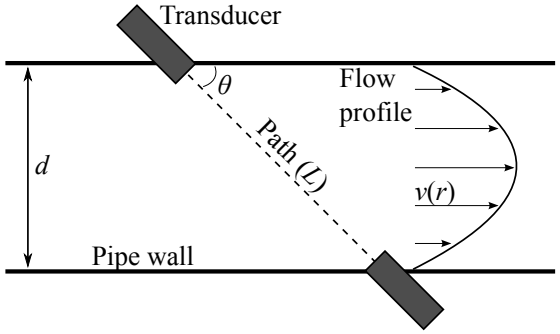

Figure 1.13: Schematic diagram of a single path ultrasonic flow measurement using two transducers in pitch-catch mode in laminar flow (parabolic flow profile).

Ultrasonic flow metering often uses time-of-flight (TOF) measurements of waves travelling upstream and downstream of the flow. The waves will have a velocity which is the vector addition of the inherent velocity of ultrasound in the specific medium and the velocity of the flow. Hence, for a wave travelling downstream the velocity will be greater and the measured TOF smaller. A typical pitch-catch setup is illustrated schematically in Fig. 1.13. The ultrasound transit times upstream t_u and down stream t_d are given by

$$\begin{aligned} t_u &= \frac{L}{c - v\cos(\theta)} \\ t_d &= \frac{L}{c + v\cos(\theta)}, \end{aligned} \tag{1.44}$$

where L is the length of the ultrasound path, c is the sound speed in the medium with no flow, v is the average flow velocity at and an angle θ to the ultrasound path. t_u and t_d are measured by alternating generator and receiver modes between the two transducers. Solving for the flow velocity v cancels c and the need of any inherent knowledge of the propagation medium to give

$$v = \frac{d(t_u - t_d)}{2t_u t_d \sin(\theta)\cos(\theta)}, \tag{1.45}$$

where d is the inner diameter of the pipe, such that $L = d/\cos(\theta)$. It is important to note that the flow velocity v from equation 1.45 is not enough to work out the volume flow or the mass flow under most circumstances. v is a measure of the average flow velocity along a single line through the pipe and will only correspond to the crossectional average in the specific case of a completely flat flow profile. That is, unless the flow velocity $v(x, y) = v$ the volume flow can only be estimated. The velocity v and the volumetric flow velocity v_m can defined as

$$\begin{aligned} v &= \frac{1}{L}\int_L v(r)dL \\ v_m &= \frac{1}{S}\int_S v(r)dS, \end{aligned} \tag{1.46}$$

where S is the crossectional area of the pipe, and assuming that the flow is symmetric about the central axis of the pipe, i.e. axisymmetric flow.

To solve this, a wetted ultrasonic flow meter will in general have several pairs of transceivers, each with a unique path through the pipe [36]. Such a meter, known as a multi-path meter, covers a larger proportion of the crossectional area of the pipe. This allows for more accurate predictions of the volumetric flow v_m.

Multi-path meters can also measure swirl. Ultrasonic flow meters with as many as 24 paths are commercially available.

1.3.2 Non-Destructive Evaluation (NDE)

Contactless techniques can be beneficial and sometimes essential in various NDE applications. It has found extensive applications in techniques using Lamb waves (thin plate waves) to evaluate defects in plates [37]. The technique has been shown effective on various materials, including composites such as carbon fibre reinforced polymer (CFRP). Laser ultrasound is another non-contact technique that is used for inspection of composite materials [38]. However, laser ultrasound systems are expensive to set up, and not energy efficient to run.

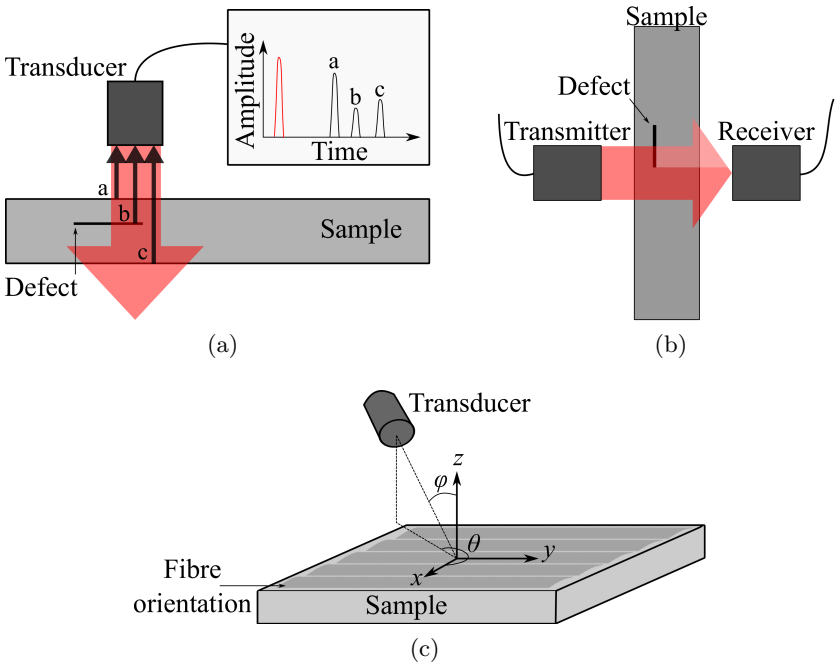

Figure 1.14: Schematic diagrams of some typical ACU NDE techniques, including (a) pulse-echo, (b) spectroscopy/through transmission and (c) back scattering.

There are different techniques of using ACU for NDE, including pulse-echo, through transmission, ultrasonic spectroscopy and back scattering, which are illustrated in Fig. 1.14. Pulse-echo (Fig. 1.14a) is one of the most common techniques, where a single transducer emits a short pulse at right angles to the sample surface, and then receives the reflected waves. The depth, and to some extent the size, of

the defect can be determined from the time and amplitude of the associated echo, as well as sample thickness. Through transmission (Fig. 1.14b) can be used for simple defect detection by looking at signal amplitude. By scanning the sample the defect can be effectively sized laterally. The technique is also often used for quickly scanning sample thickness. Ultrasonic spectroscopy, often using a through transmission setup, analyses the frequency content of a signal that has interacted with a sample, and by comparing it to the frequency content of the input pulse, information regarding the sample structure can be deduced. Back scatter techniques (Fig. 1.14c) are most applicable to samples with an inherent non-homogenous surface or near-surface structure, such as CFRP. It is similar to the pulse echo setup, but importantly the ultrasonic waves are incident upon the sample at an angle ϕ. While ϕ is kept constant the sample or transducer is rotated through the angle θ. The received signal amplitude depends upon the orientation of the sample structure with respect to the incident ultrasound.

1.3.3 Metrology and Proximity Sensing

Ultrasonic techniques have been used for decades for proximity sensing and imaging applications. The field has seen an increased amount activity with the advent of car parking sensors and more recently driverless cars, which need multiple sensor technologies in order to function safely. The mass production of simple yet robust transducers that are needed for these types of applications has been driving the development of low cost, robust and easy to manufacture devices. The flexural transducer is in many ways ideal for this type application, as it only needs a small amount of the more expensive active material (PZT), and the metal housing of the transducer, as was seen in Fig. 1.11a, inherently provides it with the necessary ruggedness and environmental protection. Another advantage is the lack of matching layers, as they can increase the unit cost, the number of production steps, and introduce more points of failure.

Flexural transducers are also used in robotics[39] and for remote location applications, e.g. to monitor water levels due to their low power consumption, allowing them to be driven with simple support electronics and batteries.

Another new use of TOF ACU is touchless gesture control of smart devices[40]. A device, such as a smartphone or tablet, is supplied with ultrasonic sensors. The sensors continuously monitor the distance of objects (usually hands) from the screen. By having a high frame rate movements towards and away from the screen can be detected. Also, by using multiple transducers gestures parallel to the screen and multiple objects can be tracked. This technology is not yet readily available and

is largely still in the development stage, but some patents governing the use of ultrasonic transducers for this purpose have been published[41].

1.4 Phased Array Ultrasound

Ultrasonic phased array transducers use interference between individual transducer elements to electronically sweep, steer and focus ultrasound. This is especially useful in imaging applications and is used extensively in medicine as a diagnostic tool[42] and in NDT for flaw detection and characterisation[43, 44]. Although research into air-coupled ultrasound arrays has increased over the last decade, the technology is still in an early stage of development[45]. Three basic types of array geometries are linear (1D) arrays, two dimensional arrays and annular arrays, which are illustrated in Fig. 1.15. Annular arrays are more restrictive than the 1D and 2D arrays in that it can only focus a beam, and not steer it.

In theory any beam shape can be constructed by a properly populated two dimensional (2D) array, but current applications are mostly limited to beam steering and focusing. The array is thus often employed to carry out the same work as several regular transducers, or a single transducer applied in several different ways. For example, beam steering allows a single transducer array to image a large volume of material from a single location, whereas a single element transducer has to be moved and angled to produce similar results.

The physical principles behind steering and focusing are simply constructive and destructive interference between waves from independent sources. Thus to focus a beam at a specific point, the signal to each element of the array has to be time delayed so that all wavefronts reach the focal point at the same time, compensating for the difference in path lengths from the individual elements to the focal point. For a linear array the time delay applied to the n^{th} element for steering at angle θ is given by[46]

$$\delta t_n = \frac{nd}{c}\sin(\theta), \tag{1.47}$$

where d is the distance between elements also known as the pitch and c is the speed of sound in the medium of propagation. n can be positive or negative with $n = 0$ denoting the central array element. For focusing, the delays are given by[47]

$$\delta t_n = \frac{r_0 - r_n}{c}, \tag{1.48}$$

where r_0 is the distance or path length from the centre of the central element to the focusing point, and r_n is the path length from the centre of the n^{th} element to

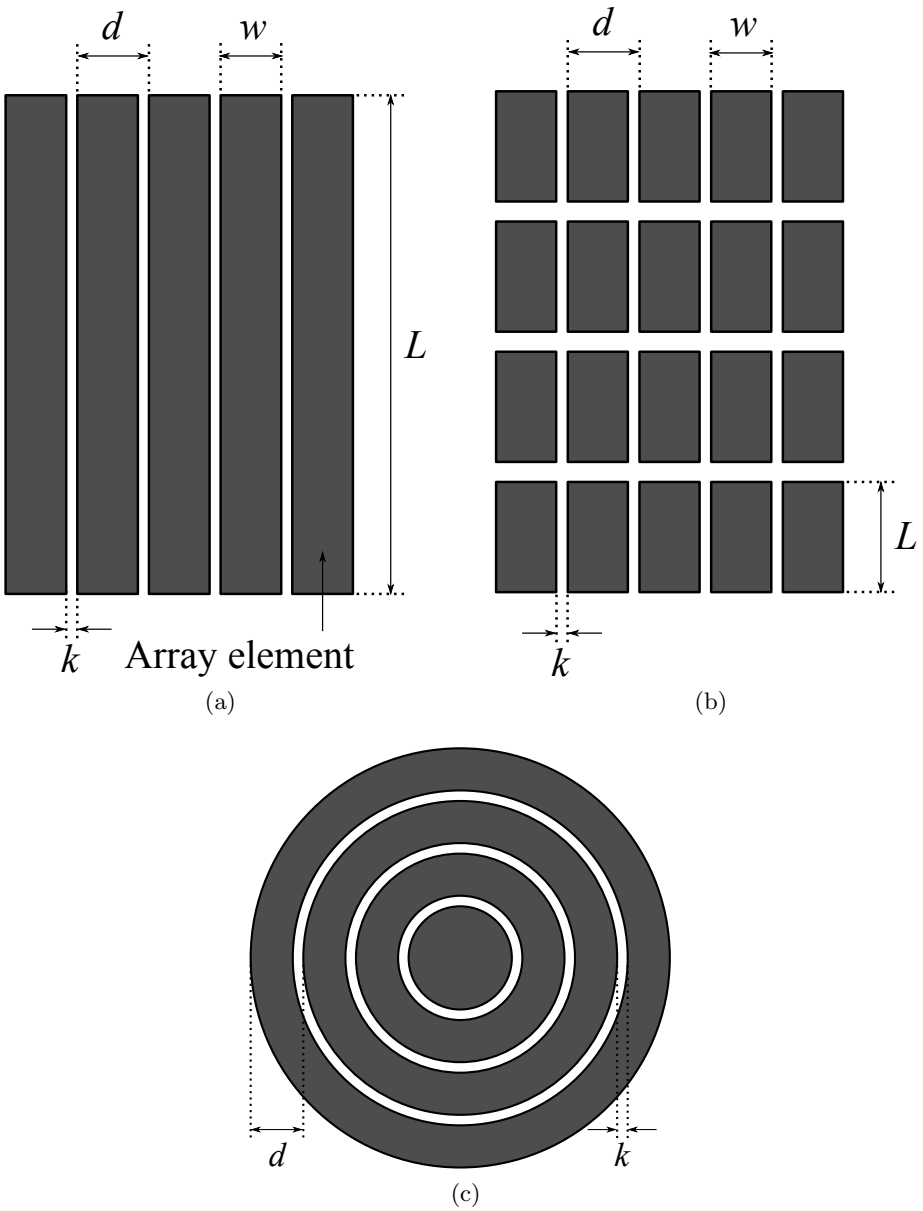

Figure 1.15: Schematic diagrams of three array geometries (a) linear (1D), (b) two dimensional (2D) and (c) annular. In the diagrams d is the interelement spacing or pitch, k is the kerf, w the element width and L the element length or elevation.

that point. Often an additional constant term t_0 is added to equations (1.47) and (1.48) to avoid negative time delays. The delay laws for steering and focusing can be combined to focus the beam at any arbitrary point in front of the transducer. Fig. 1.16 shows how a linear array is used to steer and focus by applying appropriate delays to the individual elements. To reconstruct an image from incoming waves, the inverse delay laws are applied to each receiving element respectively.

If the spacing between elements, i.e. the pitch, is greater than half the wavelength in the propagation medium, $d > \lambda/2$, then constructive interference will occur at multiple angles. This is known as the $\frac{\lambda}{2}$ criterion[48]. The additional beams are referred to as grating lobes, and are different from side lobes, which are not specific to array transducers. Grating lobes are problematic as they take away energy from the direction of interest, limit the field of view and create ghost objects in images. For air-coupled ultrasonics, because of the low sound speed and the relatively large element apertures required for generating significant pressure amplitudes, the $\frac{\lambda}{2}$ criterion cannot easily be met[45]. For applications that do not involve wide angle imaging, grating lobes are less of a problem. There are also techniques for reducing the amplitude of grating lobes or limiting their effect. For example, non periodic patterns can greatly reduce grating lobes. Some success has been achieved with random arrays[49] as well as binned arrays[50]. A recent study investigated the properties of an array placed in a Fermat spiral pattern[51].

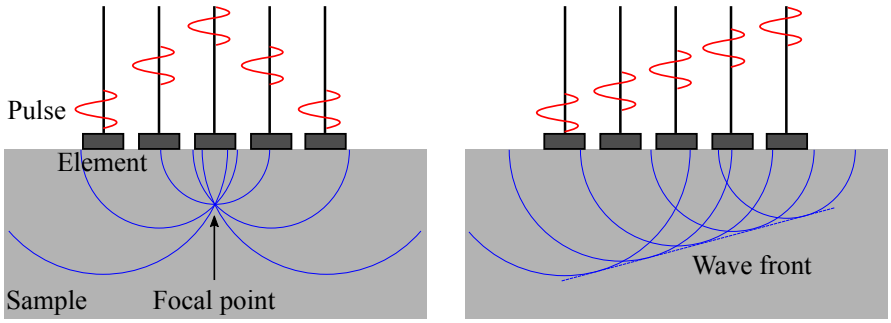

Figure 1.16: Schematic diagrams illustrating (a) focusing and (b) steering, using a phased array ultrasound transducer.

Chapter 2

Transducer Characterisation Techniques

Several different techniques were used to characterise different aspects of ultrasonic transducers. Some techniques, such as electrical impedance and output pressure directivity measurements, are routinely used for transducer characterisation. Other, more novel, methods were designed and used, and will be outlined in detail in this section. From the characterisation, different figures of merit can be extracted, and some of these will require a brief description, as they are not always universally known or agreed upon.

2.1 Laser Generation and Detection

As noted in the introduction §1.2.5, the operational frequency of a flexural transducer is determined by the geometry of the passive layer and piezoelectric unimorph system. For a thin piezoelectric disk the passive layer, i.e. the metal cap, becomes the dominant component, which sets the resonance frequencies of the transducer. Hence it is important to characterise the cap in terms of its resonance behaviour. There are several advantages of doing this before the transducer has been assembled, i.e. before bonding the piezoelectric disc to the cap. The effects of bonding the piezoelectric element to the cap can be isolated in later tests, which allows consistency in the bonding process to be evaluated. Also, the resonance behaviour of the piezoelectric element itself, such as the through thickness modes, can more easily be separated from that of the transducer as a whole. By comparing the results from a set of caps, the consistency and tolerance of the dimensions can be evaluated.

The dimensions of the passive layer could be accurately determined by for

example X-Ray imaging, but this is expensive, slow and provides an unnecessarily high level of detail. Also, for ultrasound transducer purposes we are more interested in the dynamic properties. Without the piezoelectric element some other means of actuating the cap has to be used in order to observe its dynamic behaviour. The method of actuation should be contactless, in order to affect the cap to a minimal extent and ensure consistency between subsequent tests. It is also important that the excitation is broadband, so as to reveal a large range of modes in the interrogated structure. Laser generated ultrasound[52] is well suited for this task. A laser pulse can be tailored to fit the area of a specific target, to act in the thermoelastic regime so as to not ablate the target, and be sufficiently short to provide a broad band of frequencies. The generation laser used was a Nd:YAG laser, with wavelength $\lambda = 1064$ nm, and a pulse duration of approximately 10 ns. Filters and focusing lenses were used to reduce incident power below the ablation threshold, and to get a spot size of approximately 6 mm.

To detect the resulting vibrations it is important to also have a broadband receiver, to accurately assess the dynamic behaviour of the cap and not filter out or bias some modes. Several different optical techniques using interferometry could be suitable[53]. In this work an intelligent optics system (IOS) two wave mixer laser interferometer was used [54]. The system is sensitive to the transverse (out of plane) displacements, and has a bandwidth of 125 MHz with sensitivity from around 100 Hz. Surface displacement sensitivity is 4×10^{-7} nm $(\mathrm{W/Hz})^{\frac{1}{2}}$. It has a continuous wave (CW) laser operating at 1550 nm, with variable power up to 2W, depending on the sample surface. The setup for laser generation and detection is shown in Fig. 2.1.

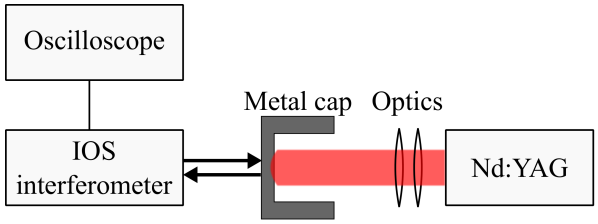

Figure 2.1: Schematic diagram of the laser generation and detection setup used for characterising the passive layer in the flexural transducer before assembly.

2.2 Time Resolved Front Face Displacement

One of the most important characteristics for transducers in general and for flexural transducers in particular is the front face displacement. It is the displacement which pushes the load medium allowing the wave to propagate. Because of the low acoustic impedance of air, discussed earlier in §1.2, large displacements of the front face are essential for effective transmission. By taking a time resolved measurement of the displacement across the whole surface of a transducer several properties can be determined. The absolute displacement for a given excitation voltage gives a figure related to the transducer efficiency. A high displacement for a low voltage means that transducer can operate with simple supporting electronics, be battery driven, and can be operated intrinsically safe. The results from these measurements also reveal resonance behaviour, if the device is driven with a suitable excitation signal. A broadband excitation pulse allows the transducer to ring down at its mechanical resonance frequencies, which by Fourier transformation reveals the frequency modes. Using a narrowband pulse, individual modes can be isolated and analysed. With a function generator, a CW voltage will give a pure single frequency mode.

Alternatively, to study a single mode, digital signal processing (DSP) can be used. From the frequency spectrum of the broadband excitation displacement data, a digital narrowband frequency filter can be designed. Recursively applying the filter to the displacement signal of each point of the scanned area will eliminate the vibration contributions from all other modes with frequencies outside that of the filter, leaving a pure mode. Compared to the CW technique, where each mode requires a separate scan, using DSP can save a significant amount of time and no previous knowledge of the resonance frequencies is required.

The setup for measuring the front face displacement is shown in Fig. 2.2. A Polytec laser vibrometer (OFV-5000) was mounted on a modified commercial 3D printer (Velleman kit K8200). The printer uses electrical stepper motors (NEMA 17), with a minimum step size of 1.8°, and belt drives to move the print bed in the xy-plane. The printer movement is controlled from a PC using a custom script written in Matlab. The laser vibrometer output is connected to a PicoScope, which is a computer controlled digital oscilloscope, which in turn is controlled by the same Matlab program as the stage. Because of the minimum step size of the electric motors, the stage has a limited minimum linear step of 0.015 mm, and cannot reach every position. An algorithm was implemented that checked the position of the stage after the move command had been issued. If the stage was unable to reach the specified position the actual coordinates were recorded instead.

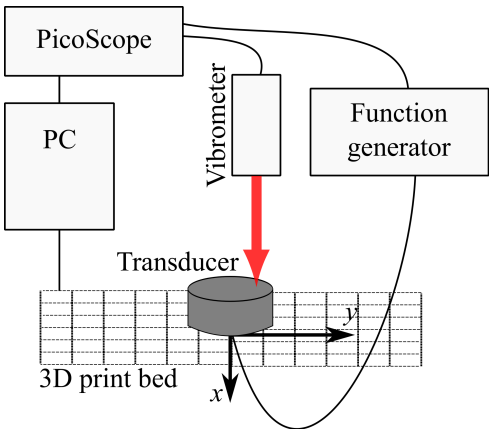

Figure 2.2: Schematic diagram of the setup used for the front face displacement scan of a transducer.

The most persistent problem with the displacement scanning technique was that of achieving consistent signal strength from the laser vibrometer, across the transducer surface. The signal strength depends on the focus of the laser as well as the surface conditions of the sample. Hence as the sample moves, small differences in surface conditions would sometimes have a large impact on the signal strength. Under a certain threshold the data became corrupted, resulting in spurious spikes of displacement on the surface. Fortunately these data points were easy to identify and could either be removed from the set, or smoothed out by two dimensional spatial averaging.

2.3 Electrical Impedance Analysis

The electrical impedance of any electrical device provides a useful set of characteristics. The impedance of an ultrasonic transducer can be used for different things, such as determining suitable supporting electronics, and finding resonance vibration frequencies. Research described here focused on the resonance behaviour deducible from peaks in the phase of the impedance as a function of frequency. At low driving frequencies a piezoelectric disc generally behaves like a parallel plate capacitor. Charge builds up on the two electroded faces, with the insulating piezoelectric material in between. At resonance frequencies however, the piezoelectric element starts to dissipate energy in the form of mechanical vibrations.

Electrical impedance is defined as

$$Z = \frac{V}{I}, \tag{2.1}$$

which can be seen as an extension of Ohm's law to take time varying voltages ($V(t)$) and currents ($I(t)$) into account.

The impedance is in general a complex number due to a phase shift between voltage and current. The impedances of an ideal resistor, inductor and capacitor are shown in table 2.1. The impedance of a simple resistor is purely real and equal to the resistance R, while the impedances of capacitors and inductors are purely imaginary.

Table 2.1: Impedance of ideal electric components.

Component	Impedance
Resistor	R
Inductor	$j\omega L$
Capacitor	$\frac{1}{j\omega C}$

Most ultrasonic transducers, e.g. piezoelectric and electrostatic, will behave like capacitors. Since $j = \mathrm{e}^{j\frac{\pi}{2}}$ it is seen that a capacitor will cause a phase shift of -90° between the voltage and current. As the transducer resonates and dissipates energy it becomes more inductive causing the phase to increase, creating a peak in the phase frequency spectrum, in the position corresponding to the resonance frequency. The magnitude of the peak, i.e. the impedance phase value at resonance, indicates how much energy is being dissipated and is related to the transducer efficiency.

An Agilent impedance analyser (4294A) was used, connected to a PC via ethernet, and controlled by a LabView program.

2.4 Pressure and Directivity Measurements

The useful output from an air-coupled ultrasonic transducer is the pressure wave that propagates through the air. A large pressure signal is associated with larger displacements, which give larger responses from receivers and are hence easier to measure. The pressure amplitude for a given excitation voltage is a good measure of the transducer efficiency.

However, measuring the pressure amplitude alone is insufficient to fully characterise the transducer output. The directivity of the pressure wave emitted by the transducer is of equal importance. The directivity, sometimes referred to as the beam profile, shows how the wave spreads out from the transducer source, and how the pressure is distributed angularly.

A useful figure of merit is the beamwidth of a transducer. It can be defined as the angular range where the pressure amplitude is above -3 dB of the maximum amplitude. There is no single optimal number for beamwidth, as different ACU applications have widely varying requirements.

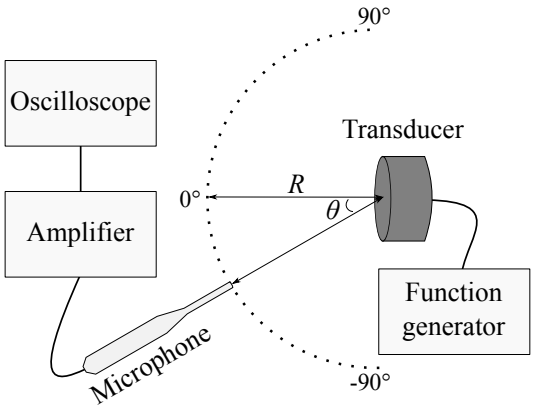

Figure 2.3: Schematic diagram of the setup for measuring the directivity of an ACU transducer.

Most ultrasonic transducer are axisymmetric, and it is only necessary to measure the pressure in one plane to get the full beam profile. The setup used in this research is shown in Fig. 2.3. A broadband (-3 dB at 150 kHz) acoustic microphone (BK 4138-A-015) was used to get accurate readings of the pressure. The microphone and amplifier were factory calibrated to give readings in volts per unit pascal (VPa^{-1}). Optical rails and a rotational stage were used to create the rotational arm, in order to sweep the microphone from $-90°$ to $90°$ at a fixed radius R away from the transducer's front face. The rotational arm had increments in steps of $2°$, with an estimated uncertainty $\pm 1°$, which is more than sufficient to accurately characterise all ACU systems encountered in this research.

For most conventional transducers the directivity is similar in both receive and transmit mode. That is, the transducer is most sensitive in the same direction in which it outputs the most pressure when transmitting. However, this is not always the case, and it is therefore useful to also characterise the receive directivity. This is most easily done by replacing the microphone in Fig. 2.3 with a uniform acoustic

source, which can then be swept to hit the investigated transducer from different angles.

2.5 Transmit-Receive Measurement

In transmit-receive (TX-RX) mode one transducer is used as generator and a second transducer as receiver as seen in Fig. 2.4. This is a common setup in different ACU applications, e.g. communication[55], flow metering and NDE[56]. This test is a good indicator of how well the transducer will actually work in these types of applications. Because pairs of transducers will not have perfectly overlapping bandwidths TX-RX measurements are also used to find pairs of transducers that are frequency matched. By comparing the input voltage or energy to the voltage from the receiving transducer the insertion loss (usually in dB) can be determined[57].

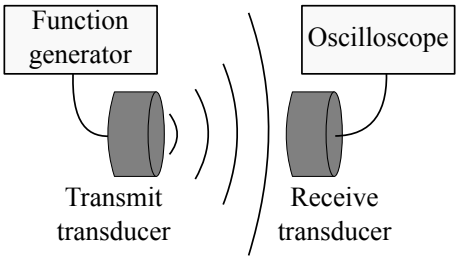

Figure 2.4: Schematic diagram of the ACU transmit-receive setup.

Chapter 3

Theory and Modelling of Vibrating Plates

To gain better understanding of flexural transducers and the underlying physics of their properties, an analytical model of the transducers was studied. The analytical theory provides physical insight into the fundamental behaviour of a system and gives predictions that can be experimentally corroborated. A full theoretical description of a flexural transducer, including all the bonds and the backing and the full geometry of the cap is not currently available, because of the complexity of the system. There are however a number of assumptions that can be made, which drastically simplify the problem. One of the most straightforward routes of analysing a flexural system is to use thin plate theory[58, 59], which is well understood. A flexural transducer, as illustrated in Fig. 1.11a, can be thought of as a thin, circular, metal plate, constrained along its outer boundary by the sides of the cap. It can therefore be modelled with a good level of accuracy as a circular, edge clamped, thin plate.

The definition of a thin plate is somewhat arbitrary, and is in general dependent on the ratio between thickness h and a lateral dimension a (e.g. the radius in the case of a circular plate). Very thin plates $a/h > 100$ lack flexural rigidity and would more correctly be referred to as membranes, as the restoring forces from a displacement are tensile membrane forces. Thick plates with $a/h < 10$ need to be treated similar to a bulk sample, with all components of stress and strain taken into account. The interesting region between membranes and thick plates $10 < a/h < 100$ contains all types of thin plates with some flexural rigidity. For small displacements, any membrane forces can be ignored, and the plate dynamics are governed by internal bending moments and transverse shear forces.

Even though a lot of understanding can be gained from a theoretical description alone, more realistic and accurate predictions of the system behaviour can be obtained from finite element (FE) modelling[48]. In an FE model the whole flexural transducer system, including piezoelectric materials and the load medium, can be modelled. Apart from more accurate predictions, the FE model has the potential of predicting wholly new features that arise from the complexity of the interactions between all individual parts that make up the whole transducer structure.

3.1 Theory of Vibrating Plates

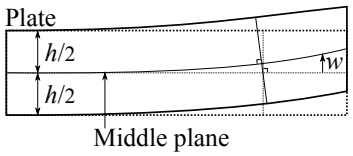

Figure 3.1: Schematic diagram of a thin plate with thickness h being deflected.

The equations describing the vibrations in circular, elliptical and rectangular plates with clamped, simply supported or free boundary conditions are derived in [60]. Consider a plate with thickness h as illustrated in Fig. 3.1. The general differential equation describing the transverse displacement of any thin plate in the range of a/h as set out above, regardless of shape and boundary conditions, is

$$D\nabla^4 w(\boldsymbol{r},t) + \rho\frac{\partial^2 w(\boldsymbol{r},t)}{\partial t^2} = 0, \tag{3.1}$$

where D is the rigidity of the plate defined in equation (3.2), w is the transverse displacement, $\boldsymbol{r}$ is the position vector and ρ is the area density. The rigidity is given by[60]

$$D = \frac{Eh^3}{12(1-\nu^2)}, \tag{3.2}$$

where E is Young's modulus and ν the Poisson ratio. In order to derive equation 3.1 there are some necessary assumptions

1. The plate material is elastic, homogenous and isotropic.
2. The plate is initially flat ($w(\boldsymbol{r}, t=0) = 0$).
3. Deflections are small compared to the plate thickness ($w << h$).

4. Straight lines, initially perpendicular to the middle plane of the plate, remain perpendicular and constant in length during bending.

5. The stress perpendicular to the middle plane is small compared to other stress components.

6. The middle surface is unstrained after bending, because displacements are small.

The assumptions are known as Kirchhoff's hypotheses[58], and essentially reduce the need for a three dimensional analysis of plate bending to a two dimensional analysis. For example, assumption 3 which asserts that displacements are small in comparison to the thickness, means that the slope is very small and the square of the slope can be neglected. After applying all the assumptions the resulting theory is known as Kirchhoff's plate theory.

To solve equation (3.1) we assume the displacement has the general harmonic form

$$w(\boldsymbol{r}, t) = W(\boldsymbol{r})\cos(\omega t), \tag{3.3}$$

where W is the position dependent displacement amplitude normal to the plate and ω the angular frequency of the vibrations. Substituting equation (3.3) into (3.1) gives

$$\nabla^4 W - \frac{\rho\omega^2}{D} W = 0. \tag{3.4}$$

Define $k^4 = \frac{\rho\omega^2}{D}$ and rearrange equation (3.4):

$$(\nabla^2 - k^2)(\nabla^2 + k^2)W = 0. \tag{3.5}$$

This gives us the two equations

$$\begin{aligned} (\nabla^2 + k^2)W &= 0 \\ (\nabla^2 - k^2)W &= 0, \end{aligned} \tag{3.6}$$

which are the Helmholtz and modified Helmholtz equations respectively[61].

3.1.1 Solutions for Circular Plates

For circular plates we can use $r = |\boldsymbol{r}|$, which is the distance from the centre of the plate. Using polar coordinates the Helmholtz equations (3.6) can be solved by

separation of variables, $W(r,\theta) = R(r)\Theta(\theta)$, which gives

$$\begin{aligned}
&\frac{\Theta}{r}\frac{d}{dr}\left(r\frac{dR}{dr}\right) + \frac{R}{r^2}\frac{d^2\Theta}{d\theta^2} \pm k^2 R\Theta = 0 \\
&\frac{r}{R}\frac{d}{dr}\left(r\frac{dR}{dr}\right) + \frac{1}{\Theta}\frac{d^2\Theta}{d\theta^2} \pm k^2 r^2 = 0 \\
&\frac{r}{R}\frac{d}{dr}\left(r\frac{dR}{dr}\right) \pm k^2 r^2 = -\frac{1}{\Theta}\frac{d^2\Theta}{d\theta^2} = \text{const.} = n^2.
\end{aligned} \tag{3.7}$$

From equation (3.7) we get two ODEs, one for each polar coordinate, equal to the same constant that has been arbitrarily denoted n^2. Due to the periodic 2π boundary condition of a circular plate, solutions to the angle dependent equation are of the form $\mathrm{e}^{\pm jn\theta}$ with $n =$ integer. Writing out the radial equations explicitly gives

$$r^2\frac{d^2R}{dr^2} + r\frac{dR}{dr} + (k^2r^2 - n^2)R = 0 \tag{3.8}$$

$$r^2\frac{d^2R}{dr^2} + r\frac{dR}{dr} - (k^2r^2 + n^2)R = 0, \tag{3.9}$$

where equation (3.8) is Bessel's differential equation and (3.9) is the modified Bessel equation, in the independent variable kr[61]. Solutions to equation (3.8) are the Bessel functions of first and second kind, denoted $J_n(kr)$ and $Y_n(kr)$ respectively, and any linear combination of the two. Similarly, the solutions to equation (3.9) are the modified Bessel functions of first and second kind, denoted $I_n(kr)$ and $K_n(kr)$ respectively, and any linear combination of the two.

For the specific example of a solid, circular plate some simplifications can be made. Assuming there is no hole at the centre of the plate, to avoid infinite stresses and deflections, both $Y_n(kr)$ and $K_n(kr)$ are eliminated. Only Bessel functions of the first kind, for positive, integral n are regular at the origin. Also, assuming that the boundary conditions around the plate are symmetrical (w.r.t. one or more diameters) the non-symmetrical terms from the angular function $\Theta(\theta)$ can be removed. Thus for a circular, solid plate the general equation for the amplitude of a mode n is

$$W_n(r,\theta) = [A_nJ_n(kr) + B_nI_n(kr)]\cos(n\theta), \tag{3.10}$$

where A_n and B_n are constant coefficients determined by the boundary conditions. Looking at the angular dependence of equation (3.10) it is seen how n specifies the number of nodal diameters, due to its position in the argument of the cosine factor. Hence, all axisymmetric modes require $n = 0$. The mode shape of any axisymmetric

mode is therefore described by

$$W(r) = AJ_0(kr) + BI_0(kr). \tag{3.11}$$

To illustrate how the mode shapes and frequencies can be predicted by equation (3.10) a plate clamped uniformly along its outer edge is considered. The boundary conditions of a clamped plate, of radius $r = a$, can be expressed as

$$\begin{aligned} W(a) &= 0 \\ \left.\frac{\partial W}{\partial r}\right|_a &= 0, \end{aligned} \tag{3.12}$$

i.e. there is no displacement or gradient of displacement along the edge of the plate. Substituting equation (3.10) into equations (3.12) gives, for non trivial solutions, the characteristic determinant

$$\begin{vmatrix} J_n(\lambda) & I_n(\lambda) \\ J_n'(\lambda) & I_n'(\lambda) \end{vmatrix} = 0, \tag{3.13}$$

where $\lambda = ka$, and primes denote differentiation w.r.t. kr. The following recursion relations apply to Bessel functions and their first derivatives [61]

$$\begin{aligned} \lambda J_n'(\lambda) &= nJ_n(\lambda) - \lambda J_{n+1}(\lambda) \\ \lambda I_n'(\lambda) &= nI_n(\lambda) + \lambda I_{n+1}(\lambda), \end{aligned} \tag{3.14}$$

which when applied to the characteristic equation (3.13) can be used to eliminate the primed functions to give

$$J_n(\lambda)I_{n+1}(\lambda) + I_n(\lambda)J_{n+1}(\lambda) = 0. \tag{3.15}$$

The roots of equation (3.15) are the eigenvalues λ, which can easily be found through numerical methods. Table 3.1 shows the first few eigenvalues for $n = 0, 1, 2, 3$. Fig. 3.2 shows the positions of the nodal lines for a plate in vibration mode (m, n) for $m, n = 0, 1, 2$. It can be seen that the nodal radius increases for modes with one or more nodal diameters, which can be understood as the system minimising its energy by reducing the slope of displacement close to the centre.

By the definition of k (and hence λ) the mode frequency ω is related to λ by

$$\omega = \left(\frac{\lambda}{a}\right)^2 \sqrt{\frac{D}{\rho}}. \tag{3.16}$$

Table 3.1: The first seven roots (λ) of equation (3.15) corresponding to the modes of a clamped, circular plate. n corresponds to the number of nodal diameters and m to the number of nodal radii. The column with $n = 0$ represents the axisymmetric modes.

m \ n	0	1	2	3
0	3.19625	4.61085	5.90565	7.14355
1	6.30645	7.79925	9.19685	10.5366
2	9.43945	10.958	12.4022	13.795
3	12.5771	14.1086	15.5794	17.0052
4	15.7164	17.2557	18.7439	20.1923
5	18.8565	20.401	21.9014	23.3662
6	21.997	23.5453	25.0548	26.5321
7	25.1379	26.6889	28.2054	29.6926

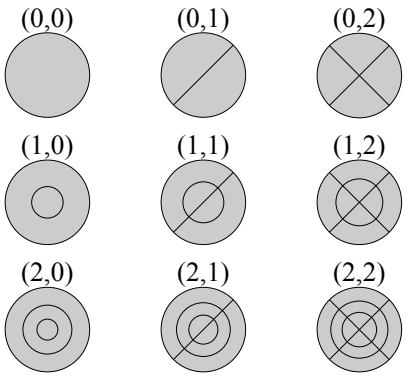

Figure 3.2: Nodal lines of a an edge clamped plate in vibration mode (m, n) for $m, n = 0, 1, 2$. The nodal radii of each mode are accurately scaled.

The specific mode shape can then be determined by applying one of the boundary condition equations (3.12) to equation (3.10), replacing ka with the eigenvalue λ of the mode of interest. Fig. 3.3 shows the normalised mode shapes of four modes. These mode shapes are important for predicting the acoustic beam profile that a particular mode will produce.

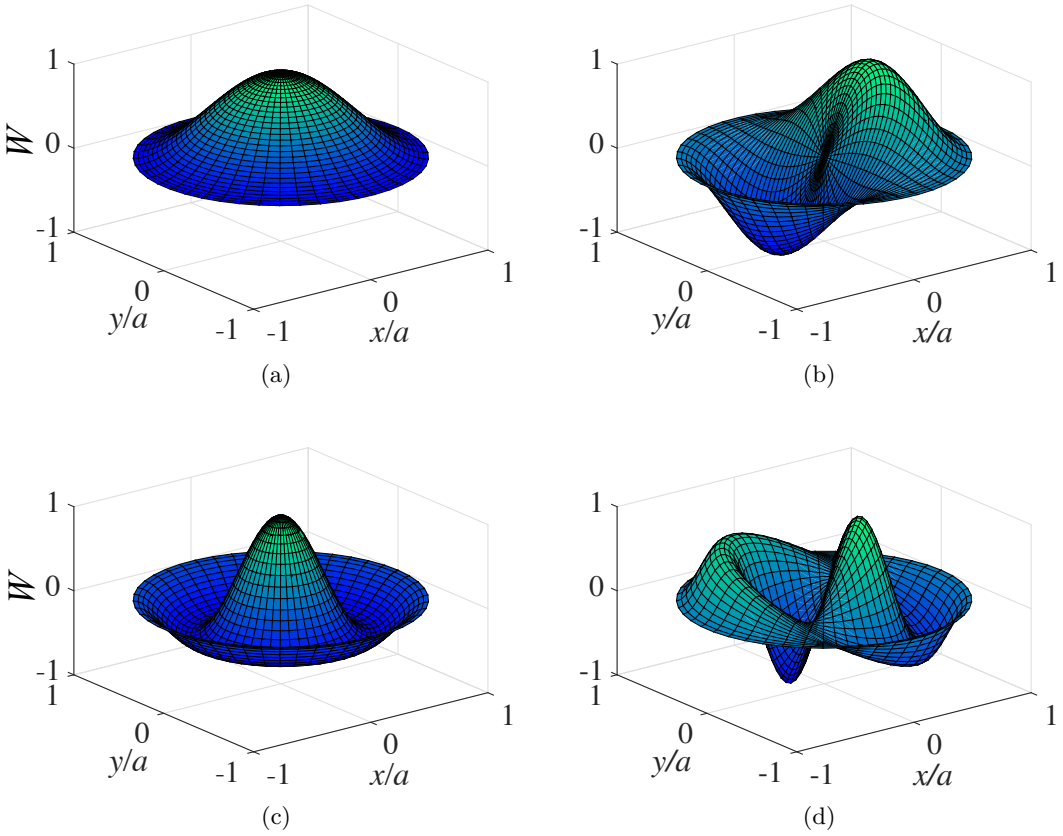

Figure 3.3: Normalised theoretical mode shapes $W(r, \theta)$ for vibration modes (a) (0,0), (b) (0,1), (c) (1,0) and (d) (1,1).

Two other boundary conditions of importance relate to completely free plates and simply supported plates, which are treated extensively in [60]. For the flexural transducer, described in §1.2.5 and depicted in fig. 1.11, the actual boundary conditions are more complicated than the three mentioned. The edge of the plate is not rigidly fixed, yet its motion is impeded by the sides of the cap. This situation could potentially be modelled as a plate uniformly supported along the edge by springs. The spring constant would be determined by the thickness and material properties of the sides of the cap.

3.2 Finite Element Modelling of Flexural Transducers

As mentioned earlier, an analytical approach to a full 3D transducer system is not possible because of the level of complexity. FE methods[62] provide a solution, which has been shown to be successful for ultrasonic problems.

FE methods divide a model into a number of sub-domains, referred to as elements. It is a discretisation procedure of a continuous system. The elements are connected at certain points referred to as nodes. A simple exemplary system is illustrated in Fig. 3.4. Although the illustration portrays the element as a rectangle or a cuboid, other geometric shapes such as triangles are not uncommon. Field values, such as velocity, in an element is determined by interpolation between bounding nodes. Each node is associated with a set of predefined parameters, such as stiffness and mass, determined by the material in the model.

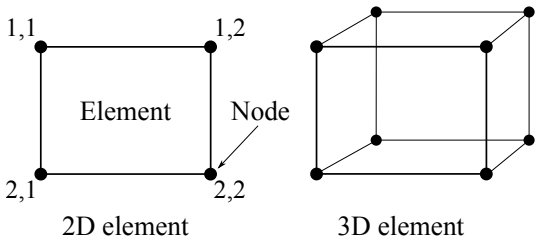

Figure 3.4: Depiction of rectangular and cuboid elements and nodes.

The FE method then works as follows. A force $F(t)$ is applied to a node or a set of nodes. The force may be time varying, but takes on a single value for the time step t. Velocities $v(t)$ caused by the force $F(t)$ are calculated given the material parameters of the node. From the velocities $v(t)$ of each node the forces $F(t + \delta t)$ are determined and applied to the nodes to update the velocity $v(t + \delta t)$. Hence the system iteratively develops in time in steps of δt. FE methods can also be used in the frequency domain, which translates from the time domain via Fourier transformation.

To determine an appropriate size of each element, i.e. δx and δy between nodes, some knowledge of the dynamic behaviour of the system is required. Specifically, there should be at least two nodes per smallest wavelength of interest. In essence it is a spatial Nyquist criteria. If the element size is bigger, the dynamics of these wavelengths will be missed or aliased down to look like a longer wavelength phenomenon. In practise it is common to use more than two nodes per wavelength for better resolution. It might appear that the optimal solution would be to make the elements arbitrarily small, but this can unnecessarily waste computational re-

sources. Once the Nyquist criteria has been satisfied the results from decreasing the element size start to converge to a point where no new information or significant improvement in precision can be achieved. It is good practice to make short runs with relatively large element sizes to initially evaluate the model, and then successively decrease the element size until the results from subsequent runs converge.

FE methods are not useful without computer implementation, in order to run these computationally intense iterations. Several commercial software packages specialising in FE analysis exist. In this research the software package PZFlex (Weidlinger Associates Inc., USA) was used, as it has been optimised for ultrasonic simulations. It is important that the specific implementation of the finite element model can handle large displacements, in order to accurately simulate flexural behaviour. PZFlex also offers built in extrapolation tools, which allows field variables (such as pressure and displacement) far away from the ultrasonic source to be calculated without having to extend the meshed region of the FE model, which could potentially cost significant amounts of computation time. Although the theory in section §3.1.1 treats both axisymmetric ($n = 0$) and non-axisymmetric modes, often we will be mostly concerned with the former. It is therefore expedient to reduce the full 3D transducer system to a 2D axisymmetric model, which saves significant amounts of computation time.

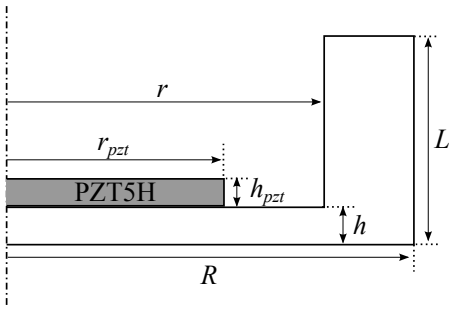

Figure 3.5: Diagram with labeled dimensions of the axisymmetric FE model used to simulate a piezoelectric flexural transducer. Models with the different cap materials aluminium, stainless steel and titanium were made.

The standard model used for FE analysis is illustrated in Fig. 3.5. It has the essential features of a flexural transducer, as introduced in §1.2.5, with a piezoelectric element bonded to the inside of a metal cap. Simulation without the piezoelectric element, where the cap is actuated by a time varying pressure load function, were also carried out.

3.3 Conclusions

From the theoretical calculations using equation (3.16), which relates frequency to plate dimensions and material properties, and substituting in values for λ from Table 3.1, the frequency of a mode can be predicted. The numerous assumptions that have been made and the simplicity of the model limits the accuracy, but it is a quick way of obtaining an approximate figure for the resonance frequencies. The dimensions of a specific frequency from the theory can be implemented in the FE model, and then fine tuned to give a specific response.

The frequency dependence on the dimensions can be seen by substituting the expression for the rigidity D in equation (3.2) into equation (3.16), which gives the two relations

$$\begin{aligned} \omega &\propto h \\ \omega &\propto \frac{1}{a^2}, \end{aligned} \tag{3.17}$$

i.e. the mode frequency is linear with the thickness of the plate and inversely proportional to the square of the plate radius. In general then an edge clamped circular plate with any given mode frequency could be fabricated. However, this is only true in the limited extent of the assumptions of the thin plate theory. The frequency could be increased indefinitely by increasing the plate thickness relative to the plate radius, but soon the plate would be too thick for the derivation of the frequency equation (3.16) to be valid. A similar argument is true for the radius.

The FE model provides a convenient way of checking the predictions from the theory, without having to assemble a transducer and test it empirically. It allows more complex systems, including the entire transducer system as well as the load medium to be simulated.

Chapter 4

Piezoelectric Flexural Transducers

Macroscopic piezoelectric flexural transducers need to be better understood and further developed to become useful for a wider range of applications, where the inherent robustness and transduction efficiency can be exploited. Some applications such as imaging, NDT and flow metering would benefit from higher frequency (¡70 kHz) flexural transducers. To do this, in depth characterisation of flexural transducers is necessary. The transducers can be characterised in terms of their resonance behaviour, their mode frequencies $f_{m,n}$ and mode shapes $W_{m,n}(r)$, displacement amplitude, electrical impedance and pressure output. The background of the flexural behaviour from the thin plate theory was covered in the previous section. Here follows an in depth analysis of piezoelectrically actuated flexural transducers.

4.1 Piezoelectricity

Though many methods for ultrasonic generation exist, piezoelectricity is still used for the majority of applications. It is therefore important to have an understanding of the underlying physics of the piezoelectric effect, and of how the material parameters of a piezoelectric element relate to ultrasonic transduction.

A piezoelectric material will, when subjected to stress, develop a potential difference across opposing faces, which is known as the direct piezoelectric effect. The indirect (or inverse) piezoelectric effect occurs when an external potential difference is applied across the opposing faces, which induces a strain in the piezoelectric element. The effect has been demonstrated for frequencies up to terahertz, which is why the indirect effect can be used to generate ultrasonic waves and the direct

effect can be used to sense ultrasonic waves.

In order for a material to be piezoelectric, the cells of the crystal structure need to lack a centre of symmetry. The lack of symmetry is not sufficient by itself to ensure piezoelectricity, but it is a necessary condition. Of the 32 crystallographic point groups there are 21 crystal systems without a centre of symmetry, of which 20 exhibit piezoelectricity.

The commonly used material lead zirconate titanate (PZT) has a so called perovskite crystal structure, as shown in Fig. 4.1. The unit cell features a positive Ti or Zr ion inside a octahedron of negative oxygen ions, with a cube of positive Pb ions around it. At zero temperature, i.e. when the atoms have no kinetic energy, the bonds between the oxygen ions push the central ion out of the centre, creating an electric dipole moment and hence polarisation. It is only when the temperature reaches the Curie temperature T_C, that the system assumes a centrosymmetric alignment and the polarisation disappears. The Curie temperature for commonly used varieties of PZT is $T_C \approx 300°\text{C}$.

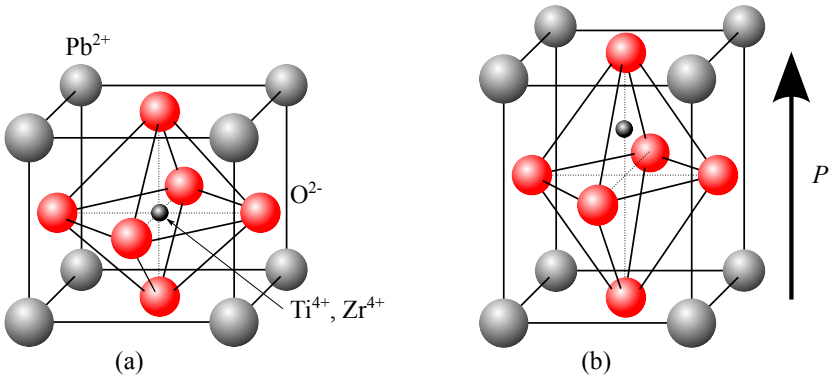

Figure 4.1: The PZT perovskite crystal structure in (a) its symmetric form, which occurs above the Curie temperature, and (b) in its non-symmetric form, which gives rise to spontaneous polarisation in the indicated direction below the Curie temperature.

Polarisation is a vector quantity, and PZT neighbouring cells will tend to have aligned polarisation in so called domains. The polarisation direction of individual domains is however random, which means that there is no net polarisation. The domains can however be aligned by subjecting the crystal to a strong electric field, which is called poling. Usually voltages in the order of kV are used with the piezoelectric element submerged in oil, at an elevated temperature $\approx T_C$, over a time period of hours. After the poling process, the material will keep its net polarisation provided it is not subjected to temperatures $> T_C$[63].

4.1.1 Mathematical Formulation of Piezoelectrcity

To gain a proper understanding of piezoelectricity, the relation between the electric and mechanical properties need to be formulated mathematically. Because of anisotropic behaviour of piezoelectric materials, a full 3D representation is most appropriate, although some simplifications have been made in order to highlight the traits important for ultrasonic transduction applications. In the following section tensor notation and the Einstein convention of summation over repeated indices are used. Bold letters indicate vector or matrix quantities.

The constitutive equations of piezoelectricity can be derived from the electric Enthalpy function $H(\boldsymbol{\epsilon}, \boldsymbol{E})$[64], which is defined as

$$H(\boldsymbol{\epsilon}, \boldsymbol{E}) = c_{ijkl}\epsilon_{ij}\epsilon_{kl} - \frac{1}{2}\kappa_{ij}E_iE_j - e_{ijk}\epsilon_{ij}E_k, \tag{4.1}$$

where c is the generalised elastic constant (at constant electric field) known as the stiffness tensor, ϵ is the strain tensor, κ is the dielectric constant or relative permittivity (at constant strain), and E is the electric field. H sums up the energy of a piezoelectric system with material properties defined by c, κ and e under strain ϵ and in an electric field E. From the enthalpy, expressed here in terms of independent variables $\boldsymbol{\epsilon}$ and $\boldsymbol{E}$, the electric displacement $\boldsymbol{D}$ and stress tensor σ are given by differentiation with respect to electric field and strain respectively[65]

$$D_i = -\frac{\partial H(\boldsymbol{\epsilon}, \boldsymbol{E})}{\partial E_i} = \kappa_{ij}E_j + e_{ijk}\epsilon_{jk} \tag{4.2}$$

$$\sigma_{ij} = \frac{\partial H(\boldsymbol{\epsilon}, \boldsymbol{E})}{\partial \epsilon_{ij}} = c_{ijkl}\epsilon_{kl} - e_{ijk}E_k \tag{4.3}$$

Equations (4.2) and (4.3) are known as the piezoelectric constitutive equations. The electric displacement equals the familiar electric field term plus an induced polarisation term, from the interaction between strain and piezoelectrcity. Equation (4.3) can most readily be interpreted as an extension to the general theory of elasticity[66, 67], by subtracting from the strain term the piezoelectric contribution to the stress due to the electric field $\boldsymbol{E}$.

It can sometimes be helpful to use other independent variables in the enthalpy function H, in order to derive other constitutive relations. For example by using $\boldsymbol{\sigma}$ and $\boldsymbol{E}$ as independent variables the strain is given by

$$\epsilon_{ij} = c_{ijkl}\sigma_{kl} + d_{ijk}E_k, \tag{4.4}$$

where d is another piezoelectric constant similar to e, which relates strain to electric

field, and is referred to as the piezoelectric charge constant. Both the stiffness tensor c and the piezoelectric coefficient d can be simplified by taking into account the particular crystal symmetries and boundary conditions of the piezoelectric sample considered. For PZT, which belongs to one of the 21 non-centrosymmetric point symmetry groups denoted $4mm$[67], there are only 3 independent variables in the piezoelectric tensor. Using the reduced index notation $d_{ijk} = d_{ip}$ for $i = 1, 2, 3$ and $p = 1, ..., 6$, where $11 \rightarrow 1$, $22 \rightarrow 2$, $33 \rightarrow 3$, 23 or $32 \rightarrow 4$, 13 or $31 \rightarrow 5$, and 12 or $21 \rightarrow 6$, the piezoelectric coefficient can be represented by the matrix

$$\boldsymbol{d} = \begin{pmatrix} 0 & 0 & 0 & 0 & d_{15} & 0 \\ 0 & 0 & 0 & d_{15} & 0 & 0 \\ d_{31} & d_{31} & d_{33} & 0 & 0 & 0 \end{pmatrix}. \tag{4.5}$$

The d_{33} component is of particular interest for ultrasonic transduction, as it relates the strain in the z direction due to an electric field applied along the same axes, which is the case for the majority of poled piezoelectric elements used for transduction. The value of d_{33} is a common figure of merit for piezoelectric elements and can be experimentally determined by measuring the transverse surface displacement, to calculate the strain, for a known applied electric field[68].

For flexural transducers of the type described in this work, the d_{31} is more significant in terms of transduction, as it is the lateral strain that causes the unimorph system to bend. There are however other properties, such as mechanical flexibility, which need to be taken into account when choosing the optimal piezoelectric material.

4.2 Equivalent Circuit

Piezoelectric systems can be represented by an equivalent circuit model, which can be used to analyse the electric response, impedance and energy conversion of a transducer. Fig. 4.2 shows the so called Van Dyke model[69] for a piezoelectric element close to resonance, which is a commonly used equivalent circuit model. The Van Dyke model is a parallel connection of a series LCR representing mechanical damping mass and elastic compliance, and a capacitor (C_0) representing the electrostatic capacitance between the two parallel plates of the piezoelectric element. R_1 represents the mechanical dissipation, and the mechanical quality factor Q_m can be estimated by

$$Q_m = \frac{\sqrt{L_1/C_1}}{R_1}. \tag{4.6}$$

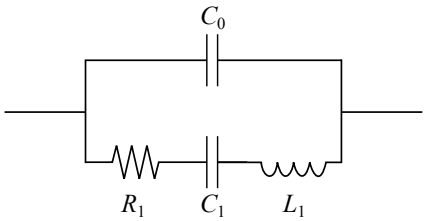

Figure 4.2: Van Dyke equivalent circuit model of a piezoelectric element close to resonance.

The value of R_1 is relevant to the speed that the resonance peak decays at. The larger the value of R_1, the faster the peak will decay. The physical meanings for the components of the circuit model can be understood here. The component C_0 represents the dominant capacitance of the piezoelectric element, the components L_1, R_1 and C_1 are relevant to the equivalent mass m, damping coefficient c, and spring constant k respectively of the piezoelectric element.

The Van Dyke model works well for simple piezoelectric systems with only one resonance, or only one local resonance. In a narrow frequency band close to the resonance frequency the electronic parameters are constant (frequency independent), as long as the given resonance mode is sufficiently isolated from other modes. The model does not accurately characterise systems with significant material losses, for which the Sherrit model[70] or more recently the Guan model[71] can be used.

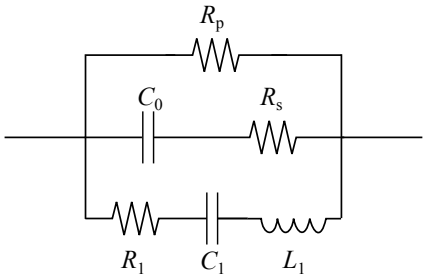

Figure 4.3: Guan equivalent circuit model, which considers both the resonant and non-resonant frequency regimes of a piezoelectric system.

The Guan equivalent circuit is shown in Fig. 4.3. R_s and R_p (series and parallel resistances respectively) represent the mechanical energy losses. Specifically, the resistance R_s incorporates the energy dissipation associated with the hysteresis of the electrical displacement and the electric field, which exists for ferroelectric materials such as piezoceramics. Unlike for the Van Dyke and Sherrit models, where the circuit parameters can be calculated from the material properties of the piezo-

electric element, the circuit parameters of the Guan model have to be determined from measurements of the impedance of the system.

The impedances of the non-resonant and resonant parts of the circuit are given respectively by

$$\begin{aligned} Z_{nr}(\omega) &= R_p \times (R_s + 1/(i\omega C_0)) \,/\, (R_p + R_s + 1/(i\omega C_0)) \,, \\ Z_r(\omega) &= R_1 + i\omega L_1 + \frac{1}{i\omega C_1}. \end{aligned} \tag{4.7}$$

To determine the circuit values, the dominant capacitance C_0 is first considered from the impedance measurement. After a value of C_0 is chosen C_1 is determined from the appearance of both the impedance magnitude and phase around the resonance peak. The smaller the value of C_1/C_0, the narrower the bandwidth of the peak. Usually, for an unloaded piezoelectric element, L_1 relates to C_1 and the resonance frequency f_1 by[71]

$$f_1 = 1/(2\pi\sqrt{L_1 C_1}). \tag{4.8}$$

For a piezoelectric system attached to a structure, as in the case of a flexural transducer, there are multiple resonances often closely spaced in frequency. To accommodate for this behaviour, additional LCR circuits are added in parallel with R_n, C_n and L_n corresponding to the n^{th} resonance mode.

4.3 Construction

The construction process of the flexural transducer, although seemingly straightforward, went through several iterations of improvements. The construction appears simple because of the clean design and the small number of individual parts that need to be assembled.

In terms of materials for the passive layer, aluminium, stainless steel and titanium were considered. Three important elastic constants of the materials are shown in Table 4.1. Aluminium is light and easy to machine, combined with good elastic properties for flexural transduction. Stainless steel is less suitable for flexural transduction, due to a higher rigidity which decreases the displacement of a plate for a given applied force, but is more suitable for industrial applications due to greater mechanical strength. Titanium is a suitable compromise, with good elastic properties for flexural transduction and high mechanical strength. The downsides of titanium are high material costs and difficult machining.

The first set of prototype transducers was made from aluminium. Caps were

	Aluminium	Stainless	Titanium
E (GPa)	69	190	116
ρ (kgm^{-3})	2700	7960	4510
ν	0.33	0.3	0.32

Table 4.1: Elastic constants of aluminium, stainless steel and titanium. The constants are used to calculate the rigidity D of a plate in equation (3.2)

machined by the Physics Department's mechanical workshop using a metal lathe. A metal rod with the required outer diameter was cut into sections of the right length, and the lathe was used to hollow out the centre. A thin layer of two component epoxy (Araldite-2014) was applied to a thin disc of PZT5H and pushed into the centre of the cap. The disc was aligned manually to the centre of the cap and left to cure at atmospheric pressure and room temperature for 24 hours. At this early stage of the research the aim was to observe flexural vibrations in such a system, and to compare observed frequencies with those predicted from the analytical model and FE methods. Despite the very simple construction procedure, flexural behaviour was observed, as is presented in the next section, and there was general agreement between experiment and theory.

However, significant differences between nominally identical transducers were observed. There were disagreements in terms of mode frequencies, mode shapes and vibration amplitudes. Trying to confirm the accuracy of any model then became difficult, since different transducers behaved more or less in accordance with the theory and FE model.

From the theoretical analysis and the FE methods it was known that small variations in the dimensions of the plate thickness and radius could have a significant impact upon the mode frequencies. The differences in mode shapes and amplitudes were hypothesised to originate from inconsistencies in bonding the piezoelectric element. If the disc is not properly centred in the cap, the system loses some symmetry, which would be expected to affect the mode shapes. The strength and thickness of the bond will have bearing on the transfer of energy from the disc to the cap, and would therefore affect the amplitude of the vibrations.

At first the metal lathe was replaced by a CNC machine for constructing caps. However, the tolerance was still deemed too great, and in the end ready made caps were procured from an external supplier. This limited the choice of dimensions, but greatly improved consistency and therefore also the analysis.

To improve the bond and consistency in the bonding process, a new assembly procedure was developed, which is illustrated in Fig. 4.4. In short, a piston and collar

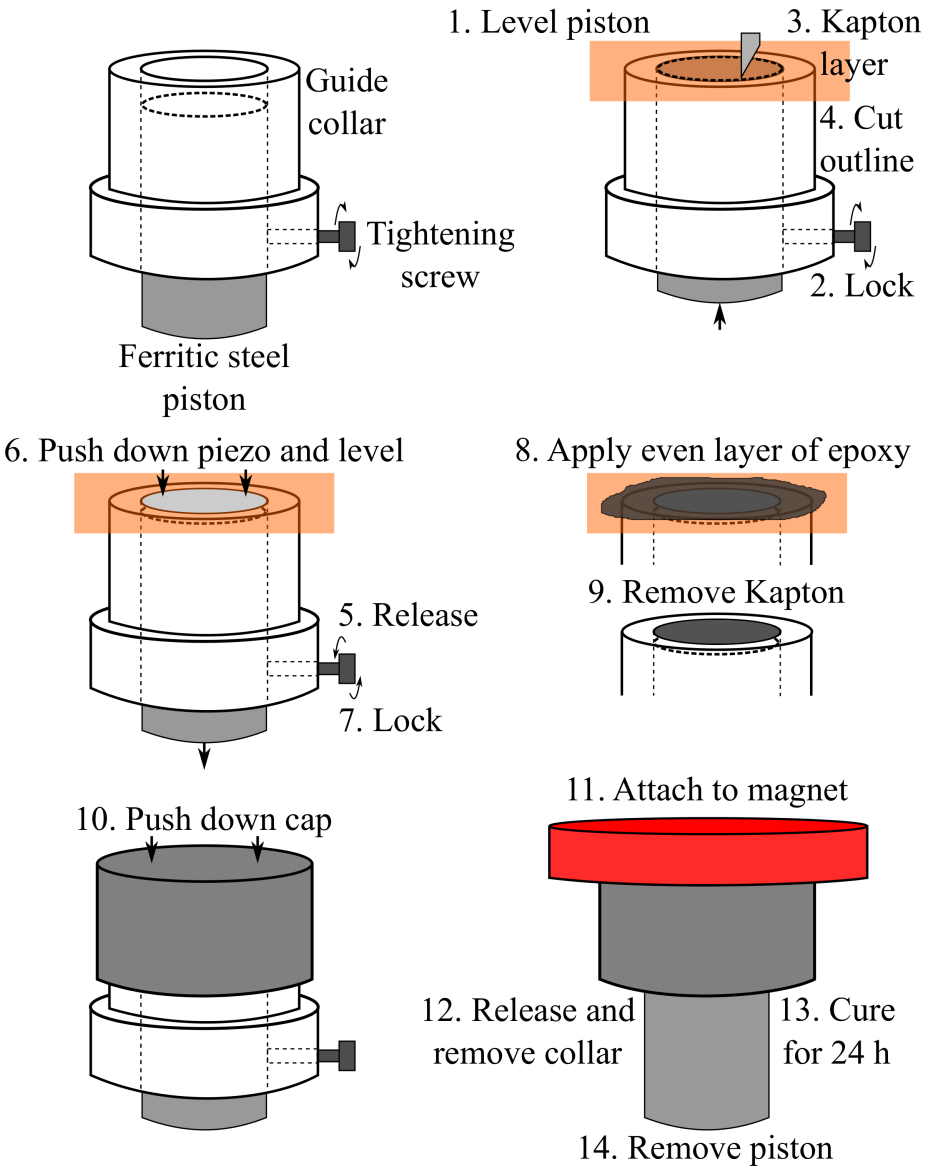

Figure 4.4: Step by step guide to the bonding procedure for consistent bond strength and piezo centering.

were used to centre the piezoelectric disc inside the cap. The piston is made of ferritic steel, which together with a magnet produced a consistent pressure to the disc during the curing procedure. The amount of pressure was regulated by the strength of the magnet, and was kept consistent between transducers by using the same magnet for each transducer in a set. For piezoelectric discs with a wrap around electrode connections were soldered to the disc. Spring contacts and conductive epoxy were also tested, but did not perform as well.

4.3.1 Flexural Array Construction

To make an array of piezoelectric flexural transducers, instead of assembling individual caps to populate the array, a novel approach was developed where a semi-rigid baffle is bonded to a single thin sheet of metal. The baffle is essentially a plate with holes in it, which defines the flexural elements on the metal plate by restricting the displacement amplitude around the holes similar to the sides of a cap. The construction process is illustrated in Fig. 4.5. A similar concept for making a 70 kHz immersion transducer was found in [72].

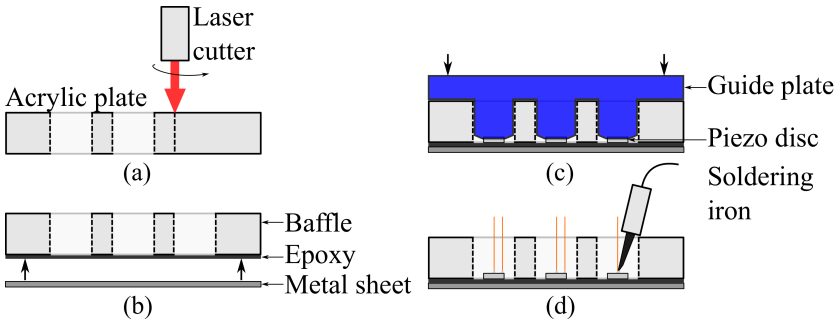

Figure 4.5: Step by step construction guide of flexural array transducer, using a single sheet of metal and a baffle back structure. (a) The baffle is made by machining an acrylic plate with a computer controlled laser cutter. (b) The baffle is bonded to the metal plate using a two component epoxy. (c) The piezoelectric discs are bonded to the plate using a 3D printed guide and the same epoxy is applied to the ground electrode. (d) Connections are soldered to the piezoelectric elements.

Two different types of baffles and with different manufacturing techniques were tested. The first prototype was used with an acrylic sheet as in Fig. 4.5, which was patterned using a laser cutter. The second array was made using a 3D printed baffle from ABS plastic. Both techniques offer a lot of customisation, with the laser cutter having better precision. The baffle was bonded using two component epoxy

(Araldite-2014). However, when bonding a plastic to a metal it was difficult to achieve sufficient bond strength, and in some trials the baffle was easily peeled off the metal. Pre-treating both surfaces with acetone alleviated the problem to some extent, but the existence of more appropriate bonding procedures should not be ruled out.

Piezoelectric discs with wrap-around electrodes were used in the arrays, and connections were soldered to each electrode. Similar to the procedure for the single element flexural transducer, thin (0.08 mm) enamelled copper wires were used at the piezoelectric end, to limit mass loading. The wires were connected to a fixed structure at the other end for strain relief with coaxial cables coming out of the structure. This setup allowed each element of the array to be driven separately.

Although the technique illustrated in Fig. 4.5 was used to make a 2D 3×3 array, the method is applicable to a large variety of array layouts. The ease of customisability is one of the benefits of the assembly technique. It is of interest for future research to investigate non-circular elements and novel array patterns[51].

4.4 Results

4.4.1 ProWave Transducer

A first set of measurements were made on a commercial 40 kHz flexural ultrasound transducer from ProWave (400ET250). The nominal operating frequency of 40 kHz corresponded to the (1,0) mode with a measured frequency of 39.8 kHZ. The measured fundamental (0,0) mode was at 6 kHZ, which puts it in the audible part of the spectrum. Fig. 4.6 shows the frequency spectrum from the transducer.

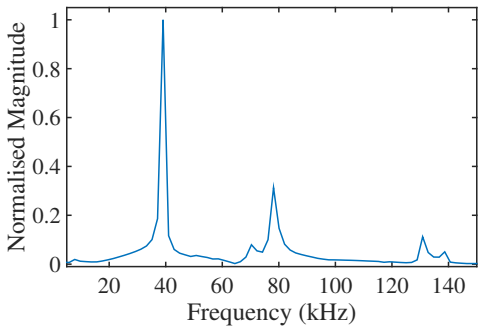

Figure 4.6: Frequency spectrum from commercial air-coupled ProWave transducer, excited by a single cycle 80 kHz sinusoidal wave.

The spectrum was produced by Fourier transforming a displacement signal

from the centre of the front face of the transducer, when the transducer was excited by a single cycle sinusoidal, 80 kHz signal. Clearly the dominant mode is at 40 kHz, with the fundamental mode barely visible. The mode shape at 40 kHz was measured by a laser vibrometer area scan of the transducer front face, as described in §2.2, and is displayed in Fig. 4.7.

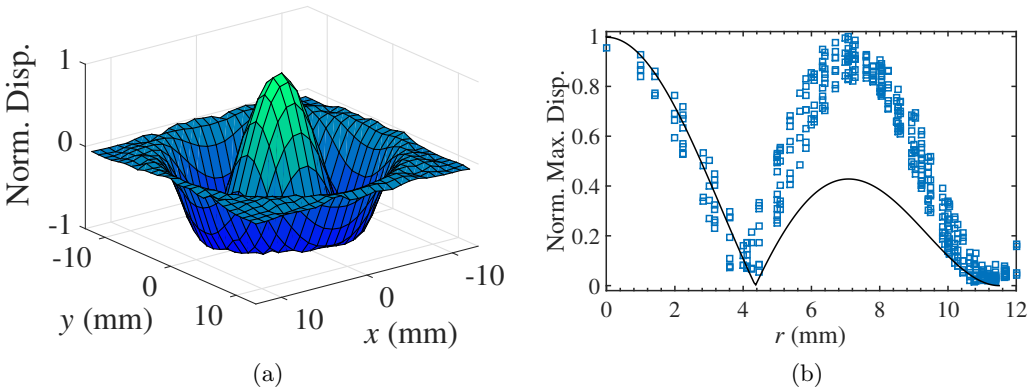

Figure 4.7: Experimental mode shape of commercial air-coupled ProWave transducer excited by a windowed sine function with $f = 39.8$ kHz. (a) Surface snapshot of displacement at time of maximum centre displacement. (b) Normalised, peak-to-peak displacement of each point plotted against the radial distance away from the centre of that point (□) and the theoretical mode shape $|W(r, 0)|$ (—) for comparison.

As seen in Fig. 4.7b the measured amplitude of the outer antinode, at $r \simeq 7$ mm, is approximately 100% greater than that of a clamped plate of similar dimensions. The effect is explained by the presence of a piezoelectric element, which effectively adds stiffness and mass loading to the centre portion of the plate, which limit the amplitude of the central antinode. From the dimensions of the transducer, ignoring the piezoelectric element, the predicted theoretical frequency from equation (3.16) is $f_{1,0} = 39.7$ kHz, which is in excellent agreement with the experimental value of (39.8 ± 0.1) kHz.

4.4.2 Aluminium Cap with $f_{0,0} \simeq 50$ kHz

A passive layer made of aluminium, with dimensions $h = 0.5$ mm, $r = 4.5$ mm, $R = 5.5$ mm and $L = 5$ mm, was made and characterised. For details regarding the experimental setup and characterisation techniques the reader is referred back to Chapter 2.

Using the laser generation and detection technique (as described in §2.1) the

frequency spectra of the caps, without any piezoelectric element, were determined. Fig. 4.8a shows the transient displacement from the centre of the front face of an aluminium cap. There is a predominant low frequency wave, with higher frequency signals superposed. The associated frequency spectrum is shown in Fig. 4.8b. The spectrum shows a strong peak at $\simeq 50$ kHz, which matches the designed fundamental resonance of the cap. Also there is no significant magnitude at lower frequencies. Though of lesser magnitude some higher frequency modes are also apparent in the spectrum.

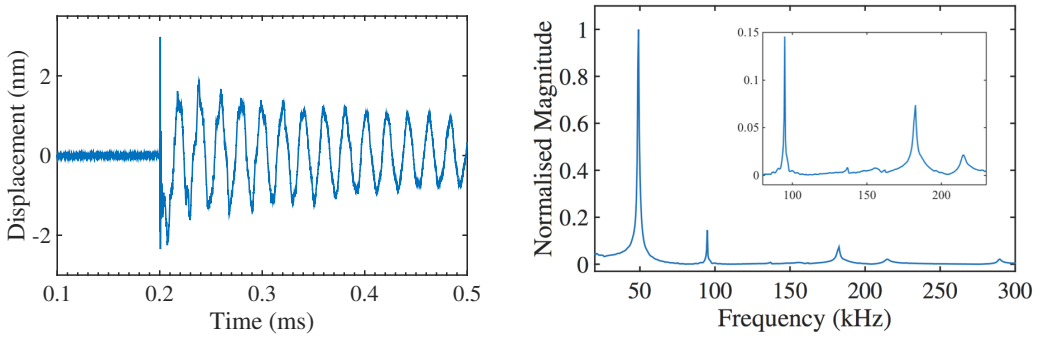

Figure 4.8: (a) Transient displacement of an aluminium cap when actuated by a Nd:YAG laser and (b) the associated normalised frequency spectrum, with an inset showing the smaller peaks in the region 80 kHz to 230 kHz.

The predicted fundamental frequency from equation (3.16) for an edge clamped plate with a radius equal to the inner radius $r = 4.5$ mm of the cap is $f_{0,0}^{a=r} = 62$ kHz, which is roughly 10 kHz higher than the fundamental peak in the frequency spectrum. Similar results were obtained for the higher modes. This is because the clamped boundary condition is not strictly true for the cap. Even though the sides of the cap restricts the motion along the edge there is not an absolute cut-off, which allows the vibration mode shape to extend past the inner radius. As the mode shape extends the spatial wavelength increases, which is associated with a lower frequency. Hence the measured mode frequencies would be expected to be lower than the plate frequencies if the value for the inner radius of the plate is used in the plate model. If the value of the outer radius of the cap is used in the model, the opposite trend is observed, where the predicted plate frequency is lower than then measured frequency. The theoretical fundamental frequency of an edge clamped plate, using the outer radius $R = 5.5$ mm of the cap, is $f_{0,0}^{a=R} = 41$ kHz. Hence it is useful to think of the clamped plate model as providing a frequency band for each mode, within

which the measured modes of a cap will be located.

Exact mode determination requires a full displacement (or velocity) area scan of the radiating face. Because of the narrow width of the theoretical frequency band for the fundamental mode, as well as its position at the lowest part of the frequency spectrum makes it easy to identify, even without seeing the mode shape. This is not true for higher order modes, especially as non-axisymmetric modes that appear close to axisymmetric modes must be considered. The displacement laser scan procedure, as described in §2.2, is time consuming and impractical for evaluating a large number of modes one at the time. A quicker route to determining mode numbering (m, n) of the peaks in a frequency spectrum is to first separate axisymmetric $(m, 0)$ and non-axisymmetric $(m, n \neq 0)$ modes. This can be done by two displacement measurements on the radiating face. The first measurement should be taken as close to the centre of the plate as possible. The second measurement is taken off-centre. Since non-axisymmetric modes have a nodal diameter, there will be no or very little contribution from these modes in the frequency spectrum from the first measurement. These modes are however likely to show up in the frequency spectrum from the displacement signal that was taken off-centre. By comparing the spectra from the two measurements the axisymmetric and non-axisymmetric modes can be distinguished.

The off-centre spectrum can also be compared to the frequency spectrum from a corresponding axisymmetric FE model. Since the model itself is axisymmetric only axisymmetric modes will appear in the model results. This method only works if there is good agreement between the FE model and experiments.

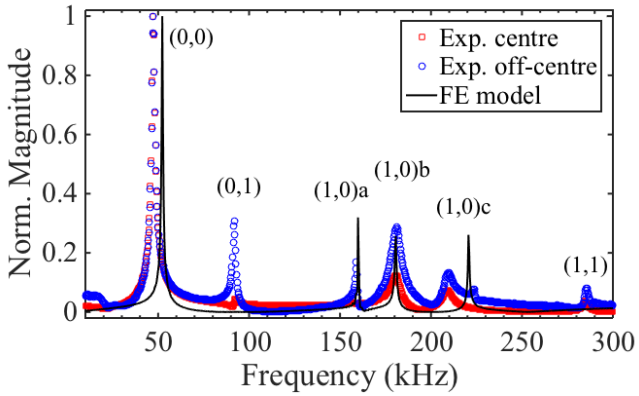

Figure 4.9: Frequency spectra from the front face of the aluminium cap, excited by non-contact methods.

The frequency spectra from a centre displacement measurement, an off-centre measurement and from the FE model are shown in Fig. 4.9. It can be noted that a peak at $\sim$ 100 kHz does not appear in the FE model and is larger in the off-centre measurement compared to the centre measurement, which clearly identifies this as a non-axisymmetric mode. It can therefore be identified as the (0,1) mode, which has a theoretical frequency band 86 kHz$< f <$ 129 kHz. Similarly the (1,1) mode was identified at $f_{1,1} = 285$ kHz. One interesting feature of the spectra that was not immediately apparent in Fig. 4.8b is the three closely spaced peaks [(1,0)a,b,c], which were present in both the simulated and experimental data, but does not emerge from the theoretical model. The lowest frequency peak of the three is in the correct range for the (0,2) mode but the FE model rules this out, since it only shows axisymmetric contributions to the spectrum.

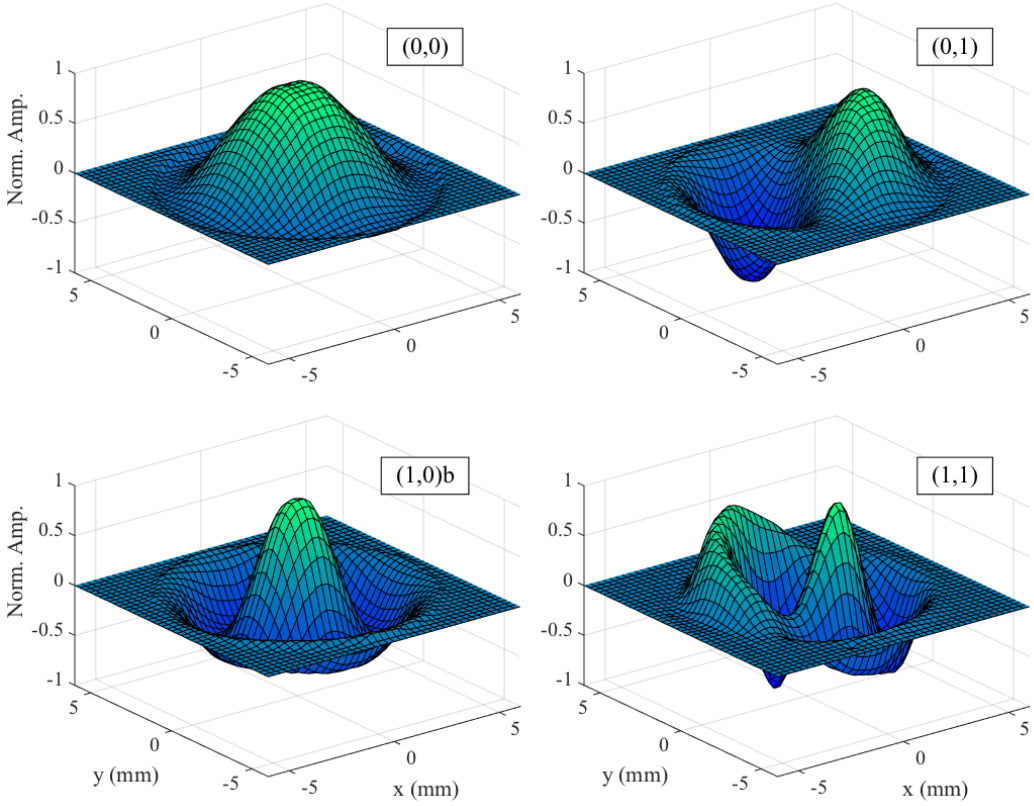

Figure 4.10: Experimental mode shapes from the passive aluminium layer with labeled mode numbers. The mode shapes of (1,0)a and (1,0)c are not shown, but both looked similar to the mode shape of (1,0)b.

The middle peak at $\sim$ 180 kHz, is roughly were the (1,0) mode is expected to occur, from equation (3.16). Hence, these modes are referred to as (1,0)a, (1,0)b and (1,0)c respectively in order of increasing frequency.

As explained in §2.2 the shapes of several modes can be experimentally found from a single area scan of displacement, by using a broadband excitation pulse and then applying a digital, narrowband frequency filter corresponding to the mode of interest. The displacement of the front face of the aluminium cap was measured using the Polytec laser vibrometer as shown in Fig. 2.2. Fig. 4.10 shows the mode shapes of of modes (0,0), (0,1), (1,0)b and (1,1). The correspondence to the theoretical mode shapes that were calculated and shown in Fig. 3.3 is apparent.

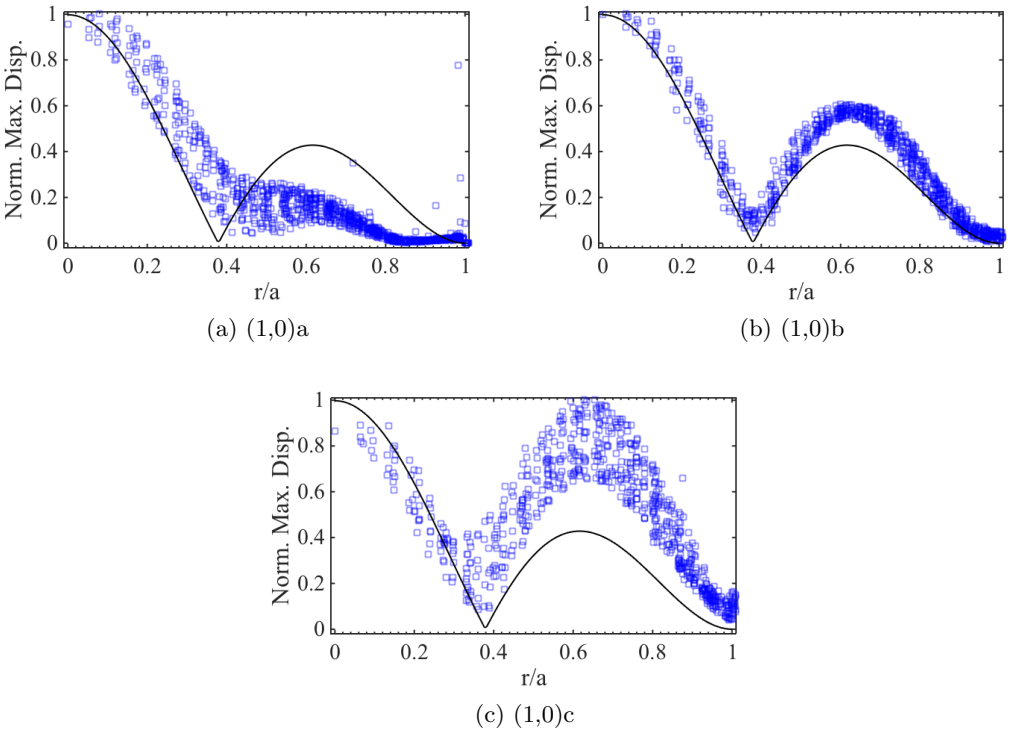

(a) (1,0)a (b) (1,0)b

(c) (1,0)c

Figure 4.11: Experimental, normalised, mode shapes of the split (1,0) mode of the aluminium cap as a function of dimensionless radius (□), compared with the theoretical mode shape (—) calculated for different values of plate radius a, from equation (3.11). (a) mode (1,0)a at 160 kHz with $a = 5.5$ mm, (b) mode (1,0)b at 180 kHz with $a = 5.0$ mm, and (c) mode (1,0)c at 210 kHz with $a = 4.5$ mm.

Fig. 4.11 shows the normalised maximum amplitude of each point of the area scan plotted against the radial distance from the centre of that point for the

split (1,0) mode. The radial distance is taken as r/a, where a represents the plate radius. The value of a has been adjusted for the theoretical mode shapes in the three plots to make the fit to the experimental data better. For (1,0)a $a = 5.5$ mm, which is also equal to the outer radius of the cap. For (1,0)b $a = 5.0$ mm and for (1,0)c $a = 4.5$ mm, the latter of which corresponds to the inner radius of the cap. The relative amplitude of the outer antinode (at a radial distance of approximately 3 mm) to the centre antinode also changes.

The vertical spread of the experimental data for a given value of r indicates how axisymmetric the mode is. If points on the surface with the same radial distance from the centre have different amplitudes than the vertical spread increases. In the limit of a perfectly axisymmetric mode, the spread would be zero along the mode shape. Hence, it is seen that both (1,0)a and (1,0)c are picking up contributions from non-axisymmetric vibrations. Since the FE model is inherently axisymmetric, this could not be observed in the simulated data. A reasonable explanation for this spread comes from the proximity of (1,0)a to the (0,2) mode, and the proximity of (1,0)c to the (0,3) mode, as seen in Table 3.1. Both (0,2) and (0,3) are non-axisymmetric modes, and would therefore have large vertical spreads, as many different amplitudes would be sampled for any given radial distance. Overall the (1,0)b shows the best adherence to the theoretical (1,0) edge clamped plate mode.

4.4.3 Aluminium Cap with $f_{0,0} \simeq 150$ kHz

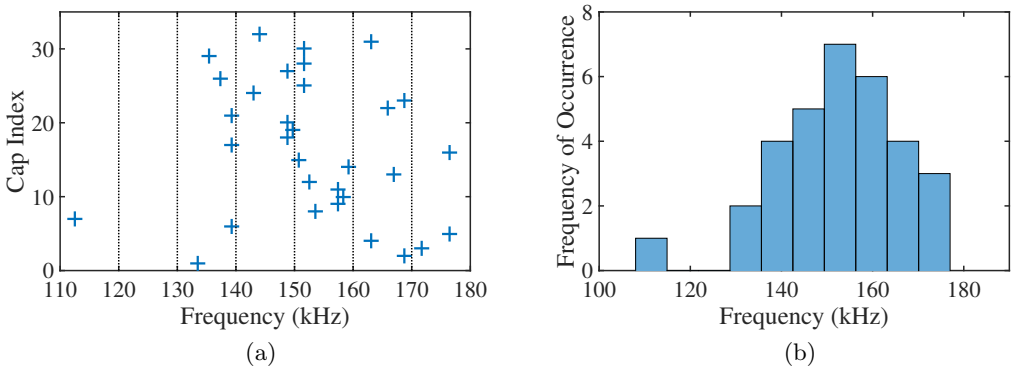

Figure 4.12: (a) Fundamental frequency of 32 individual aluminium caps ($h = 0.5$ mm, $r = 2.5$ mm, $R = 3.5$ mm) without piezoelectric elements, from laser characterisation. (b) Frequency histogram of the fundamental frequency distribution of the caps.

As mentioned previously consistency is both important and difficult to achieve for flexural systems. Fig. 4.12 shows the fundamental frequency of 32 individual aluminium caps with the same nominal dimensions: $h = 0.5$ mm, $r = 2.5$ mm, $R = 3.5$ mm and $L = 4$ mm.

The measured fundamental mode frequency covers a range of about 70 kHz, which is 46% of the average mode frequency. The theoretical frequency band for this transducer was 103 kHz$< f <$ 201 kHz, and though the average mode frequency is within this range, the spread is too large to make any significant comparisons to the theory. If the dimensions of the individual caps had been identical, then the fundamental frequency would have taken a single value within the theoretical frequency band, rather than spreading out between the upper and lower limits. From the histogram, assuming there is no systematic manufacturing error in the machining process, the fundamental frequency associated with the nominal dimensions is within the range 148 kHz to 156 kHz. FE methods confirmed this assumption, and predicted a fundamental mode frequency of $f_{0,0} = 149$ kHz.

As the mode frequency scales with the $\lambda_{m,n}^2$, which increases for higher modes, the absolute value of the frequency shift becomes greater for higher frequency modes. Similarly the theoretical frequency band increases for higher modes. The width of the theoretical frequency band of the fundamental mode of the analysed cap is 98 kHz.

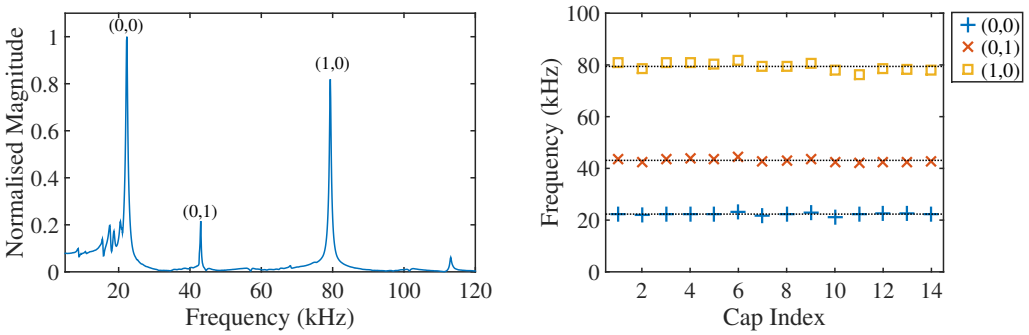

Figure 4.13: (a) Frequency spectrum from a titanium cap ($h = 0.25$ mm, $r = 5.2$ mm, $R = 6.0$ mm) with the first three resonance peaks with labeled mode numbers. (b) Resonance peak positions of the modes (0,0), (0,1) and (1,0) of a set of 14 titanium caps with the same nominal dimensions. Dotted horizontal lines represent the mean frequency values for the respective modes. Spectrum in (a) corresponds to the cap with index number 8 in (b).

4.4.4 Titanium Cap with $f_{0,0} = 22$ kHz

Titanium caps with dimensions $h = 0.25$ mm, $r = 5.2$ mm, $R = 6.0$ mm and $L = 4$ mm were tested. The caps were produced by an external manufacturer. In comparison to the aluminium caps characterised in the previous section, the laser generation and detection characterisation of a set of titanium caps showed good consistency between caps, indicating a low tolerance on the dimensions. Fig. 4.13a shows the frequency spectrum from one cap in a set of 14. Fig. 4.13b plots the frequency of the three first peaks in the spectrum for each cap. The peaks were later confirmed to correspond to modes (0,0), (0,1) and (1,0) in order of increasing frequency.

The mean values and uncertainties are

$$\begin{aligned} f_{0,0} &= (22.3 \pm 0.5) \text{ kHz} \\ f_{0,1} &= (43 \pm 1) \text{ kHz} \\ f_{1,0} &= (79 \pm 2) \text{ kHz}, \end{aligned} \tag{4.9}$$

which fit into the theoretical frequency bands 17.5 kHz< $f_{0,0}$ <23.2 kHz, 36.3 kHz< $f_{0,1}$ <48.3 kHz and 67.9 kHz< $f_{1,0}$ <83.9 kHz respectively.

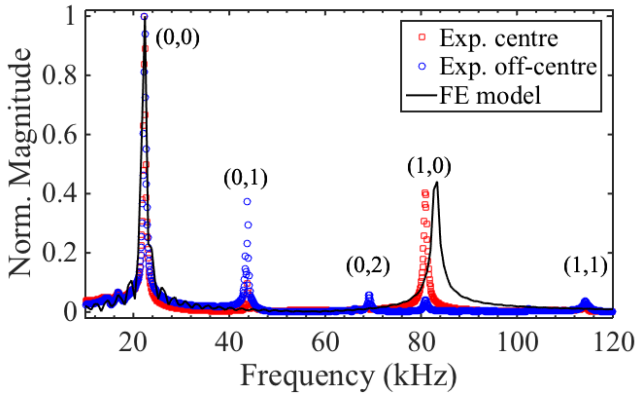

Figure 4.14: Frequency spectra from front face of titanium cap, excited by a Nd:YAG laser.

Similar to the procedure for the aluminium cap, two displacement measurements were made, one close to the centre of the cap and one off-centre. The corresponding frequency spectra and the spectrum from FE methods are shown in Fig. 4.14.

The FE model predicts a slightly higher frequency for the (1,0) mode, but

there is otherwise good agreement between the model and experiment. Again it can be noted that the all non-axisymmetric modes ($m, n \neq 0$) are absent from the results of the FE model, since the model is inherently axisymmetric.

4.4.5 Titanium Flexural Transducer

Piezoelectric flexural transducers were made using titanium caps described in §4.4.4, by attaching a PZT5H piezoelectric disc to the inside of the caps as explained in §4.3. In the first set of titanium transducers, a small disc with dimensions $r_{pzt} = 1.5$ mm and $h_{pzt} = 0.25$ mm was used in order not to impede the flexural motion of the passive layer. Frequency spectra from displacement measurements and from FE simulations are shown in Fig. 4.15.

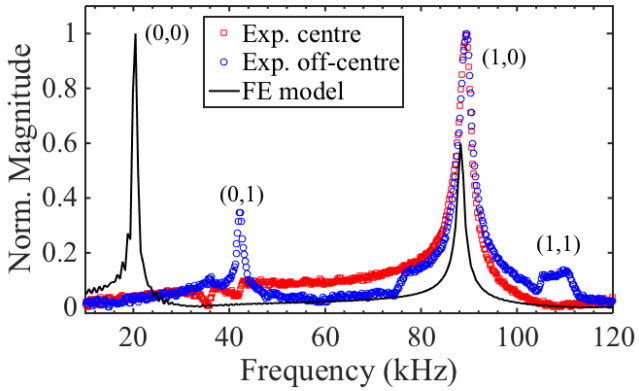

Figure 4.15: Frequency spectra from a titanium flexural transducer excited by a broadband signal.

There are a couple of important features in the spectra that should be highlighted. The fundamental mode is negligibly small in the experimental data, but has the greatest amplitude of the modes in the FE spectrum. This behaviour was not predicted, as generally the fundamental mode was dominant in the results from the caps, as seen in Figs. 4.13a and 4.14, although the (1,0) mode was observed significantly stronger in the commercial ProWave transducer in §4.4.1. Furthermore, so far the FE models have produced results in good agreement with the experimental results. The second thing to notice is that the (1,0) mode has shifted up in frequency by $\sim$ 10 kHz to 90 kHz. This was expected due to an effective stiffening of the plate due to the addition of the piezoelectric disc.

Surface displacement scans of the transducer front face were made to characterise the mode shapes. The transducer was excited with a 3 cycle, 5 Vpp,

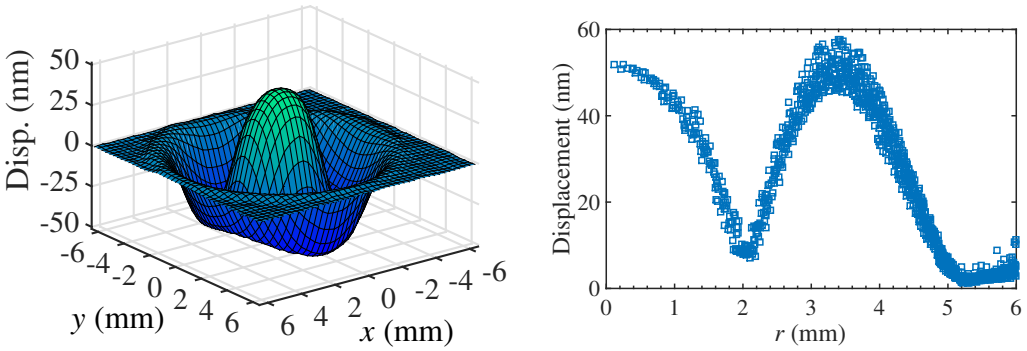

Figure 4.16: Experimental mode shape of mode (1,0) of a titanium transducer with piezoelectric disc dimensions $r_{pzt} = 1.5$ mm and $h_{pzt} = 0.25$ mm. (a) Surface snapshot of displacement at time of maximum centre displacement. (b) Peak-to-peak displacement of each point of the surface scan plotted as a function of the radial distance from the centre of that point.

$f = 89$ kHz sine signal to look at mode (1,0). The results are presented in Fig. 4.16. The mode shape is similar to that of the commercial ProWave transducer (see Fig. 4.7). However, the outer radius of the titanium transducer is under half that of the ProWave transducer, which is why the frequency of the mode is higher. Compared to the mode shape of the (1,0) mode of the passive layer without a piezoelectric element, as seen in Figs. 4.11b and 4.10, the central peak is somewhat flattened, and the amplitude of the outer antinode is greater. These effects are explained by the central stiffening and mass loading of the plate from the piezoelectric disc.

The transducer was also characterised using electrical impedance analysis, as described in §2.3. The impedance of the transducer is shown in Fig. 4.17. The frequency range was extended to 500 kHz, as the transducer exhibited interesting behaviour at higher frequencies. Specifically, there are two large peaks in the phase spectrum at 200 kHz and 320 kHz respectively.

The phase spectrum in Fig. 4.17b is particularly useful for finding the flexural modes. Clearly the peak in the phase at 90 kHz corresponds to the flexural mode (1,0). From later displacement scans the peaks at 200 kHz and 320 kHz were identified as corresponding to modes (2,0) and (3,0) respectively (see Figs. 4.20 and 4.21). Away from resonance the impedance phase $\simeq 90°$, as expected for a piezoelectric system. Similar to the spectrum from displacement data, the fundamental mode has no significant impact on the impedance. Hence, the lack of the fundamental mode from the displacement data was not due to the particular excitation

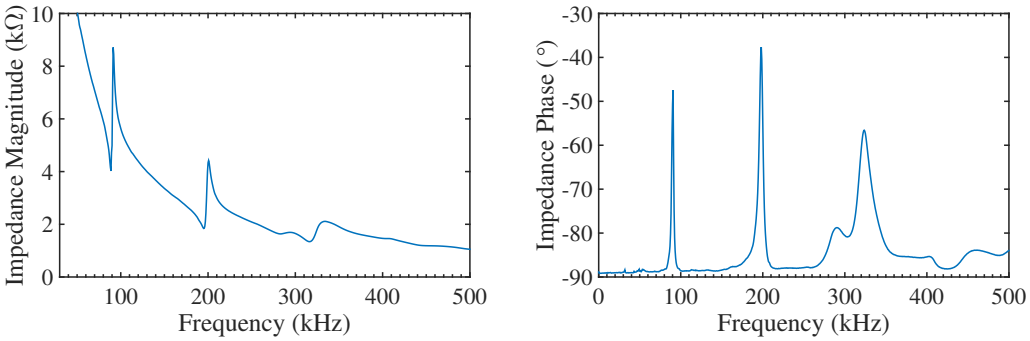

Figure 4.17: Electrical impedance (a) magnitude and (b) phase of a titanium transducer with piezoelectric disc dimensions $r_{pzt} = 1.5$ mm and $h_{pzt} = 0.25$ mm.

method used, which will also affect the prevalence of individual modes. It is seen that axisymmetric modes are favoured in the impedance spectrum.

To check that the disappearance of the fundamental mode was not isolated to one specific transducer, more titanium transducers with the same dimensions were tested using the same methods. Fig. 4.18 shows the frequency spectra from two other transducers. The spectra are in good agreement with each other, as well as with the previous one in Fig. 4.17. They confirmed that the fundamental mode was missing in general for this type of transducer.

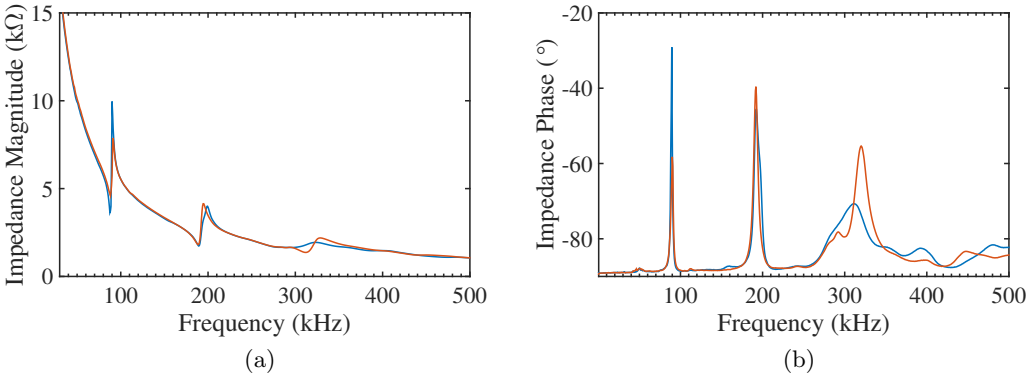

Figure 4.18: Electrical impedance (a) magnitude and (b) phase of two titanium transducers with piezoelectric disc dimensions $r_{pzt} = 1.5$ mm and $h_{pzt} = 0.25$ mm.

The amplitudes of the resonance peaks of the phase spectra differ between the three transducers. It is not just a case of one transducer behaving differently to another. In Fig. 4.18 one transducer has significantly greater phase peak at mode (1,0) around 90 kHz, whereas the amplitudes are comparable for mode (2,0). This behaviour hints at inconsistency in assembly process of the transducers. Even though the construction method described in §4.3 limited the variability between transducers to a great extent, it did not eliminate it. Possible reasons and solutions for this problem are discussed in the conclusions §4.5.

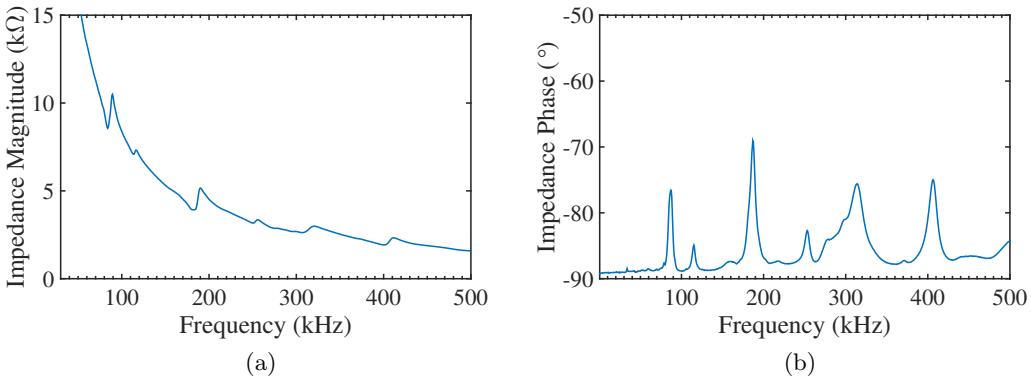

Figure 4.19: Electrical impedance (a) magnitude and (b) phase of a titanium transducer with a slightly off centre piezoelectric disc.

An interesting observation was made in the impedance results from a transducer, which during assembly had its piezoelectric disc slightly displaced (< 1 mm) from the centre. The impedance magnitude and phase are shown in Figs. 4.19a and 4.19b respectively. As seen in the phase spectrum, the axisymmetric modes (1,0), (2,0) and (3,0) have smaller amplitudes, whereas non-axisymmetric modes, such as (1,1) at 115 kHz, have increased amplitudes. By not properly centering the piezoelectric disc, asymmetry is added to the system, which unsurprisingly increases non-axisymmetric behaviour of the transducer.

The experimental mode shapes of modes (2,0) and (3,0) are shown in Figs. 4.20 and 4.21. The scan of mode (2,0) was obtained by exciting the transducer with a 3 cycle, 5 Vpp, 197 kHz sine signal. Mode (3,0) was less prevalent in the displacement data, and exciting the transducer with a short sine burst with frequency $f_{3,0}$ did not produce a clean mode. Instead a superposition of mode (1,0), (2,0) and (3,0) was obtained. Hence the scan data presented in Fig. 4.21 was obtained from exciting the transducer with a 50 cycle, 2 Vpp, 321 kHz sine wave. This is one of the reasons

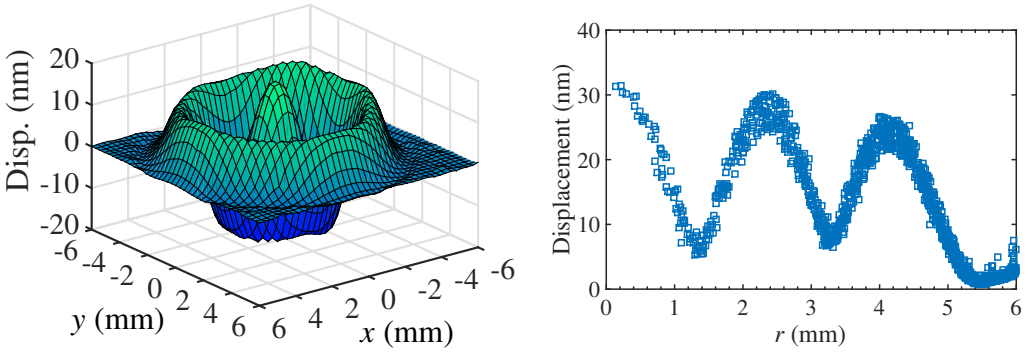

Figure 4.20: Experimental mode shape of mode (2,0) of a titanium transducer with piezoelectric disc dimensions $r_{pzt} = 1.5$ mm and $h_{pzt} = 0.25$ mm. (a) Surface snapshot of displacement at time of maximum centre displacement. (b) Peak-to-peak displacement of each point of the surface scan plotted as a function of the radial distance from the centre of that point.

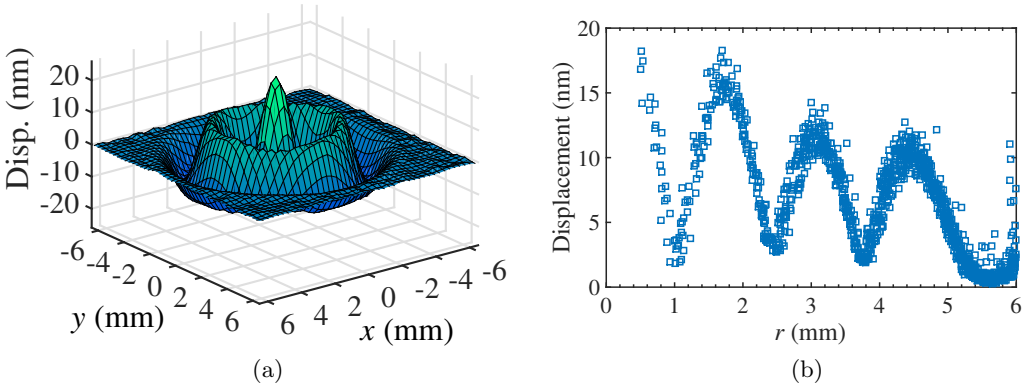

Figure 4.21: Experimental mode shape of mode (3,0) of a titanium transducer with piezoelectric disc dimensions $r_{pzt} = 1.5$ mm and $h_{pzt} = 0.25$ mm. (a) Surface snapshot of displacement at time of maximum centre displacement. (b) Peak-to-peak displacement of each point of the surface scan plotted as a function of the radial distance from the centre of that point.

the mode shape looks more symmetric and more consistent with the associated theoretical clamped plate mode shape.

The effect of the radius of the piezoelectric disc on the transducer performance was investigated using FE methods. A model as was shown in Fig. 3.5 with varying piezoelectric radius r_{pzt} was made. Fig. 4.22 shows how the central displacement amplitude of modes (0,0) and (1,0) of the transducer varies with piezoelectric disc radius.

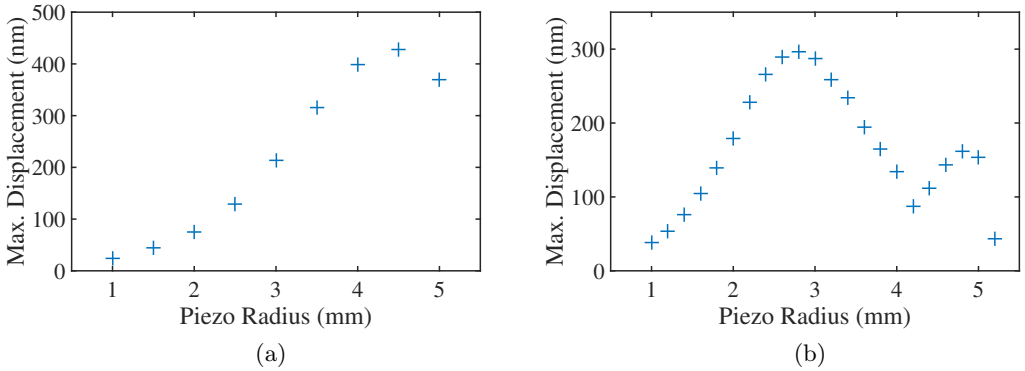

Figure 4.22: Maximum displacement of the centre of the front face of a titanium transducer plotted against the radius of the piezoelectric element from the FE model, for (a) mode (0,0) and (b) mode (1,0).

In general the displacement amplitude increases with increasing radius. This was expected since a larger disc increases the overall amount of active material as well as the capacitance of the device. The effect is however non-linear and depends on both the dimensions of the passive layer and the specific mode shape that is being excited. The amplitude of the fundamental mode increases continuously with increasing radius $r_{pzt} < r$, i.e. until the disc radius equals the inner radius of the cap, where the amplitude drops. The (1,0) mode on the other hand has an increasing amplitude in the region $r_{pzt} < 3$ mm, followed by a drop for 3 mm $< r_{pzt} < 4$ mm. The amplitude then rises again until the disc radius equals the inner radius of the cap where there is a sharp drop. This behaviour is explained by referring back to the specific mode shapes of the (0,0) and (1,0) modes, which reveals that the value of r_{pzt} that produces maximum amplitude of the (1,0) mode coincides with the radial distance to the outer antinode. From the thin plate theory (see §3.1) the position of the outer antinode of mode (1,0) is at $0.61a$, which for the titanium transducer gives $0.61r = 3.2$ mm. This is the largest radius of the piezoelectric disc without the disc having to bend back on itself, which is very energy costly, which explains

why the amplitude drops for larger radii even though the active region increases and the voltage is kept constant. This effect is absent for the (0,0) mode since it has no outer antinode, i.e. the whole front face is in phase. The drop in amplitude that occurs for both modes at $r_{pzt} = r$ occurs because the sides of the cap restrain the lateral motion of the piezoelectric disc, and hence limits the strain exerted on the passive layer to cause flexing.

Since the piezoelectric discs used so far had $r_{pzt} = 1.5$ mm, which has a relatively small amplitude according to the FE results, large improvements could be expected by optimising the radius of the discs used. Because the transducers were made to operate in the (1,0) mode, PZT5H discs with dimensions $r_{pzt} = 3$ mm and $h_{pzt} = 0.25$ mm were used to make a new set of titanium transducers. The impedance of one transducer is shown in Fig. 4.23.

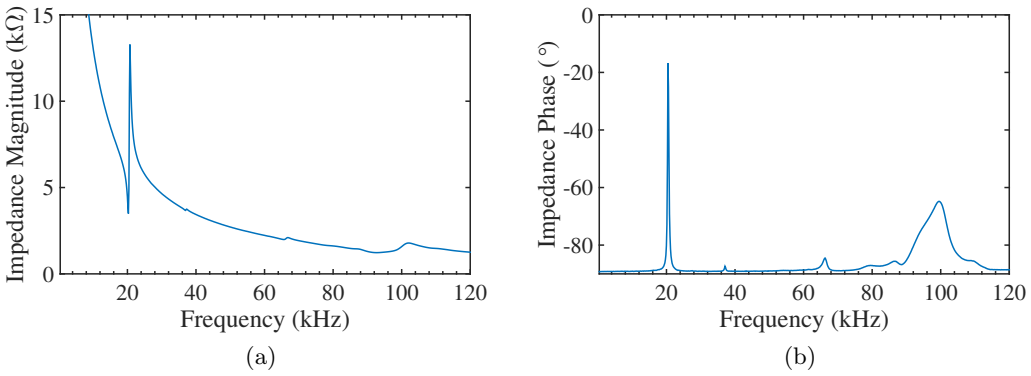

Figure 4.23: Electrical impedance (a) magnitude and (b) phase of a titanium transducer with piezoelectric disc dimensions $r_{pzt} = 3.0$ mm and $h_{pzt} = 0.25$ mm.

The fundamental mode is around 20 kHz and the (1,0) mode has been shifted up further in the spectrum to $f_{1,0} \simeq 100$ kHz. The increased size of the piezoelectric element reduced the phase peaks of higher modes (2,0) and (3,0) significantly, which is why the spectrum range has been limited to 120 kHz.

Fig. 4.24 shows the mode shape of a transducer, that was excited by a 3 cycle, 5 Vpp, 100 kHz sine signal. The mode shape should be compared to that of the previous set of transducers in Fig. 4.16. The overall displacement amplitude has increased by about a factor of two. The increase is not as great as suggested by the FE results, which predicted an increase by a factor of three (from 100 nm to 300 nm as seen in Fig. 4.22b). The centre peak is sharper, because the piezoelectric element extends further inside the cap, and the mode shape looks more like the theoretical

$W_{1,0}(r)$. There is a local spike along the outer antinode, which is seen in both Figs. 4.24a and 4.24b, but the outer antinode is otherwise lower, relative to the central peak.

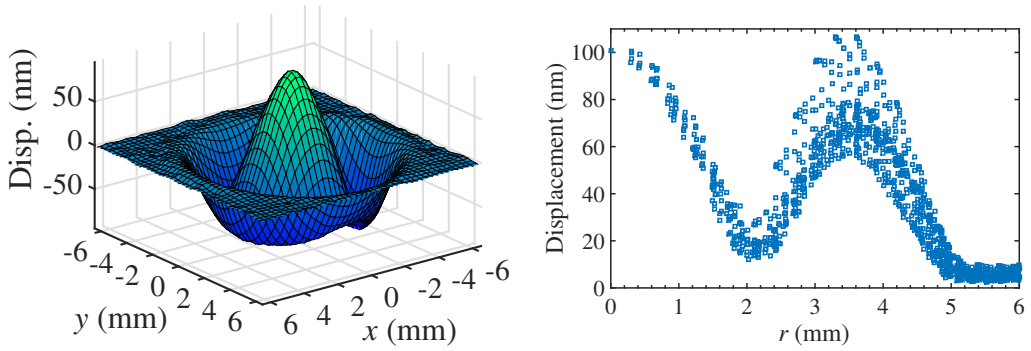

Figure 4.24: Experimental mode shape of mode (1,0) of a titanium transducer with piezoelectric disc dimensions $r_{pzt} = 3.0$ mm and $h_{pzt} = 0.25$ mm. (a) Surface snapshot of displacement at time of maximum centre displacement. (b) Peak-to-peak displacement of each point of the surface scan plotted as a function of the radial distance from the centre of that point.

The pressure output from the transducer was measured with an acoustic microphone (details of setup were given in §2), and is displayed together with the associated frequency spectrum in Fig. 4.25. The transducer was excited by a 3 cycle, 10 Vpp, 100 kHz sine signal. The frequency was chosen because it was close to the (1,0) mode in the transducers, even though each transducer had a slightly different resonance frequency. The microphone was put 24 cm from the transducer front face. The frequency bandwidth FWHM$\simeq$ 15 kHz or 15% of the centre frequency. The bandwidth can be improved by reducing the number of excitation cycles at the cost of pressure amplitude. Inversely, if the bandwidth is of less importance the number of cycles can be increased to get higher pressure levels. Fig. 4.26 shows the pressure output from another titanium transducer from the same set that was excited by a 50 cycle, 10 Vpp, 97 kHz (at resonance) sine signal. The transducer was driven at resonance to see the maximum output when using many cycles.

The pressure amplitude is over 20 Pa or 120 dB sound pressure level (SPL). This is one advantage of using a resonating system, where the amplitude can be controlled not only by the excitation voltage but also by the number of cycles. Being able to keep the voltage low is beneficial to applications concerned with intrinsic safety, such as flow metering.

In essence, an effective 100 kHz titanium flexural transducer has been made.

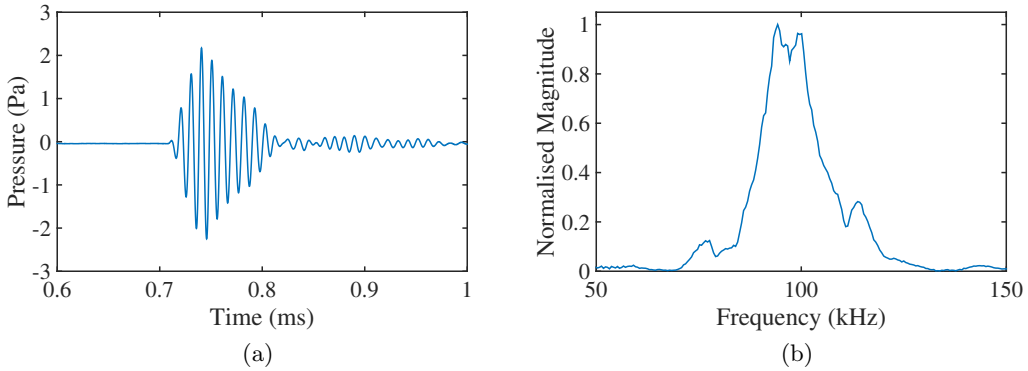

Figure 4.25: (a) Pressure 24 cm from source and (b) associated frequency spectrum, from a titanium transducer excited by a 3 cycle, 10 Vpp, 100 kHz sinusoidal signal

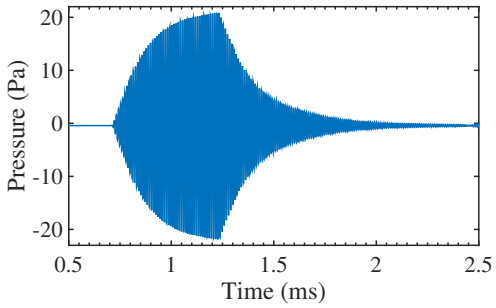

Figure 4.26: Pressure output 24 cm from front face of titanium transducer, excited by a 50 cycle, 10 Vpp, 97 kHz sine signal.

4.4.6 Flexural Phased Array Transducer

The construction method described in §4.3.1 was used to build a first flexural transducer array. Array elements are referred to by element number (p, q), where p is the row and q the column of the element starting from $(0, 0)$ in the upper left corner of the array. Hence, the central element is referred to as element (1,1) in this 3×3 array. To avoid confusion with mode numbering (m, n) it will always be made clear when the number refers to an element or a vibration mode. A condensed report on the flexural array transducer is found in the conference paper [73] (reproduced in Appendix A). The array has a pitch $d = 12.4$ mm, kerf $k = 2$ mm. The layout with

labeled dimensions are shown in Fig. 4.27. The plate used was a $50 \times 50 \times 0.25$ mm stainless steel shim. The piezoelectric elements were the same PZT5H discs used for the titanium transducers in the previous section, with radius $r_{pzt} = 3.0$ mm and thickness $h_{pzt} = 0.25$ mm. Hence, for each individual element, the piezoelectric disc, the inner radius and plate thickness were the same as for the titanium transducers in §4.4.5.

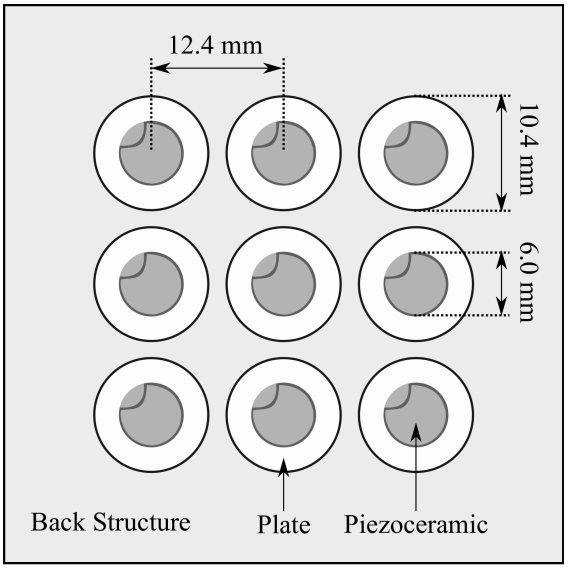

Figure 4.27: Bottom view schematic diagram of flexural array transducer.

The dimensions of the array elements were chosen to produce similar behaviour to the titanium transducers, so that the behaviour and performance of individual elements could readily be compared to the behaviour and performance of single element flexural transducers. If the baffle bonded to the stainless steel plate provides sufficient isolation between array elements, each element should behave like a single element flexural transducer. On the other hand, if there is insufficient isolation the whole plate will vibrate at a much lower frequency, and individual elements will not be well defined. Consequently, if the array works as intended the array elements will use the (1,0) vibration mode, like the flexural titanium transducers. In general it might be better to use the fundamental mode for flexural arrays, since it has a simpler output beam profile.

When the transducer is operated at 100 kHz, which is close to the (1,0) mode frequency of the titanium transducers, the ultrasound wavelength in air is 3.4 mm. Then $d > \lambda/2$, which makes grating lobes unavoidable. The transducer would therefore not be suitable for imaging applications. In general, because of

the relation between frequency and plate radius $f \propto 1/a^2$ from equation (3.16), it is not possible to make a flexural array which passes the $\lambda/2$ criterion. As the element size is reduced to reduce the pitch, the frequency increases and λ becomes smaller. Recent research into a smart aperture waveguide for a different kind of flexural transducer array, in order to achieve pitch $d < \lambda/2$, can be found in the literature [74].

An in-house built low frequency phased array controller was used to drive the transducer. Fig. 4.28a shows the pressure signal 40 cm from the centre element, when excited alone by a 100 kHz, 3 cycle square wave. The excitation voltage amplitude was set to 2% of the maximum output, which is approximately 10 V. The element pressure output measured $\simeq$ 1.1 Pa in amplitude, which is sufficient and suitable for sensor type applications. Fig. 4.28b shows the associated frequency spectrum.

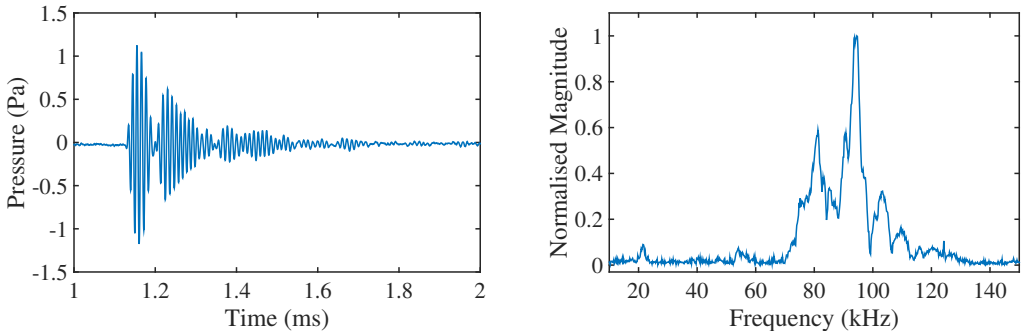

Figure 4.28: (a) Pressure output 40 cm from centre element, excited by a 3 cycle, ∼20 Vpp, 100 kHz square wave. (b) The associated frequency spectrum.

The spectrum gives a first indication that the array element behaves like a flexural transducer with a radius defined by the baffle, i.e. $r = 5.2$ mm. There is significant magnitude between 90 kHz and 100 kHz, which is the region where the (1,0) mode is expected. Also, there is a small low frequency contribution at just above 20 kHz, which is where the fundamental mode is expected to be found. The (1,0) frequency peak is not as clean as those seen in the single element transducers (e.g. in Fig. 4.25), which is due to the more complex structure and interactions with neighbouring array elements.

Fig. 4.29a shows the pressure along the central line 40 cm from the transducer when all transducer elements are used in phase, and Fig. 4.29b plots the

maximum pressure amplitude at the same point in space (on the central line) from each individual element.

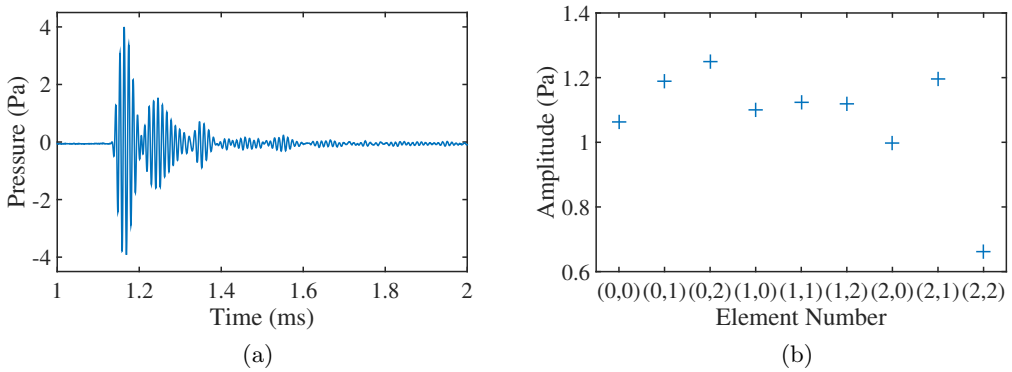

Figure 4.29: (a) Pressure output 40 cm from transducer, when all elements are excited. (b) The maximum pressure amplitude from each individual element.

The pulse shape is similar to that from the centre element in Fig. 4.28a. The amplitude from the transducer array is 4 Pa, which is lower than the sum of the individual element amplitudes, because of the different path lengths and to the measurement point. For constructive interference the central element would have to be delayed with respect to the outer elements by the time corresponding to the difference in path length, in accordance with equation (1.48). From Fig. 4.29b it is seen that the elements have similar output amplitudes, except for element (2,2), which has a significantly lower output.

To confirm that the excited mode around 100 kHz is the (1,0) mode, and to see the extent to which the element is contained within the limits of the baffle, a time resolved displacement scan of the array front face was done. Fig. 4.30 shows the maximum displacement of the array as the central element was excited. The element was excited by a 3 cycle sinusoidal signal at 100 kHz and 5 Vpp.

From the figures it is seen that the displacement is mostly constrained to the area defined by the baffle, and that the vibration mode has one nodal radius indicative of the (1,0) mode shape. When comparing Fig. 4.30b to the results from the single element transducer in Fig. 4.16b, it is seen that the apparent element size of the array element is larger, with a radius approximately 1.5 mm greater. The vertical spread is relatively large close to the edge of the element, which indicates a loss of symmetry in that region. The displacement amplitude of the single element transducer is greater than that of the array element, which is partly explained by

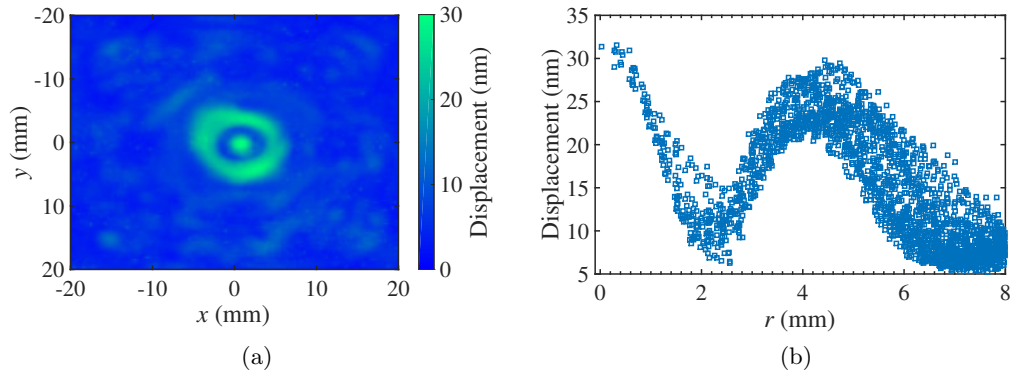

Figure 4.30: Maximum front face displacement of flexural array transducer when the centre element is excited. (a) Surface plot covering all elements and (b) maximum displacement as a function of radial distance from centre focused on the centre elements.

the use of stainless steel in the array instead of titanium. The resonance frequency is also lower for the array element, because of the extended radius of the mode shape, which means that the transducer was driven slightly off-resonance.

The mechanical crosstalk between elements was evaluated by measuring the displacement of neighbouring elements with a laser vibrometer. Significant mechanical cross talk, with displacement amplitudes of neighbouring, inactive elements, reaching -12 dB was observed. Fig. 4.31 shows the transient displacement signals from the centre of three separate elements, when one of them was being excited. The signals are labeled with their respective element numbers.

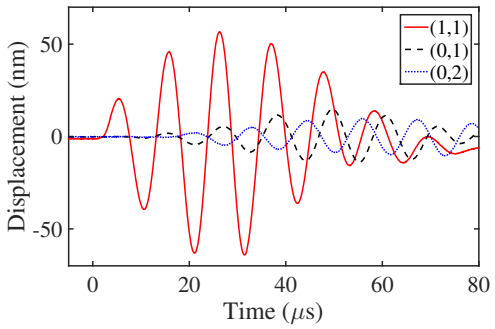

Figure 4.31: Centre displacement signal from three elements, when the centre element (1,1) is excited, showing the level of mechanical crosstalk.

Fig. 4.32 shows the maximum displacement of the array, when all elements are driven in phase with the phased array controller. All elements were excited with

a 3 cycle, 100 kHz, square wave, with 0.5% pulser amplitude The results indicate that there is good consistency between most of the elements. Element (2,2), in the lower right corner, is less well defined than the others, and surrounded by high displacement peaks that are not part of the (1,0) vibration mode. This is due to locally weak bonding between the baffle and the steel plate. The high displacement peaks around this element are associated with areas of visible, trapped air in the bond layer. Hence it can be concluded that bond strength and consistency are important for the performance of the individual elements and of the array as a whole.

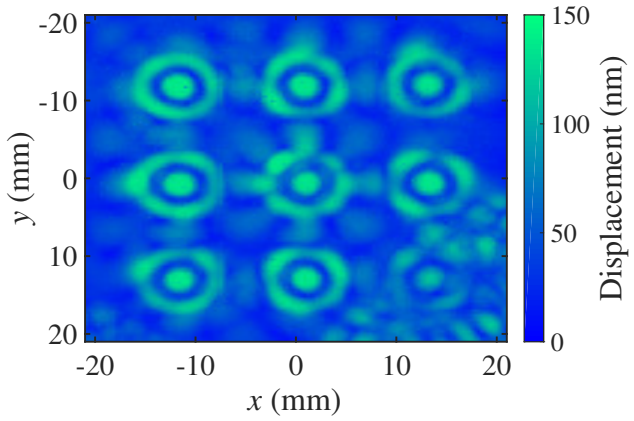

Figure 4.32: Maximum front face displacement of flexural array transducer when all elements are excited in phase.

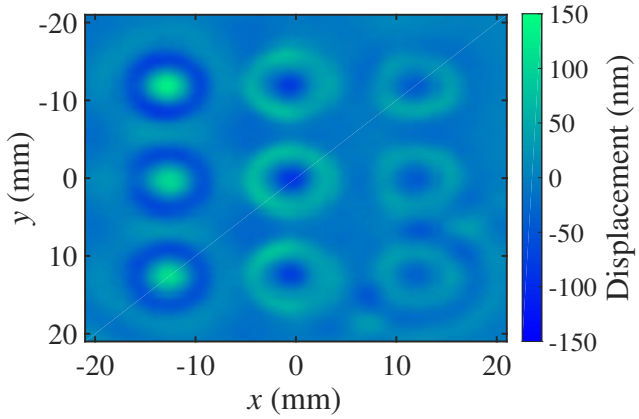

Figure 4.33: Instantaneous front face displacement of the flexural array when phased to produce a 5 degree steering angle.

Some initial steering tests by phasing the array were carried out. Fig. 4.33

shows a snapshot of the array displacement, when the elements were phased to produce 5 degree steering. The maximum pressure amplitude could successfully be shifted off-centre by small angles, but large grating lobes were present. This was expected given the relatively large element spacing, and the small number of array elements.

4.5 Conclusions from Piezoelectric Flexurals

The characterisation of the passive component of the flexural transducer system showed that there is good agreement between the theoretical model for an edge clamped plate and a cap with equivalent dimensions. Since the cap has an inner radius r and outer radius R it was useful to define an upper and lower limit for the frequency of any particular mode. This provided a theoretical frequency band for each mode, within which that mode was expected to appear experimentally. The band increases with increasing mode number and is therefore most useful in predicting low frequency modes. The tolerance on the dimensions of a cap is quite low for producing consistent frequency behaviour.

The aluminium cap investigated in §4.4.2 had a fundamental mode frequency $f_{0,0} = 50$ kHz, which is within the theoretical frequency band 41 kHz$< f_{0,0} <$62 kHz. Two modes at 160 kHz and 210 kHz respectively, as seen in Fig. 4.9, were identified as variations of the (1,0) mode, since they both were mostly axisymmetric and had one nodal radius. From Fig. 4.11 it is seen that mode (1,0)b is in best agreement with the theoretical mode shape. It was theorised that the slight non-axisymmetric contribution to the other two nodes (1,0)a and (1,0)c were due to the vicinity of non-axisymmetric modes (0,2) and (0,3) respectively.

Because of the large frequency discrepancy between the small aluminium caps reported in §4.4.3 they were not used to make transducers. It should also be noted that because of the small radius $r = 2.5$ mm, which was chosen to produce a high frequency fundamental mode, the plate ratio $a/h \sim 6$ puts the cap just outside the range of a thin plate as defined in §3.1. Hence the assumptions that are used to derive the plate equation (3.1) and subsequently equations (3.10) and (3.16) for the mode shapes and mode frequencies respectively, are not valid.

The set of titanium caps investigated in §4.4.4 was shown to have mode frequencies all within the theoretical frequency bands. It is therefore reasonable to use the thin, circular plate with clamped edge model to describe the flexural vibrations of the cap. The consistency and predictability of the cap results were two of the main reasons most of the subsequent transducer development was done using

these caps as the passive layer. Another reason was the frequency of the (1,0) mode $f_{1,0} = 80$ kHz, which is twice that of the commercial ProWave transducer that was analysed in §4.4.1. By using this mode, a flexural transducer sensor with a higher frequency than currently exists could be developed and characterised.

The first set of titanium transducers, using a piezoelectric element with a radius of 1.5 mm, had an operating frequency of 90 kHz corresponding to the (1,0) mode. The displacement of the (2,0) mode is roughly half that of the (1,0) mode for the same input voltage. Though this is significantly less it is quite possible to use this mode for higher frequency applications, where the frequency increase is more important than the loss of power efficiency. Similar arguments could be made for mode (3,0) at 320 kHz, but because this mode was harder to excite, requiring more cycles in the excitation signal, it also puts limits on the time resolution of the signal.

The mode shape of the transducer operating at 90 kHz showed a flattening of the central peak, compared to the theoretical mode shape. Hence, it can be said that the addition of a piezoelectric disc will have an effect on both mode shape and mode frequency. The size of this effect will depend on the relative dimensions of the piezoelectric disc to the dimensions of the plate. The commercial ProWave transducer showed less effect from the piezoelectric element, because the passive layer had significantly greater radius and thickness.

FE methods revealed that the optimal radius of the piezoelectric element for the titanium transducer using the (1,0) mode for transduction was ~ 3 mm. A second set with these larger piezoelectric discs was made. The set showed an increased displacement amplitude and a large pressure output. Since the flexural transducer is a resonant system, the output pressure can be increased by increasing the number of cycles in the excitation signal, until the rate of energy loss equals the input and a continuous wave (CW) pressure signal is obtained.

The individual variance between nominally identical transducers is a result of the assembly process and especially of the bonding of the piezoelectric element. As was previously noted, the mode frequencies are sensitive to the dimensions of the passive layer, and the piezoelectric disc can be thought of as changing the effective thickness and stiffness of the cap. Hence, the thickness of the bond layer, which is difficult to precisely control and check, becomes important for consistent transducer behaviour. More work could also be done on the bonding material itself.

The narrow bandwidth combined with the fine dependence upon dimensions and manufacturing makes piezoelectric flexural transducers difficult to match, which makes them more suited to pulse-echo applications rather than transmit-receive.

A new type of flexural ultrasound array was presented in §4.4.6. By using a

single plate of metal, with individual flexural elements specified by a baffle bonded to the pack of the plate, a robust easy to manufacture transducer array was made. Each element behaved similar to a single element transducer with a thickness h equal to the thickness of the plate, and an inner radius r slightly larger than the radius of the holes in the baffle. This was the important proof of concept. Most array elements showed good consistency except for element (2,2), which can be seen in Figs. 4.29b and 4.32. The reason was discovered to be regions of debonding and air inclusions in the bond layer around element (2,2). Using phasing to steer the ultrasound beam by small angles was demonstrated, but for good results more elements and smaller elements are needed.

Chapter 5

Electrodynamic Flexural Transducers

A current carrying coil, for actuating the passive metal layer of a flexural transducer, was first used as an alternative non-contact method for characterising the cap before introducing the piezoelectric element and assembling the transducer. Because the coil does not touch (load) the plate, similar results to those from laser generation (§2.1) were expected. However, displacements much greater than those produced by the pulsed Nd:YAG laser beam source were observed, and so came the idea of building an electrodynamic flexural transducer (EDFT). In essence the EDFT uses the flexural vibration modes of a thin plate for coupling to air, or other low impedance media, combined with non-contact, electromagnetic generation. Apart from the novelty of the EDFT itself there are several other reasons for exploring such a device:

1. Since no piezoelectric materials are used the transducer has potential applications at elevated temperatures above the Curie temperature (T_C) of piezoelectric materials.

2. The design with the metal front makes the transducer more robust than alternative PZT-free designs, such as the electrostatic transducers described in §1.2.4.

3. The easily reconfigurable shape of the generation coil makes new design geometries of the transducers possible.

Fig. 5.1 shows a schematic diagram of the first EDFT design that was tested. In essence, the same type of aluminium cap was used as with the piezoelectric flexural

transducers (§4.4.2), but with the piezoceramic disc replaced by a spiral coil as the active element. Some initial results on mode frequencies and shapes with comparison to FE are presented in the conference paper [75] (reproduced in Appendix A). In this first paper, only generation of ultrasound waves was reported, as attempts to use the EDFT as a detector had failed. Further development has since produced new improved designs of EDFTs both for generation and reception of ultrasound waves[76].

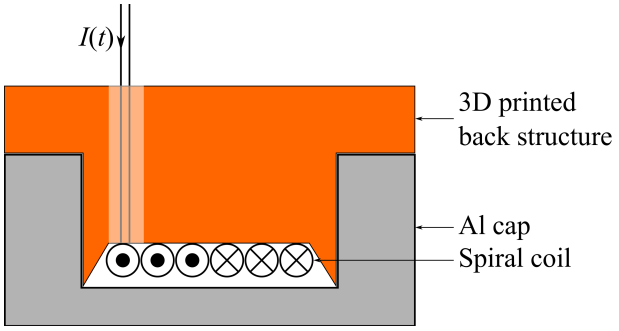

Figure 5.1: Schematic diagram of a crossection of an early EDFT design.

Although EDFTs are a new type of transducer, the electromagnetic coupling of ultrasound into a conductive sample is a well known procedure in the NDE community. It is hence that in the following section, when discussing the electromagnetic principles, references will be made to research on electromagnetic acoustic transducers (EMATs)[77, 78] as well as general eddy current technology[79].

5.1 Electromagnetic Coupling

This section outlines the underlying electromagnetic interactions of the EDFT that couple the electromagnetic energy to mechanical vibrations in the front face of the transducer. The fundamental equations describing electromagnetic behaviour are Maxwell's equations[80], which expressed in differential form are

$$\nabla \cdot \boldsymbol{E} = \rho_e \epsilon \tag{5.1}$$

$$\nabla \cdot \boldsymbol{B} = 0 \tag{5.2}$$

$$\nabla \times \boldsymbol{E} = -\frac{\partial \boldsymbol{B}}{\partial t} \tag{5.3}$$

$$\nabla \times \boldsymbol{B} = \mu \boldsymbol{J} + \mu \rho_e \frac{\partial \boldsymbol{E}}{\partial t}, \tag{5.4}$$

where $\boldsymbol{E}$ and $\boldsymbol{B}$ are the electric and magnetic fields respectively, ρ_e is the (free) electric charge density, ϵ is the electric permittivity ($\epsilon = \epsilon_r\epsilon_0$), μ is the magnetic permeability ($\mu = \mu_r\mu_0$), and $\boldsymbol{J}$ is the (free) current density. When analysing electric and magnetic fields in a sample it is useful to introduce the electric displacement $\boldsymbol{D}$ and magnetic field strength $\boldsymbol{H}$, which are given by the constitutive relations

$$\boldsymbol{D} = \epsilon\boldsymbol{E} \tag{5.5}$$

$$\boldsymbol{H} = \frac{\boldsymbol{B}}{\mu}. \tag{5.6}$$

Using the constitutive relations equations (5.1) and (5.4) can be written as

$$\nabla \cdot \boldsymbol{D} = \rho_e \tag{5.7}$$

$$\nabla \times \boldsymbol{H} = \boldsymbol{J} + \frac{\partial \boldsymbol{D}}{\partial t}, \tag{5.8}$$

which together with equations (5.2) and (5.3) are referred to as Maxwell's equations in a material.

The time varying current in the transducer coil induces a magnetic field, which penetrates into the plate, and in turn induces an electric field in the plate in accordance with Faraday's law expressed in equation (5.3). The electric field induces an eddy current J_E, by accelerating the free electrons in the plate[79, 81, 82]. The current density due to the electric field in a sample with conductance σ is given by Ohm's law[6]

$$\boldsymbol{J} = \sigma\boldsymbol{E}. \tag{5.9}$$

It should be noted that the electric field exerts forces on both positive and negative charges in the plate, but the ions are heavier, restrained in space by lattice bonds, and shielded by electrons, and will therefore not contribute to the current.

The eddy current in the plate is in such a direction that it induces a magnetic field that opposes the original field that caused the current, in accordance with Lenz's law[6]. This limits the penetration depth of the electromagnetic fields into the plate. The depth of penetration is described by the electromagnetic skin-depth δ[83]

$$\delta = \sqrt{\frac{2}{\mu\omega\sigma}}, \tag{5.10}$$

which is the depth at which the field strength drops to $1/e$ of its original value. The higher the frequency of the coil current the smaller the penetration depth. The electromagnetic skin-depth of aluminium at 50 kHz is 0.37 mm, which is similar to

the plate thickness h used in flexural transducers. The electric field in the plate can be expressed as a plane wave, which decays with depth with decay constant δ[80]

$$\boldsymbol{E} = \boldsymbol{E}_0 e^{i(\omega t - \frac{z}{\delta})} e^{-\frac{z}{\delta}}. \tag{5.11}$$

This gives an expression for the current density by using equation (5.9)

$$\boldsymbol{J} = \boldsymbol{J}_0 e^{i(\omega t - \frac{z}{\delta})} e^{-\frac{z}{\delta}}, \tag{5.12}$$

where $\boldsymbol{J}_0 = \sigma \boldsymbol{E}_0$. From equation (5.12) it is seen how both the amplitude and the phase of the eddy current changes with depth. It is common practice in NDT and other applications to assume that the sample width is greater than the skin-depth, in which case the eddy current can be approximated by a single current at the surface with a phase lag of $\pi/4$. However, for the thin plates and low frequencies considered for EDFTs this is not a valid approximation. For a very thin plate or very low frequency, such that $\delta >> h$, the phase of the eddy current does not change significantly throughout the plate and can be assumed constant. However, the EDFTs considered in this work have $\delta \approx h$, which means the problem has to be treated in full without simplifications[84]. Fig. 5.2 shows how the eddy current amplitude and phase change throughout the depth of a 0.5 mm thick aluminium plate.

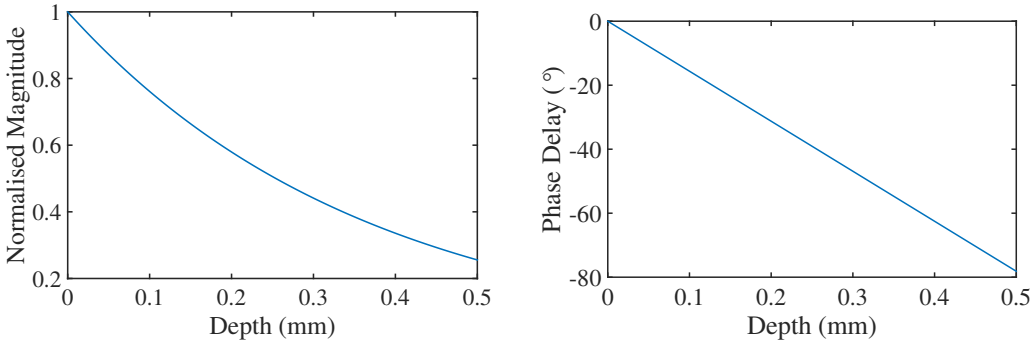

Figure 5.2: (a) Normalised magnitude and (b) phase delay of an eddy current $\boldsymbol{J}$ at frequency $f = 50$ kHz, as a function of depth in an aluminium sample.

The lift-off, i.e. the distance between the coil and the conductive sample, affects the generation current as the equivalent inductance of the system changes[85]. This in turn affects the amplitude and frequency of the eddy current, and subse-

quently of the ultrasonic waves in the plate. In general both the amplitude and frequency of the eddy current J_E decrease with increased lift-off. The shape of the coil, the size and the number of turns determine how sensitive the system is to changes in lift-off.

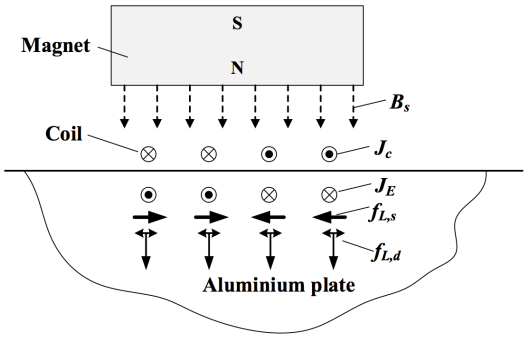

Figure 5.3: Working mechanism of an EMAT on an aluminium sample. $f_{L,d}$ is the Lorentz force due to the dynamic magnetic field and $f_{L,s}$ the Lorentz force from the static magnetic field.

The force on the eddy current from the magnetic fields is the Lorentz force[80]

$$\boldsymbol{F} = q\boldsymbol{E} + \boldsymbol{J} \times \boldsymbol{B}. \tag{5.13}$$

In EMAT's and EDFTs alike the electric field E can be ignored. The magnetic field B can be divided into a static field term B_s from a permanent magnet and dynamic field term B_d induced by the current in the generation coil:

$$\boldsymbol{B} = \boldsymbol{B}_s + \boldsymbol{B}_d. \tag{5.14}$$

Generally speaking, three mechanisms are responsible for the electro-acoustic transduction of EMATs: the Lorentz force, the magnetostrictive force and the magnetization force[86]. The electrodynamic coupling to the front face of the EDFT is via the Lorentz mechanism in this case, as is often the dominant coupling mechanism with EMATs. The generation process of an EMAT on an aluminium plate is illustrated in Figure 5.3. When an alternating current J_c travels through the coil, a dynamic magnetic field B_d is generated in the electromagnetic skin depth of the aluminium plate. The time varying magnetic field induces an eddy current J_E within the skin depth of the plate, and the electrons that constitute this eddy current experience Lorentz forces $f_{L,d}$ and $f_{L,s}$, when the eddy current J_E interacts with the dynamic magnetic field B_d from the EMAT coil and the static magnetic field B_s from the magnet. The directions of these forces are shown in Figure 5.3. The electrons that

experience these Lorentz forces scatter off the atoms, exchanging momentum with the atoms. This in turn gives rise to the coherent motion of the aluminium atoms, leading to the generation of an ultrasonic wave. The resultant wave modes are determined by the configurations and the parameters of the EMAT and the dimensions and the material properties of the plate.

In the detection process, when the atoms and free electrons in the metal move due to the displacement associated with an ultrasonic wave, the free electrons with energy above the Fermi level will experience a Lorentz force in the presence of a magnetic field. These electrons constitute a current that will generate a magnetic field, which when within the electromagnetic skin depth of the surface will produce a magnetic field external to the sample that can induce an electromotive force (voltage) on a suitably orientated detection coil[87]. This makes an EMAT, that operates as a detector, a velocity sensor rather than a displacement sensor[88].

5.2 Design

From the theoretical analysis of electromagnetic coupling in the previous section some design optimisations can be made. The coil lift-off from the metal cap should be minimised, in order to maximise energy transfer. A static magnetic field can be used to enhance the dynamic field, as well as enable the transducer to receive incoming ultrasonic waves. The direction of the static field is also important. It is seen from equation (5.13) and Fig. 5.3 that in order to generate a transverse (out of plane) Lorentz force from the static magnetic field, the field needs to have an in-plane component at an angle to the mirror current. The maximum transverse force on the plate is achieved when the static magnetic field is in-plane and perpendicular to the eddy current. Since the eddy current mirrors the generation current from a spiral coil, the static field should ideally be radial in the plane of the eddy current.

Because of the freedom of coil design[89] the possibility of alternative transducer geometries other than the circular cap can be explored. Specifically, an annular plate, with an inner clamped boundary was considered. It is straightforward to make a spiral coil with a hole at the centre, and by introducing a second boundary there is more freedom in choosing aperture size, for a given resonance frequency. In order to predict mode shapes and frequencies for an annular geometry the higher order Bessel terms from solving the plate equations (3.8) and (3.9) have to be included, which makes the expression more complicated, but still numerically solvable with the two additional boundary conditions for the inner clamped edge. Using Matlab to find the frequency roots of the clamped-clamped annular plate, the dimensions

for the inner and outer boundary radii were chosen to give a fundamental mode frequency of 50 kHz. The frequency was chosen to match the fundamental mode frequency of the original aluminium cap, which was used to make the first EDFT. Also, the attenuation for ultrasound waves with a frequency of 50 kHz is suitably low for the transmission distances considered.

The three final designs, including the original aluminium cap EDFT, that were investigated are shown schematically in Fig. 5.4. The transducers will henceforth be referred to as transducer A, B, and C respectively. Transducer A is a small aperture circular cap EDFT, transducer B has an annular aluminium cap with a ring magnet inside, and transducer C has a circular aluminium plate with a ring magnet bonded to edges and a mild steel core forming an annular region. The three transducer designs were first presented and compared in [90].

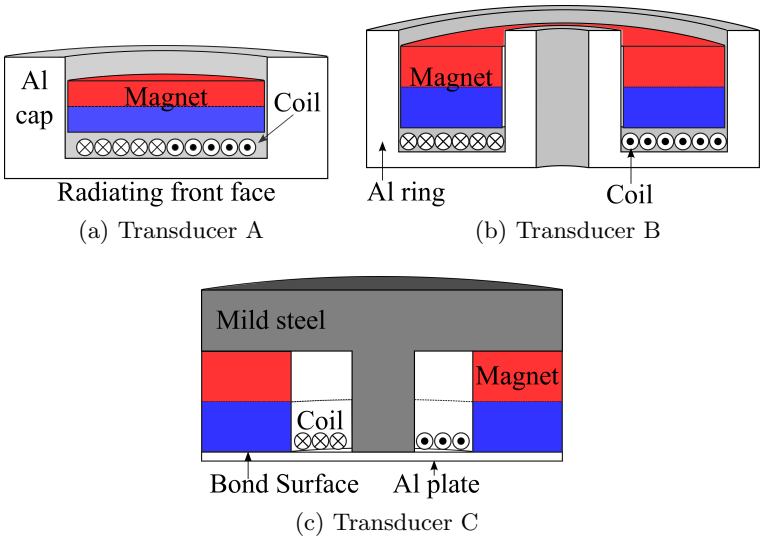

(a) Transducer A

(b) Transducer B

(c) Transducer C

Figure 5.4: Schematic diagrams (not to scale) of the three EDFT designs investigated. The transducers are referred to in the text as (a) transducer A, (b) transducer B and (c) transducer C respectively.

Transducer B has the same plate thickness $h = 0.5$ mm as transducer A. For a circular flexural transducer, increasing the aperture size for a fixed plate thickness would decrease the mode frequencies in accordance with equation (3.16). However, an annular cap has, by virtue of its geometry, a clamped inner radius which can also be varied to influence the mode frequencies. Hence, transducer B was made to have a significantly larger active, radiating, area than transducer A, but with the same fundamental mode frequency $f_{0,0} = 50$ kHz. Increasing the active area both

increases the generation force because of the larger area covered by the generation coil, and increases the output pressure which comes from the integral of displacement across the radiating face as shown in equation (1.28).

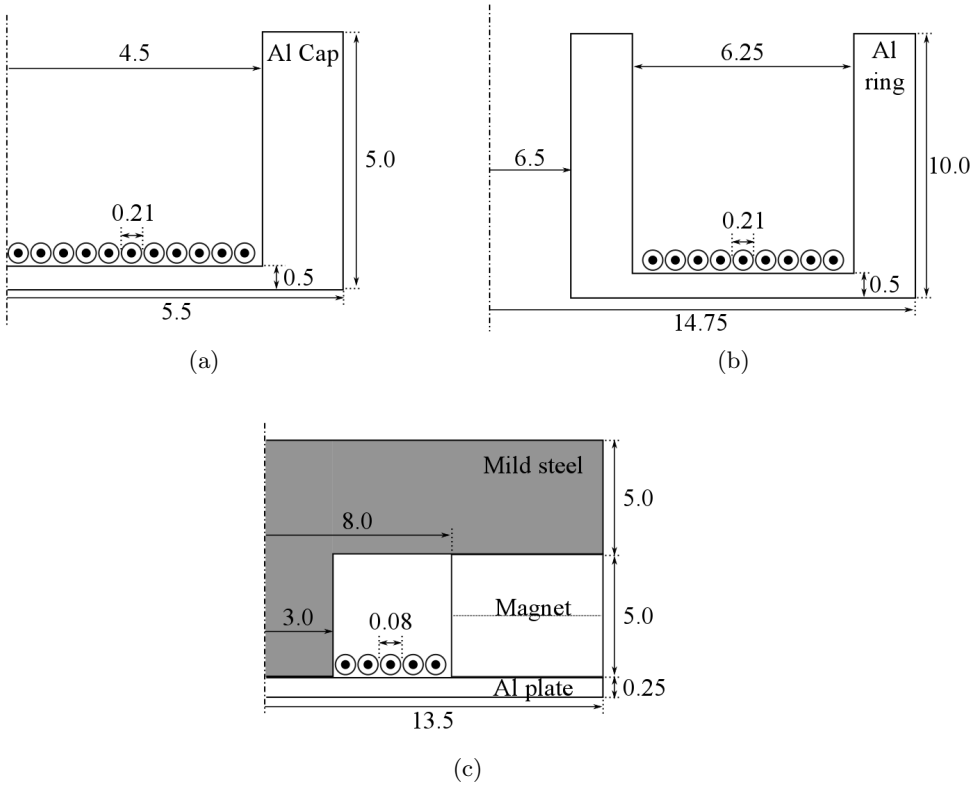

Figure 5.5: Axisymmetric schematic diagrams of (a) transducer A, (b) transducer B and (c) transducer C, with all dimensions in mm.

Fig. 5.5 shows axisymmetric diagrams of the three designs with all dimensions in mm. The active area, defined as the area of the transducer covered by the generation coil, for transducers A, B and C are 63.6 mm^2, 436.9 mm^2 and 172.8 mm^2 respectively.

Transducer C was developed with the problem of receiving ultrasound in mind. Transducer A and B, only use the fringe field of the magnets to sense incoming waves. Transducer C, on the other hand, has the magnet placed such that a greater component of the field lies in the plane of the front face, and the mild steel core works to further direct the field into this plane. To improve the receive sensitivity further, a thin 0.08 mm wire was chosen for the spiral coil. For a given magnetic field the induced current in the coil is directly proportional to the number of turns

in the coil. A thinner wire allows for a greater number of turns in a fixed area, which hence increases the sensitivity of the transducer.

A downside of the design of transducer C is the introduction of a new bond layer, which to some extent suffers from the same problems as the bond layer in the conventional piezoelectric flexural transducers. Also because the magnet is now a part of the housing of the transducer it cannot easily be replaced by an electromagnet for truly high temperature applications. Another potential issue with transducer C is that once it has been sealed with the steel core, the coil becomes inaccessible. Should the transducer break it cannot easily be repaired.

5.3 Construction

Transducers A and B were made with caps machined by the Physics Department's mechanical workshop from aluminium rods. The mild steel core in transducer C was similarly fashioned. The circular aluminium plate at the front of transducer C was laser cut from a 0.25 mm aluminium sheet. The laser cutter was used because it reduces the risk of bending or denting the plate, rather than a need for high precision.

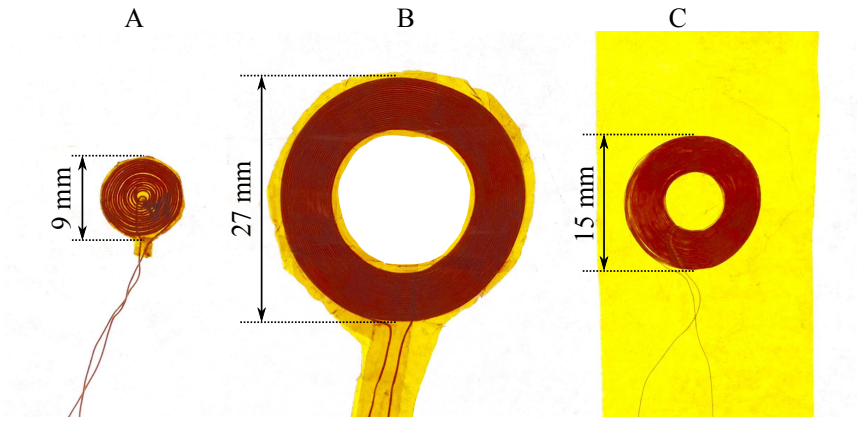

Figure 5.6: Backlit photo of the transducer coils used in EDFTs A, B and C.

The spiral coils were wound by hand with 0.3 mm wire for transducers A and B, and 0.08 mm wire for transducer C, using a 3D printed guide plate, and enclosed in a single layer of Kapton tape. The Kapton tape helped to hold the wire in place, but was not otherwise necessary, and was later removed from the coil in transducer C. The guide plate fixed the outer diameter of the spiral coil. The tape thickness is small, ~ 0.1 mm, and no effect of the increased lift-off was apparent from measurement of the transducer output. Fig. 5.6 shows a photo of the

three different spiral coils used in the three different designs. The photo also gives an indication of the difference in area of the transducer plates that is actuated in the different designs. Two component epoxy Araldite 2014 was used to bond the aluminium plate to the magnet and the steel core in transducer C.

5.4 Results from EDFTs

An in-house built EMAT pulser was used to drive the EDFTs. The pulser has a high voltage low impedance output, optimised for driving the type of coils used in EMATs. The current through a small 100 mΩ resistor in series with the spiral coil used in transducer A is shown in Fig. 5.7a. The frequency content of the current pulse is shown in Fig. 5.7b. The current is roughly U-shaped with a peak-to-peak amplitude of ∼200 A. Pulsers with greater current amplitudes over 1 kA have been used for EMAT applications[91], which suggests that if necessary the EDFTs could be driven with a larger current to produce higher pressure amplitudes. However, a large excitation current puts higher demand on the coil and requires a greater wire thickness to be used. From the frequency spectrum it is seen that though the pulser is not optimised for low frequencies, around 50 kHz, there is still a significant amount of energy in this part of the spectrum.

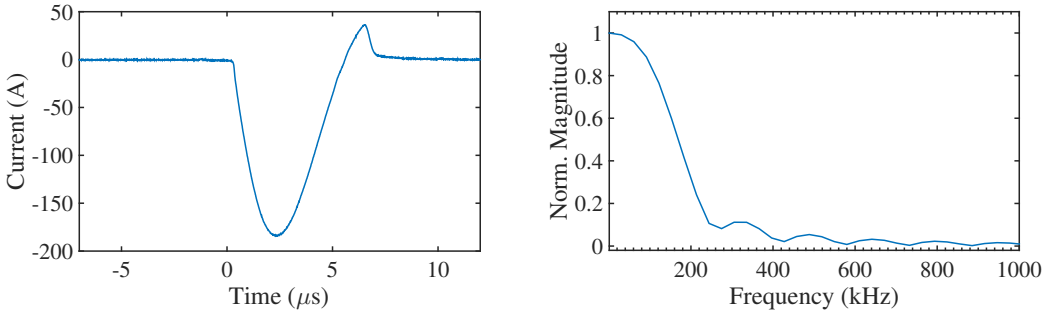

Figure 5.7: (a) Generation current pulse through a 100 mΩ resistor in series with the spiral coil in transducer A and (b) the associated frequency spectrum.

Large pressure amplitudes were observed ∼ 31 cm and ∼40 cm from the front face of the transducers, as seen in Fig. 5.8. Transducer B (Fig. 5.8c) produced the greatest peak pressure amplitudes around 45 Pa or SPL = 127 dB[1]. This is about an order of magnitude greater than the pressure amplitudes from the other two

[1]Using a reference pressure of 20 μPa.

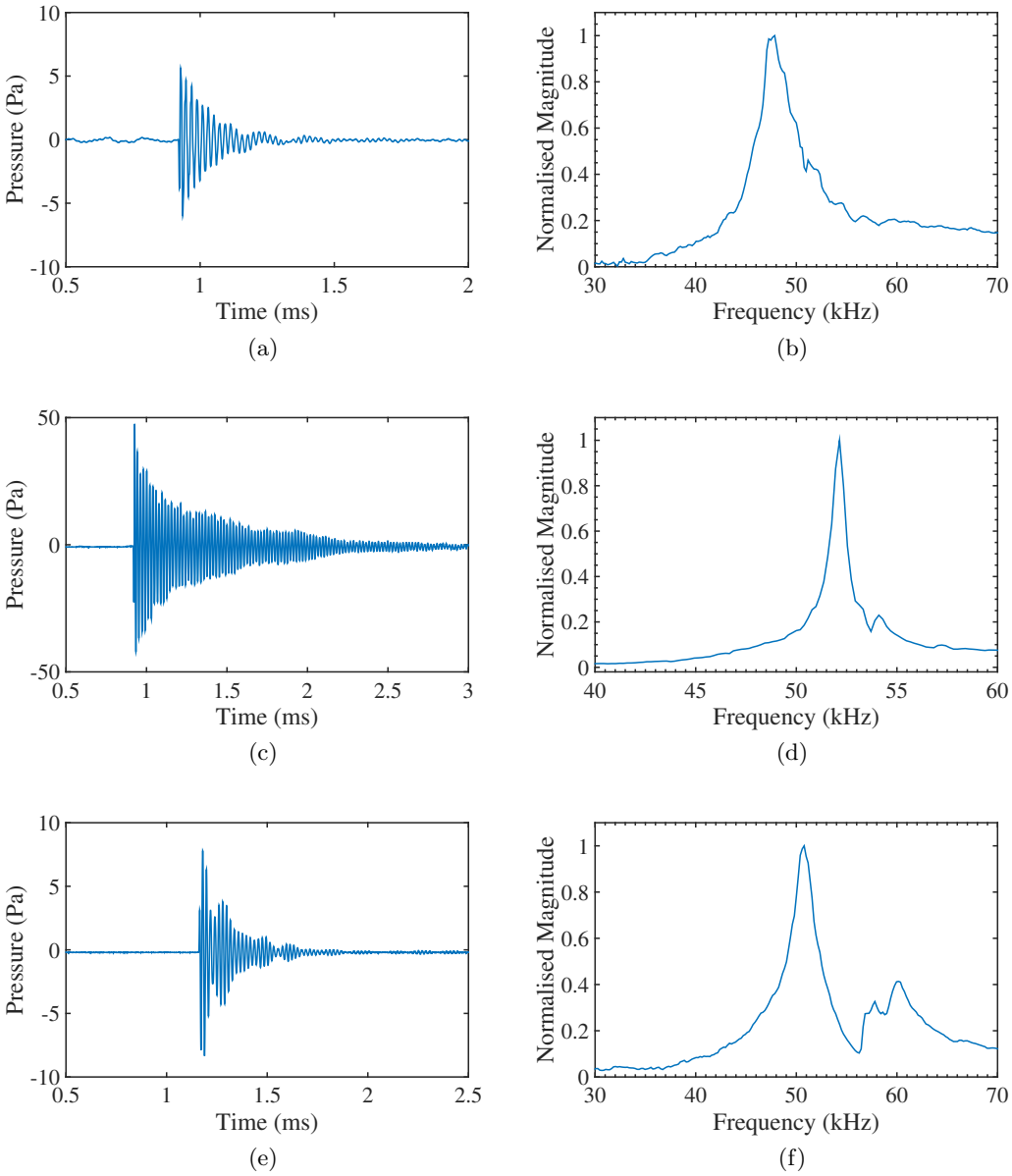

Figure 5.8: Pressure signals from (a) transducer A, (c) transducer B and (e) transducer C, measured with a broadband acoustic microphone. Transducers A and B were located $\sim$ 31 cm from the microphone, and transducer C was located $\sim$ 40 cm from the microphone. The associated normalised frequency spectrum of each signal is shown in (b), (d) and (f) respectively.

designs, which is largely due to the overall greater surface area of the front face of transducer B. However, it is important to remember that the aperture of transducer A cannot simply be increased, as this would reduce the resonance frequency. Hence, by using the annular geometry greater flexibility in frequency and aperture size is achieved, as the inner and outer radius can be varied separately to give a specific resonance frequency. Transducer A (Fig. 5.8a) had a peak pressure amplitude of 5.6 Pa (SPL=109 dB) and transducer C (Fig. 5.8e) a peak pressure amplitude of 7.8 Pa (SPL=112 dB). These pressure amplitudes are sufficiently high for sensor type applications, and especially transducer B has an SPL high enough for NDT applications.

The frequency spectra of the pressure signals are also shown in Fig. 5.8. Similar to the piezoelectric flexural transducers the frequency bandwidths of the EDFTs are small, due to the inherent resonance of the transducers. Transducer B has a particularly long ring down ∼1 ms, which gives it a narrow bandwidth with FWHM=2 kHz (Fig. 5.8d). The centre frequency is also slightly higher than the predicted 50 kHz at 52 kHz. Transducer A (Fig. 5.8b) and C (Fig. 5.8f) both have shorter ring down times ∼0.5 ms, and subsequently broader bandwidths with FWHM=5 kHz. In general these transducers, like the piezoelectric flexural transducers, are not suitable for applications requiring a large range of frequencies to be generated, but would be used in, for example, single mode excitations.

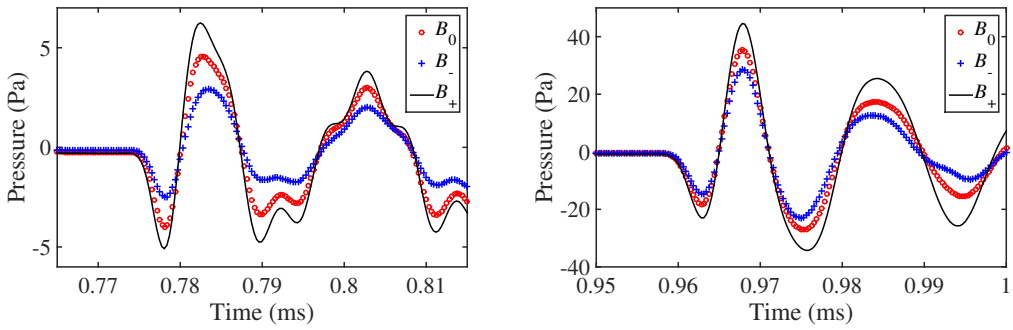

Figure 5.9: Transient pressure signals from (a) transducer A and (b) transducer B, with no permanent magnet (○), with the magnet oriented so that the static and dynamic fields add (−), and with the magnet oriented so that the static and dynamic fields oppose each other (+).

To investigate how the dynamic magnetic field B_d and the static magnetic field B_s contributed individually to the actuating forces in the transducers, the

pressure was measured from transducers A and B without the permanent magnet. Then the magnet was reinserted with switched polarity orientation and the pressure measured again. Fig. 5.9 shows the initial pressure signals from transducers A and B with three different magnet states. B_0 denotes no static magnetic field, B_+ refers to the magnet orientation where the fields add up and B_- is the opposite orientation where the fields subtract.

From the figure it is clear that the main contribution to the Lorentz force is the dynamic field B_d. Significant pressure amplitudes are measured without any static field (B_0), and by adding the magnet the amplitude can be increased (B_+) or decreased (B_-). Compared to the zero field case B_+ increases the initial pressure amplitude by 26.5% and 25.8% for transducers A and B respectively. B_- decreases the amplitude compared to B_0 by 36.0% and 19.2% for transducers A and B respectively. The effect of the magnet orientation compared to the zero field case in decibels is summarised in Table 5.1.

Table 5.1: Pressure amplitude of transducers A and B for different magnet polarities, relative to the zero field amplitude.

Transducer	B_+ (dB)	B_- (dB)
A	2.0	-3.9
B	2.0	-1.9

It is not obvious why the B_- magnet orientation in transducer A produces the largest change in amplitude. In the theoretical investigation of plate vibrations in §3.1 only the transverse component of displacement was considered. In reality there will be some coupling between vertical and radial displacement. It could therefore be that the in-plane component of the Lorentz force from the B_- field opposes the radial displacement coupled to the transverse mode vibrations of the plate.

The measurements for B_+ and B_- were repeated by changing the direction of the generation current while keeping the magnet orientation the same. The behaviour was completely equivalent, as expected from equation (5.13). In both figures, and especially Fig. 5.9b, a compression of the first wavelength of the signal was seen. The first half period $T/2$ of the signal from transducer B has an associated frequency $f = 1/T \simeq 100$ kHz, which is almost twice that of the resonance frequency. As the transducer rings down, without being forced, the wavelength extends and the frequency decreases to the fundamental mode frequency. This is partly because of the high frequency content of the generation current, as seen in Fig. 5.7b, but also because the Lorentz force from the dynamic magnetic field B_d has twice the

frequency of the force from the static field B_s.

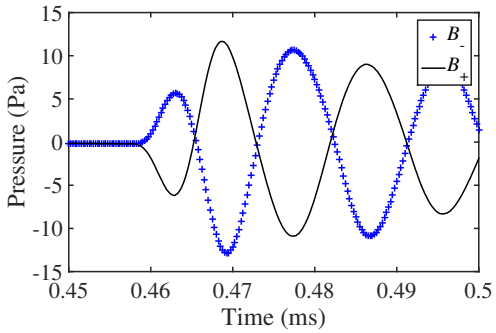

Figure 5.10: Transient pressure signals from transducer C, for opposite current directions in the generation coil.

The magnet could not be removed and its orientation not easily switched in transducer C. Since the magnet is part of the housing (see Fig. 5.4c) that defines the dimensions of the flexural plate the B_0 case could not be tested. The pressure signals for B_+ and B_- were however measured by reversing the direction of the generation current. Fig. 5.10 shows the pressure signals from transducer C with the two opposite current directions. Instead of a fractional change in the amplitude a full 180° phase shift was observed. This means that the net Lorentz force changes direction as the current changes direction, and the force contribution from the static magnetic field B_s is dominant. This also results in a less compressed first period of the signal, compared to transducers A and B, since the Lorentz force from the static field has half the frequency of the force from the dynamic field. It is interesting how different the transducers B and C behave in relation to the electromagnetic coupling, given that the same magnet was used in both designs.

To test the detection sensitivity of each transducer a commercial air-coupled ultrasound transducer (Airmar 50 kHz) was used as transmitter. The pressure signal from the transducer, measured with the acoustic microphone, and the associated frequency spectrum are shown in Fig. 5.11. The pressure amplitude is approximately 9 Pa, which is similar to the output from the transducers A and C (see Fig. 5.8). The frequency is centred at 50 kHz with a FWHM = 6 kHz. Although the bandwidth is narrow it covers the frequency range of the EDFTs.

The generating transducer was placed 40 cm from the receiving EDFT. The receiver was connected to a standard 20 dB EMAT amplifier. Fig. 5.12 shows the receive signals from the three EDFTs and the associated frequency spectra. Because of low SNR, the signals were averaged 128 times and frequency filtered with a low pass filter (-3 dB at 300 kHz). The receive amplitudes for the transducers A,

B and C are 0.6 mV, 1.1 mV and 1.6 mV respectively. The frequency spectra of the transducers are similar, transducer A having a slightly smaller bandwidth. In general, the bandwidth of the received signal is close to the bandwidth of the signal generated by the Airmar transducer as measured with the acoustic microphone (see Fig. 5.11b). Since flexural transducers are narrowband devices, this would not be true for a broadband source. Transducers B and C do not accurately capture the centre frequency of the Airmar transducer, which is overestimated by approximately 2 kHz. This is another consequence of using a resonant system, where the transducers will skew the received signal frequency towards their mode frequency. As seen in the transmission data (Figure 5.8) both transducers B and C have a mode frequency above 50 kHz, which explains the shift in centre frequency of the receive signals.

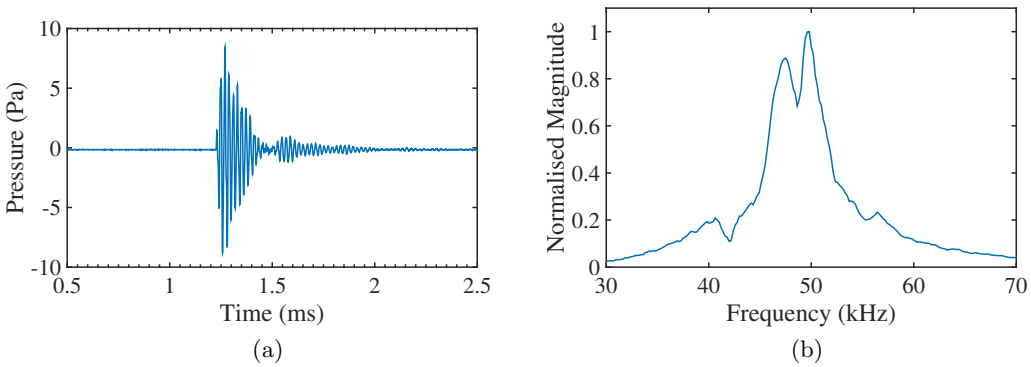

Figure 5.11: (a) Pressure signal from a 50 kHz Airmar transducer measured with a broadband acoustic microphone and (b) the associated frequency spectrum.

The sensitivity of the EDFTs is not high, but is in line with what can be expected from an EMAT receiver. Because low SNR is a well known problem in some EMAT applications, there already exists a body of research into mitigating it. SNR can be improved, as above, by averaging and frequency filtering. There are also more advanced linear and non-linear filtering techniques using both finite and infinite impulse response filters[92] and discrete wavelet transform methods[93]. A comparison of the different de-noising procedures for EMATs can be found in[94], where a 27 dB enhancement of SNR was reported for the wavelet transform method.

A transmit-receive experiment was made with transducers B and C. Transducer B was used as transmitter and transducer C as receiver, as they had the greatest output amplitude and sensitivity respectively. Fig. 5.13 shows the receive

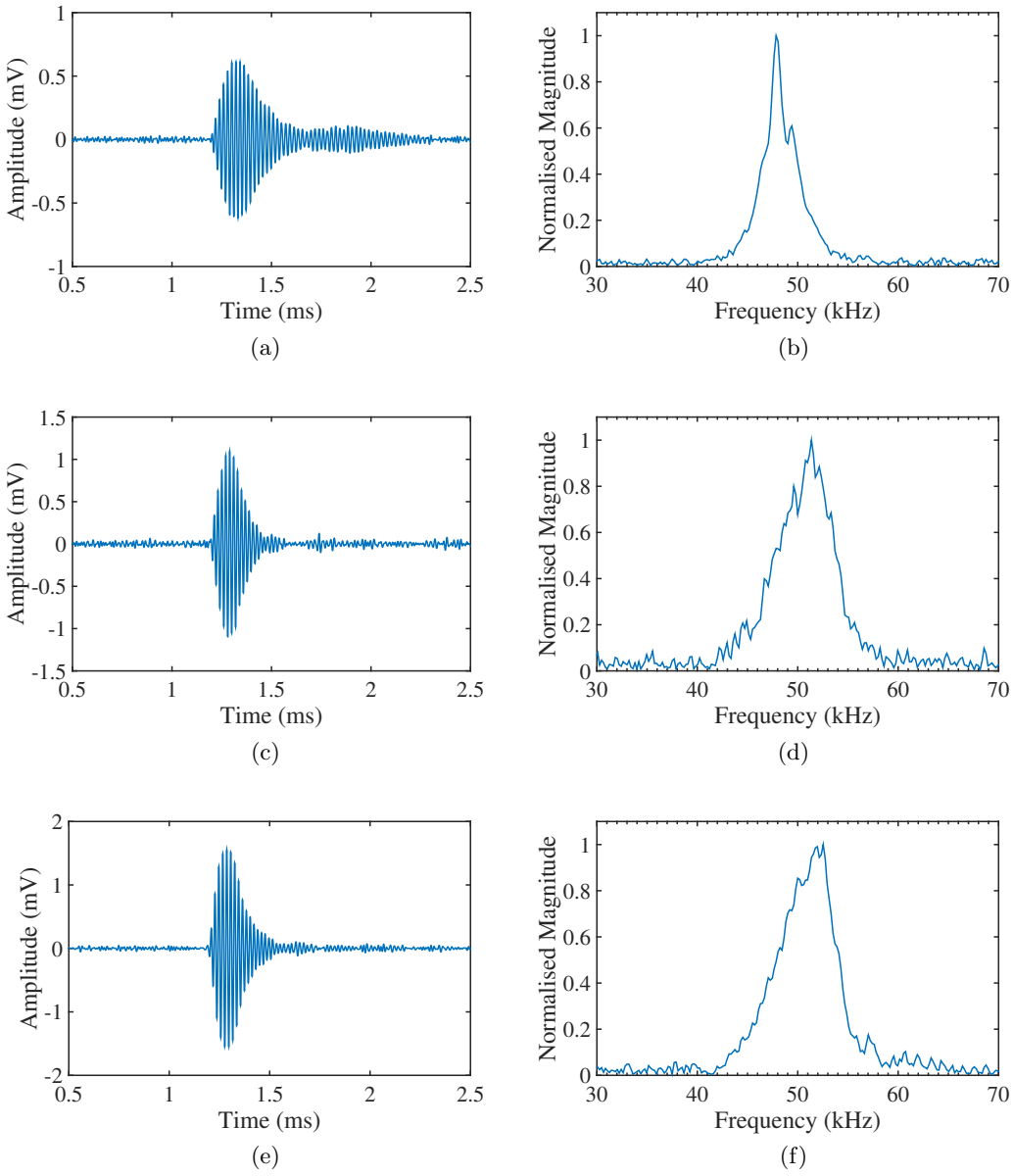

Figure 5.12: Receive signals from (a) transducer A, (c) transducer B and (e) transducer C. The associated normalised frequency spectrum of each signal is shown in (b), (d) and (f) respectively.

signal with 128 averages. The peak amplitude measures 30 mV, which is roughly 0.67 mV per pascal, using the value for peak pressure amplitude measured with the acoustic microphone. This is a higher voltage per unit Pascal than in the previous experiments with the Airmar transmitter, because of the greater number of cycles in the wave produced by transducer B. Apart from the higher amplitude, the longer ring down of transducer B causes greater resonance in the receiving transducer. The signal was clearly measurable with a single shot SNR of 15 dB. This shows that the EDFT system can be used for transmit-receive applications in air over a distance of 40 cm.

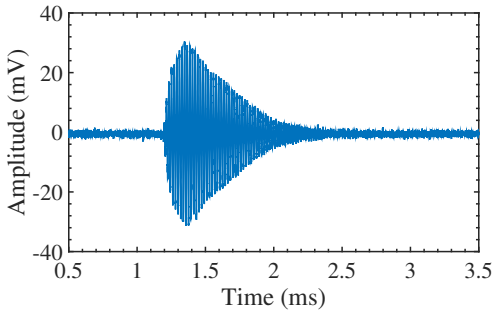

Figure 5.13: Receive signal from transducer C with transducer B as transmitter at a distance of 40 cm and with 128 averages.

To summarise and compare the results from the three different designs, Table 5.2 gives for each transducer the active surface area (i.e. the area of the flexing plate), SPL, centre frequency and sensitivity. The sensitivity is given as received voltage per unit of acoustic pressure. The centre frequencies are taken from the transmission measurements, as these were not influenced by the characteristics of the commercial Airmar transducer.

Table 5.2: Summarised results from the three transducer designs.

Transducer	Area (mm^2)	SPL (dB)	Frequency (kHz)	Sensitivity (mV/Pa)
A	63.6	109	48	0.07
B	436.9	127	52	0.12
C	172.8	112	51	0.18

5.4.1 Characterisation of Transducer C

Transducer C (Fig. 5.4c) was further characterised, because of its higher sensitivity and more complex structure. Fig. 5.14 shows the front face velocity of the trans-

ducer, measured using the laser scan setup outlined in §2.2. The increased noise at $r > 12$ mm is due to the increased noise picked up by the vibrometer at the edge of the transducer surface in the corners of the scan. The velocity was measured instead of the displacement as the displacement amplitude was too great and saturated the Polytec vibrometer. The transducer was excited with the same EMAT pulser that was used in the previous section.

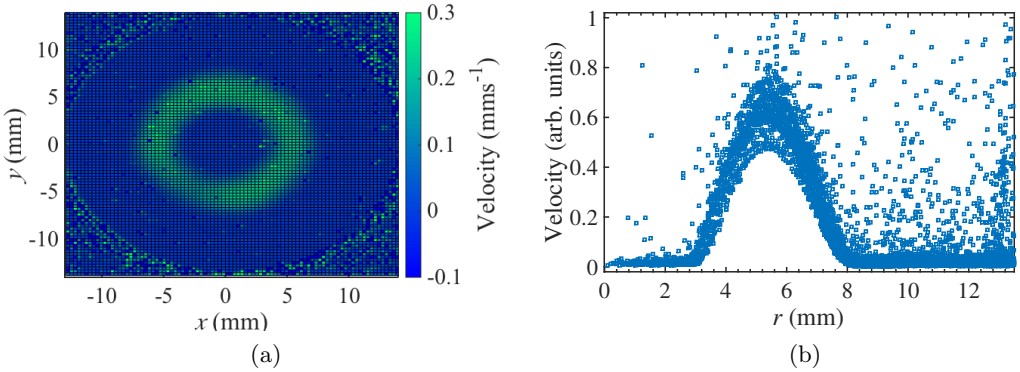

Figure 5.14: (a) Surface velocity snapshot at maximum amplitude and (b) peak-to-peak velocity of each point plotted against the radial distance away from the centre of that point.

Spurious data points are apparent in both figures, and result from local loss of signal strength from the Polytec due to surface roughness. The general mode shape is however apparent, and clearly displays the fundamental mode of an annular plate, with vibrations in phase across the whole radiating surface. From Fig. 5.14b it is seen that the vibrations of the plate are well contained by the magnet and iron core, between 3 mm and 8 mm. The whole area of the transducer front face is significantly greater than the active area that generates the ultrasound wave. This is one of the costs of the magnet placement in the design of transducer C, compared to the other two designs. The ratio of active to overall front face area is 0.30, but could be increased by using a larger magnet.

The front face velocity data was used to predict the transducer directivity. The discretised Rayleigh integral (see equation (1.30)) was used as explained in §1.1.3 to sum the pressure contribution from each area element (i.e. each point of measurement) of the transducer surface. The pressure amplitude along a 180° arc 30 cm from the centre of the transducer front face is shown in Fig. 5.15. The directivity is not entirely symmetric, with a larger sidelobe on one side. The sidelobes are found at $-50°$ and $45°$ respectively. The amplitude does not go to zero at $\pm 90°$,

which could be an artefact of the discretisation of the Rayleigh integral, as was observed for the plane piston in Fig. 1.5. The beam width of the main lobe is roughly 70°.

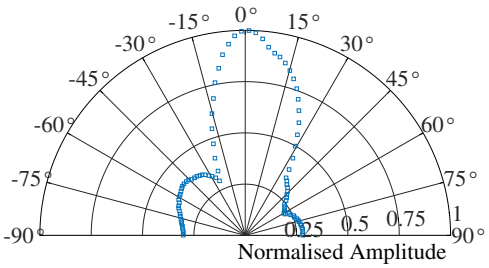

Figure 5.15: Predicted far-field directivity of the EDFT, from the front face velocity data.

The transmit directivity of the transducer was also measured experimentally, using the setup outlined in §2.4 and Fig. 2.3. Fig. 5.16a shows the pressure amplitude plotted against angle for a 180° horizontal sweep in 2° increments. The distance between the centre of the transducer and the microphone was 30 cm. The transducer has a main beam width of 70° and sidelobes at ±60°. The sidelobe level is between −7 dB and −10 dB. This makes the transducer relatively directional, with little potential interference from sidelobes.

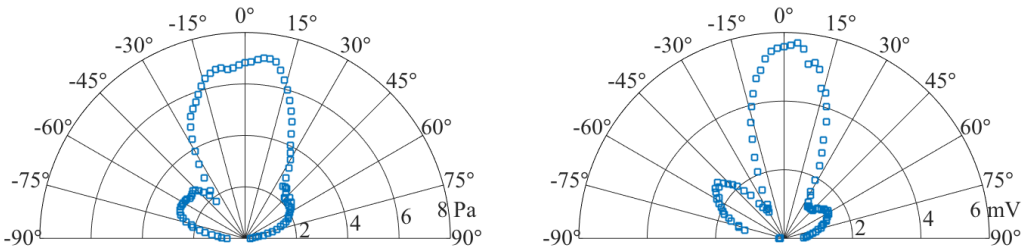

(a) (b)

Figure 5.16: (a) Transmit directivity and (b) receive directivity of transducer C.

Comparing the measured directivity to the predicted directivity displayed in Fig. 5.15 shows some agreement. The width of the main lobe is accurately represented, and the sidelobe levels are similar, but the angles of the sidelobes are greater in the measured data.

The receive directivity of the transducer was also measured, and is shown in Fig. 5.16b. The transducer was connected to an oscilloscope via an EMAT pre-amplifier, and the microphone in the directivity setup was replaced by the 50 kHz Airmar transducer (see Fig. 5.11). The main lobe is narrower in receive mode, with a 60° beam width. The sidelobes are still located at approximately ±60°, with the largest sidelobe having an amplitude of −8 dB.

5.5 Conclusions from EDFTs

The electrodynamic flexural transducer is a novel addition to the air-coupled ultrasonics family of transducers. Three different designs of 50 kHz EDFTs were shown to work both for generating and receiving ultrasound waves in air.

Transducers A and B could both generate ultrasound waves in air without a permanent magnet, relying only on the dynamic field B_d from the generation coil. In fact, even with the static field, the contribution to the Lorentz force (equation (5.13)) actuating the transducer was predominantly from the dynamic field. The permanent magnet increased the pressure amplitude by about 2 dB. A stronger magnet could increase the amplitude more, but a larger magnet would not fit inside the housing. In transducer C the static field provided the main contribution to the Lorentz force, as seen by the 180° phase shift in the pressure signal when the current direction was reversed (Fig. 5.10). This fundamental difference in the actuation of transducers A and B compared to transducer C highlights the importance of the magnetic field direction.

Because the EMAT pulser that was used produced a broadband output, the resonance properties of the flexural system are not fully utilised. As was seen for the piezoelectric flexural transducers in Chapter 4, the displacement amplitude and output pressure increase significantly with additional driving cycles. Hence, it would be reasonable to assume that the output could be enhanced by exciting the EDFTs with a toneburst signal. Or alternatively, the amplitude could be kept constant and the voltage of the pulser reduced.

Transducers B and C have an additional element of freedom in terms of design. Assuming the availability of ring magnets with arbitrary size, the inner and outer bounding radii of the annular plate can be individually changed. This allows the active area, i.e. the area of the front face displacing the load medium, to be modified while keeping the resonance frequency constant. In comparison, for transducer A, increasing the aperture size and active area is associated with a decrease in mode frequency in accordance with equation (3.16).

The annular design of transducer B lends itself well to making annular arrays (see Fig. 1.15c), which with suitable electronics could be focused for even higher sound pressure levels at the required distance. From the dimensions of the EDFTs, given in Fig. 5.5, it is seen that transducer A would easily fit inside the hollow centre of transducer B. The two could hence be combined to give a larger active area and enhance both pressure output and input sensitivity.

Transducer C was shown to operate in the fundamental mode of an annular plate with clamped inner and outer radii. The radiation pattern produced by this mode featured a large main lobe with 70° beam width and sidelobes at ±60 with a sidelobe level of −8 dB.

Chapter 6

Evaluation of Flexural Transducers for Flow Applications

The discussion of flexural transducers for flow applications will be limited to piezoelectric flexural transducers. They have a number of qualities that would be beneficial in a flow meter. Because flexural transducers can be operated at a lower voltage compared to standard piezoelectric transducers, meeting intrinsic safety requirements becomes easier. Modern commercial ultrasonic flow meters can be driven with voltages as low as 40 V, by using advanced digital signal processing to compensate for the related low SNR. This voltage is still significantly higher than those commonly used for flexural transducers. In Chapter 4 concerning piezoelectric flexural transducers, all characterisation of the transducers was done with $V_{\mathrm{pp}} \leq 10$ V driving voltages.

Another advantage of the low voltage is the related low power consumption of flexural transducers, which allows for battery compatible meters. These type of meters are becoming increasingly important for networks of meters covering remote locations, or locations that are not easily accessible.

A common point of failure in current ultrasonic transducers employing matching layers, is the debonding of the matching layer from the piezoelectric element. A flexural transducer does not have a matching layer and therefore eliminates one of the bond layers. This could potentially prolong the lifetime of the transducers in a flow meter. Furthermore, by removing the matching layer the number of construction steps is reduced, which could make production of transducers faster and more cost effective.

The passive layer of the flexural transducer, i.e. the metal cap, provides inherent protection of the active element of the transducer from the fluid. This gives the transducers the necessary ruggedness for industrial flow measurements. The titanium caps that were characterised in §4.4.4 and used to make 100 kHz flexural transducers could be used with conventional matching layer transducers to protect matching layer, piezoelectric element and electronic connections. In such transducers however the metal cap is associated with signal loss and pulse distortion. The flexural transducer on the other hand use the cap to generate the ultrasound waves in the fluid.

There are also some potential problems with using flexural transducers for flow applications. Flexural transducer cannot be backfilled with a hard setting material as this would kill the flexural vibrations of the cap. This makes the transducer susceptible to being damaged at elevated pressures. At sufficiently high pressures the passive layer might collapse inwards, unless pressure equalisation is engineered into the design.

As has been seen in previous chapters, flexural transducers have a narrow frequency bandwidth and long ring down. For flow applications the low bandwidth is not a disadvantage, as only the transit time is of interest, and transmitting and receiving transducers have the same operating frequency. The ring down time however limits the repetition rate of the meter, as the ultrasound waves in the pipe have to disperse before the same transducer can be fired again. This can be mitigated to some extent in a multipath meter, where active transducer pairs can be cycled.

6.1 Flow Measurement Techniques

Ultrasonic flow metering was first introduced as an application of fluid coupled ultrasound transducers in §1.3.1. In order to put the ultrasonic flow measurement technique into context some other contemporary flow measurement techniques should be introduced. The range of flow meters discussed here is not comprehensive, but presents some of the more commonly employed technologies: Turbine meters, differential pressure meters, thermal meters, Coriolis meters and electromagnetic meters. For each type of meter the basic principles of operation are explained, as well as some of their advantages and disadvantages.

6.1.1 Turbine Meters

Turbine meters[95, 96] are some of the most versatile mechanical flow meters, as they can be produced in a wide range of sizes, and are suitable in both high pressure and

high temperature environments. The meters can also reach high precision ($\sim 0.15\%$) and are intrinsically safe.

The operation of a turbine meter can be understood largely intuitively. The turbine consists of a rotor with blades at an angle to the flow, which turn due to the fluid flowing past the blades. The rotation of the turbine is then related to the mass flow rate of the fluid. The blades can be straight or twisted (helical). Although a local pressure drop is unavoidable as the fluid imparts some momentum to the turbine, in most meters the rotor is designed to minimise the disturbance to the flow. Ideally the blades cut perfectly through the fluid in a helix. In practice, drag forces that impede the rotation limit the efficiency, but overall the energy extracted from the fluid is small.

Bearings and structures that are necessary for holding the turbine in the pipe introduce a larger pressure drop than the rotor itself. It is however common practice to combine these structures with flow straighteners[97]. Straighteners usually consist of a plate with holes or short pipes, which constrain radial motion of the fluid, and hence force the flow to straighten as it passes through the plate. The turbine meter is one type of meter particularly sensitive to swirls in the flow, and can therefore benefit significantly from eliminating these upstream of the rotor section.

The mechanically moving parts introduce some problems of their own as friction in the system, which can change and develop over time, will affect the meter readings. The moving parts also reduces the life time of the turbine meter. Also, because the turbine meter has to be installed inside the pipe (in the flow), access to the meter becomes a problem, which can significantly increase costs and downtime associated with maintenance.

6.1.2 Orifice Plates and Venturi Meters

The orifice plate meter[98] measures the difference in pressure upstream (before) and downstream (after) a precise constriction in the pipe, which is used to calculate the mass flow rate. It is one of the most common types of differential pressure meters. Fig. 6.1 shows a schematic diagram of a typical orifice plate meter setup. It is seemingly simple to construct, as it essentially comprises a metal plate with an orifice inserted between flanges with pressure tappings in the pipe wall. However, the flow through the meter is complex and the tolerance on the dimensions of the plate and the pressure tappings has to be small to achieve the necessary precision. The orifice plate meter can have a precision just under 1%, but could often be much worse depending on the specific installation details and manufacturing tolerances.

The differential pressure is measured by manometers, Bourdon tubes, or

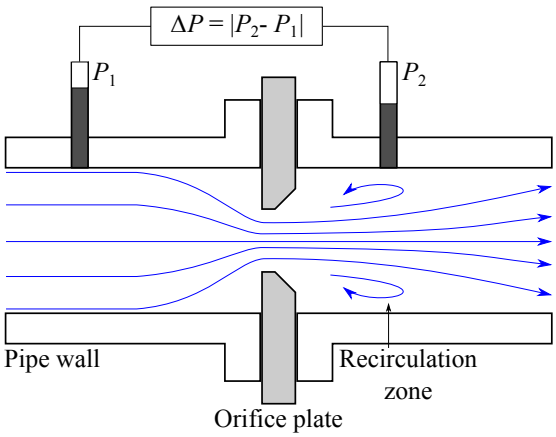

Figure 6.1: Schematic diagram of an orifice plate meter in crossection.

electromagnetic pressure transducers[99]. The flow is then deduced from experimentally derived equations. The mass flow rate is proportional to the square root of the differential pressure.

Because the precision of the orifice meter is closely tied to the precise installation of the plate and pressure tappings, the meter is especially susceptible to wear. This can become a problem especially when dealing with a corrosive or abrasive fluid. Similarly, fluids that leave deposits could affect the diameter of the orifice and hence degrade the precision of the meter. Another problem with the orifice plate meter is the large pressure drop downstream of the plate, which inevitably leads to energy losses.

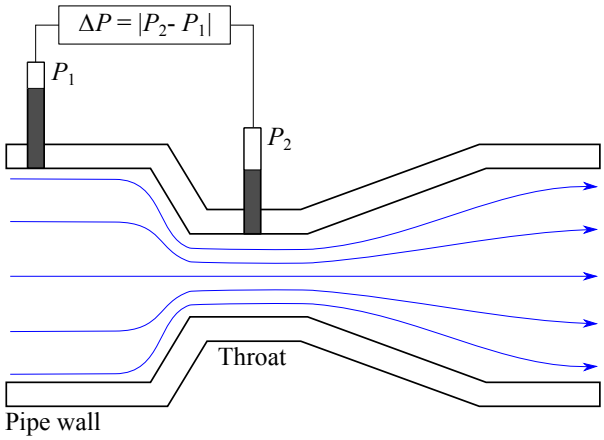

Figure 6.2: Schematic diagram of a classical venturi meter in crossection.

The venturi meter is another differential pressure meter, similar to the orifice plate meter in operation. Instead of a plate with a fixed diameter orifice, the venturi

meter has a tapered constriction as shown in Fig. 6.2. The flow converges and passes smoothly through the constricted section, known as the throat, and subsequently out through a diverging cone. This gradual reduction and then expansion of the pipe crossection decreases recirculation. The pressure is measured upstream before the converging cone where pressure is at a maximum, and again at the throat where the flow velocity is at a maximum and the pressure at a minimum, which gives the largest differential pressure.

In general the diverging angle downstream from the throat is smaller than the inlet angle, which results in a better pressure recovery. The total pressure drop across the whole meter is much smaller than that for the orifice plate meter. These characteristics make the venturi meter more appropriate in applications where low energy consumption is important. Also, because of a smaller recirculation zone, the venturi meter can better handle some multiphase fluids such as oil water mixtures.

6.1.3 Thermal Meters

The heat loss from an object immersed in a fluid is susceptible to the flow rate of the fluid. An in-line thermal mass flow meter[98] uses two electronic temperature sensors, and a heating element combined with one of the sensors, as illustrated in Fig. 6.3. The temperature difference between the two sensors is measured and kept constant by feedback to the heating element. The flow rate can then be calculated by monitoring the power consumption of the heating element. In Fig. 6.3 the two sensors are placed upstream and downstream, but it is also common to have the sensors perpendicular to the flow.

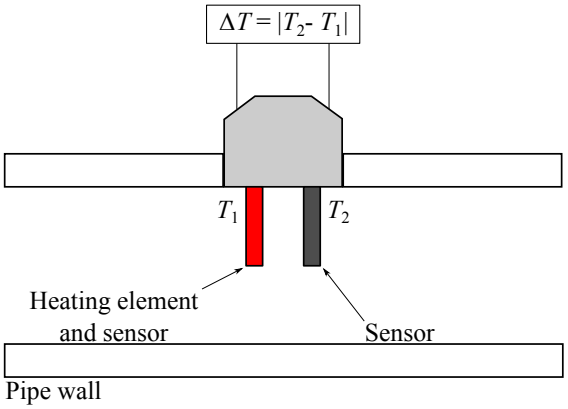

Figure 6.3: Schematic diagram of an in-line thermal mass flow meter setup in crossection.

This type of thermal meter has a limited impact on the flow, depending

on the size of the heat sensors. As the meter only samples a limited crossection of the flow in the pipe, the precision is somewhat susceptible to the flow profile. The response rate of the thermal meter is relatively low, as it depends on the heat convection from the sensors.

6.1.4 Coriolis Meters

A Coriolis mass flow meter[100, 101, 102] derives its name from the Coriolis effect[103], which is an important phenomenon in fluid dynamics. The effect describes how an object observed from a rotating reference frame experiences a deflecting force.

The Coriolis meter consists of a fluid conveying conduit, which can be imparted angular momentum by an electromagnetic vibrator. The movement is translated to the flowing fluid in the conduit, which causes particles of the fluid to experience Coriolis acceleration. Resulting forces from the fluid are proportional to the product of velocity and density, and generate local pressures on the conduit walls. These pressures cause a measurable deflection of the conduit, as illustrated in Fig. 6.4. In the U-tube Coriolis meter, the forces on the conduit produce a twisting motion, which is related to the mass flow rate. The deflection is often measured by electromagnetic or optical sensors.

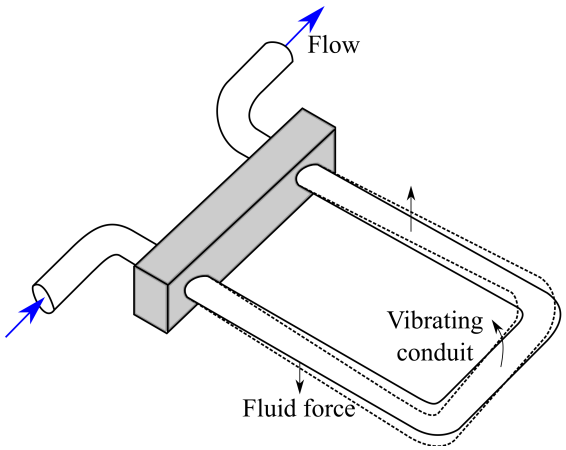

Figure 6.4: Schematic diagram of a single loop, or U-tube, Coriolis meter. In the diagram the Coriolis forces that produce a twisting motion as the conduit moves upward are shown.

Under normal operation a precision better than 0.5% is common. Other advantages of the meter include compact design, low power consumption and low maintenance requirements. The pressure loss across the meter is one of the disadvantages.

6.1.5 Electromagnetic Meters

The electromagnetic flow meter uses Faraday's law (see equation (5.3)), which describes the electromotive force induced in a conductor travelling though a magnetic field, to calculate the mean velocity of a fluid through a conduit. The first flow meter of this type was developed in 1930. Much of the subsequent development was driven by the medical field[104, 105], where the electromagnetic meter was used for blood flow measurements.

To measure the flow, a uniform magnetic field is set up across the conduit. As the fluid moves through the field, charged particles experience a Lorentz force (see equation (5.13)). Assuming the fluid has non-negligible conductivity, the Lorentz force causes charge separation, which leads to a detectable potential difference across the diameter of the pipe. A simple setup of an electromagnetic flow meter is shown schematically in Fig. 6.5.

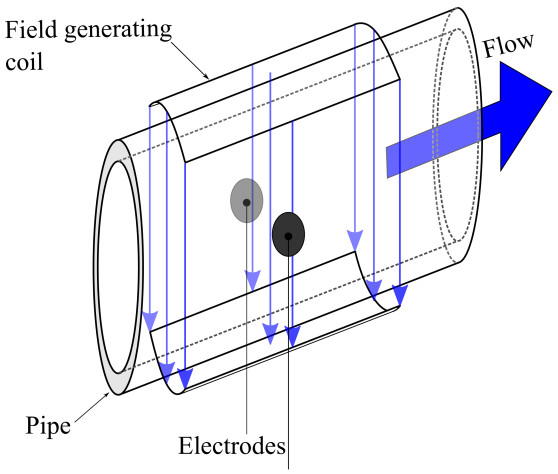

Figure 6.5: Schematic diagram of an electromagnetic flow meter.

The pipe has to be non-magnetic to allow the magnetic field to penetrate the pipe. Usually the field is created by coils excited by an alternating current. The voltages in the fluid are measured between two electrodes that are set in the wall of the pipe. The inside of the pipe has to be coated by an insulating material to avoid shorts. Even though the electric currents and eddies created as the fluid cuts the magnetic flux lines are complicated, for a large range of flow conditions, the expression for the potential difference across the electrodes is given by

$$\Delta V = B D_p \overline{v}, \tag{6.1}$$

where B is the magnetic field strength, D_p is the diameter of the pipe and $\overline{v}$ is the

mean flow velocity in the pipe. The equation (6.1) only holds true for a uniform magnetic field and for an axisymmetric flow profile. Any fully developed flow profile in a cylindrical pipe will be axisymmetric, but it is not always practical or even possible to let the flow fully develop before the meter. Work has been done to deal with distortions in the flow profile by, for example, the use of a weight function[106, 107]. The effect can also be limited by using extended electrodes.

Electromagnetic meters will work on any conducting fluid, generally considered as any fluid with a conductivity above $\sigma = 4 \times 10^{-4}$ Sm^{-1}, although research into measurements on fluids with a lower conductivity has been done[108]. Similar to the ultrasonic meter, the electromagnetic meter has very little influence on the flow, and there is no significant pressure drop after the meter section. Also, an electromagnetic meter has no moving parts, which prolongs the life time of the meter.

6.2 Experimental Setup of Flexural Transducers for Flow Measurements

Three different types of experiments were conducted to evaluate the potential use of the 100 kHz titanium flexural transducer (from §4.4.5) for flow applications. In the experiments focus was put on the signal shape retention, as this is one of the most important transducer properties for transit time ultrasonic meters. The precision of the meter depends on the accurate measurement of time delays upstream and downstream, which are used in equation (1.45) to calculate the flow velocity v. The delays are calculated by comparing the delayed signals to a reference signal, recorded at zero flow. Different methods and algorithms exist for calculating the delay between two signals. In ultrasonic flow metering both zero crossing methods and cross correlation methods[109] are common, and particularly for techniques using cross correlation, signal shape distortion is detrimental to measurements.

To allow the flexural transducers to be fixed into a meter body they were glued into a larger aluminium holder, which was backfilled with a hard set epoxy. In order to backfill the aluminium holder without damaging the transducer, each transducer was fitted with a lid assembly, which sealed the transducer whilst leaving an air-gap inside. This also made the transducers more robust.

6.2.1 Elevated Static Pressure

A transducer pair was fitted into a meter body sealed at both ends, with a manual pump and a pressure gauge. The transducers were used in transmit-receive mode as the pressure was increased from ambient to 12.8 bar. Because the transducers were fitted into a pre-made meter body, with set paths, the distance between the transducers was fixed. The distance was measured by TOF to be approximately 22 cm.

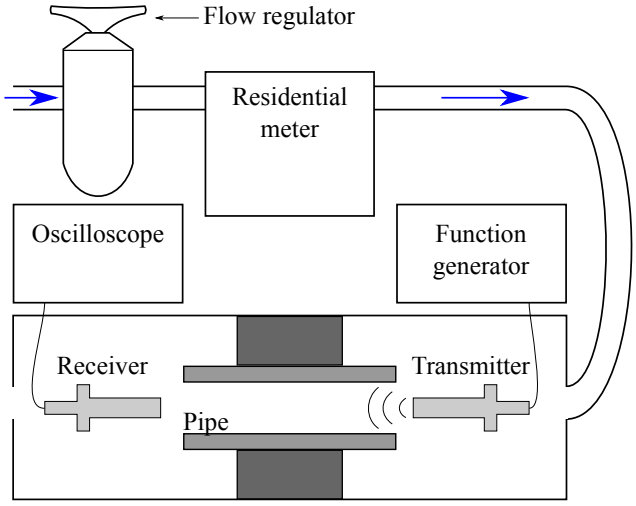

Figure 6.6: Schematic diagram of setup for measuring flow velocity from a pressurised air supply with a flow regulator. The transmitter and receiver were 100 kHz titanium flexural transducers.

6.2.2 Air Flow

In residential gas meters a different transducer setup can be used, where the ultrasound waves travel parallel to the flow. The measured time delays of upstream and downstream signals are no longer reduced by the $\cos(\theta)$ factor, which makes measurements of the delays easier. On the other hand, the flow is disturbed to a much greater extent in this type of meter compared to the type of ultrasonic flow meter introduced in §1.3.1. A schematic diagram of the setup used is shown in Fig. 6.6.

6.2.3 Water Flow Rig

The flow rig that was used is described in detail in [110] and [111]. A small, straight, single path, flow meter was constructed, again using a pair of the titanium flexural transducers. Fig. 6.7 shows the meter section used in the flow rig.

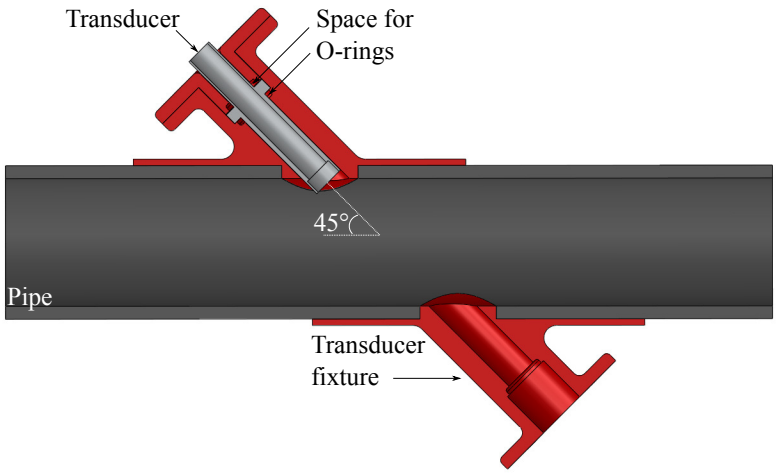

Figure 6.7: SolidWorks CAD diagram of straight path flow meter setup in crossection. The diagram shows only one of the transducers inserted into the meter.

The meter was made by drilling holes into a pipe section and gluing in two transducer fixtures. The fixtures were designed in CAD program SolidWorks and 3D printed using ABS plastic. They were designed to give a 45° angle to the flow. The pipe diameter was 50 mm, giving an ultrasound path length of $L = 70$ mm. Normally, for accurate flow metering, the distance L has to be determined very precisely. However, this was not feasible with 3D printed fixtures and hand drilled openings in the pipe. With this in mind, the setup could still be used to evaluate if the transducers were capable of precise (as opposed to accurate) measurements of flow. Two O-rings and a rubber gasket (not shown in the diagram) were used in each transducer fixture to stop leaks. For high flow rates (> 100 kgms^{-1}) there was however a small leak from both transducers. A commercial Coriolis meter was used to measure the mass flow rate, which was varied between 50 kgms^{-1} and 170 kgms^{-1}.

6.3 Results

6.3.1 Elevated Static Pressure

The static experiment at increased pressures showed a non-linear amplitude response, as seen in Fig. 6.8a. There is an initial large increase in signal amplitude as the pressure is increased from ambient to 1.2 bar. This is followed by a relatively flat region up to 3.0 bar, and then a sharp drop back to ambient pressure amplitude level as the pressure was increased to 6.4 bar. The amplitude then starts to increase

slowly again and has a positive gradient when the setup reaches maximum capacity at around 12.8 bar. The initial amplitude gain as the pressure is increased from ambient has previously been observed for standard matching layer transducers in flow meters, which was ascribed to better coupling between the piezoelectric element and the matching layer, and between the matching layer and the protective metal cap. This explanation is however not satisfactory for the flexural transducers used in this experiment. A potential explanation is an increased energy transmission due to an increased load impedance. Since the transducers are not pressure equalised, pushing the air in front of the transducer requires a larger force, which translates into a higher mechanical impedance, which would be closer to the effective impedance of the flexural transducer. The drop in amplitude that follows the increase is explained by the greater force needed to bend the front face outwards at increased pressures. Regarding the slow increase in amplitude at higher pressures, further research will be necessary to determine the reasons for this trend.

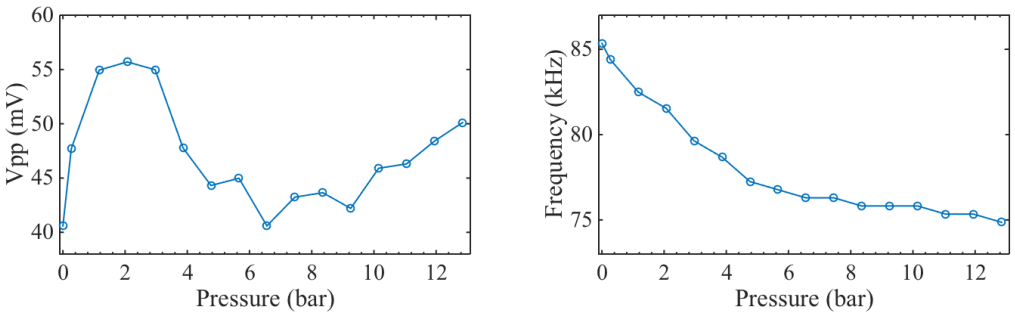

Figure 6.8: (a) Receive signal peak-to-peak amplitude and (b) receive signal centre frequency, for static pressures from 0 bar (ambient) to 12.8 bar.

The centre frequency of the received signal also changes as the pressure is increased, as seen in Fig. 6.8b. The change in frequency is however more predictable than the amplitude, and follows an almost exponential decline with increased pressure. The transmitter is driven by a function generator with a 100 kHz, 3 cycle, 10 V_{pp} sinusoidal signal. The received signal on the other hand has a lower frequency, starting at just over 85 kHz at ambient pressure, and going down to 75 kHz at 12.8 bar. This drop in frequency is due to the increased force necessary to bend the plate. That is, the increased pressure increases the effective inertia of the plate, which decreases the resonance frequency of the system.

Fig.6.9 shows the receive signal at four different pressures. Apart from the

change in amplitude the signal shape is undistorted for small changes in pressure. At 12.8 bar the signal shape has been significantly distorted. The initial part of the signal is however similar, and could still be used to measure transit time. In general, using the zero crossing method for TOF measurements, only the first few cycles of the signal are of interest. Hence, the distortion seen in Fig. 6.9 would not necessarily negatively influence the precision of a flow velocity measurement.

The distortion of the signal that appears at ~ 0.9 ms comes from mechanical crosstalk through the body of the flow meter. As the pressure increases the coupling between the meter body and the transducer increases, as the transducer is pushed into closer contact. This effect could be controlled to some extent by how tightly the transducer was fixed into the body, and with the use of O-rings in areas of contact.

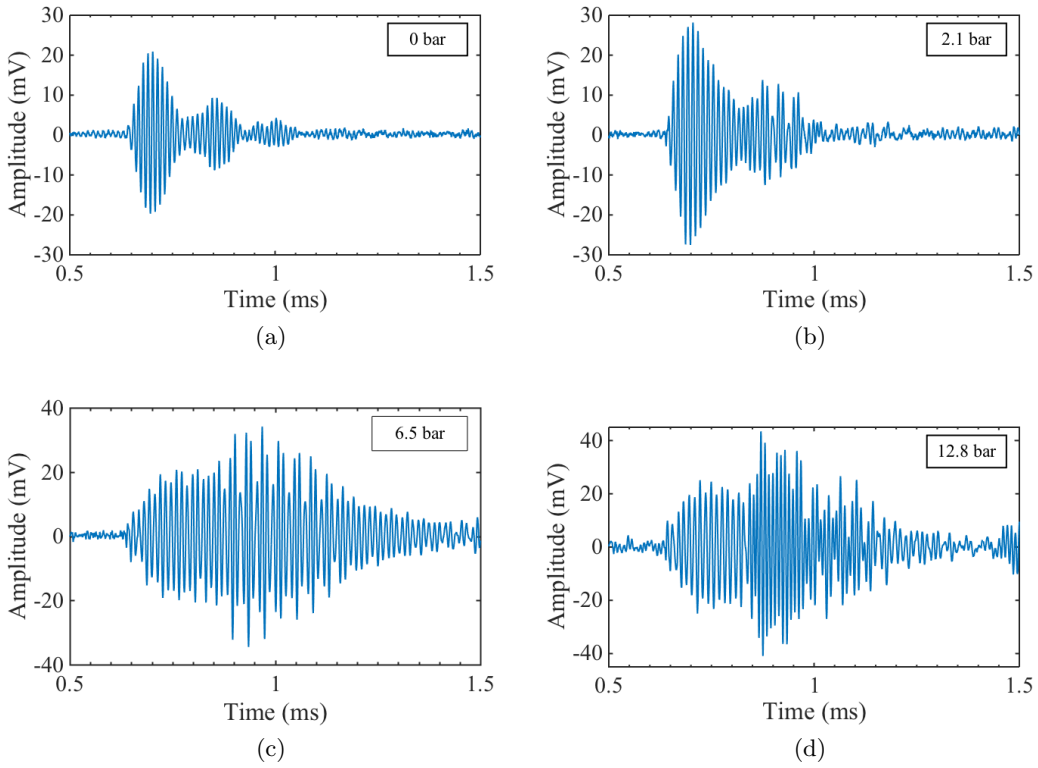

Figure 6.9: Signals recorded at different static pressures: (a) ambient pressure, (b) 2.1 bar, (c) 6.5 bar and (d) 12.8 bar.

6.3.2 Air Flow

Fig. 6.10 shows the flow velocity v, measured with the flexural ultrasound transducers, plotted against the volumetric flow rate as given by a commercial residential gas meter. There is a clear linear relation between the two, which shows that the titanium flexural transducers can be used in these type of gas flow applications. As seen in the diagram of the setup in Fig.r̃effig: the air flow was forced through a pipe section. The pipe section was however not long enough to allow the flow to fully develop, and even better result would be expected for the flexural transducers with an optimised setup.

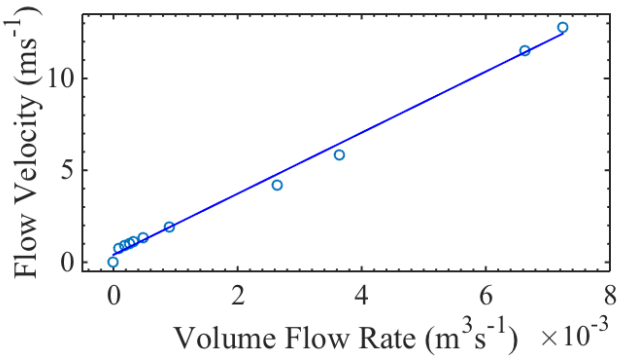

Figure 6.10: Flow velocity from ultrasound TOF measurements in line with air flow, against volume flow rate read from a residential diaphragm meter, and a straight line fit to the data.

There was some signal distortion with increased flow rate, as seen in Fig. 6.11, and hence the zero crossing method was used to calculate TOF. A Matlab script was written and used for finding the zero crossings of each signal and calculating the differences in TOF between different signals.

6.3.3 Water Flow Rig

The experimental setup used to measure the water flow was not precise enough to make accurate measurements of the flow velocity. From the results it became apparent that the path distance between the transducers increased as the pressure increased at higher flow rates. This lead to a measurement bias where the transit time upstream t_u increased more rapidly than expected, and the downstream transit time t_d did not decrease as fast as expected. The reason is probably the plastic fixtures and the O-rings, which would allow the transducers to be pushed back as

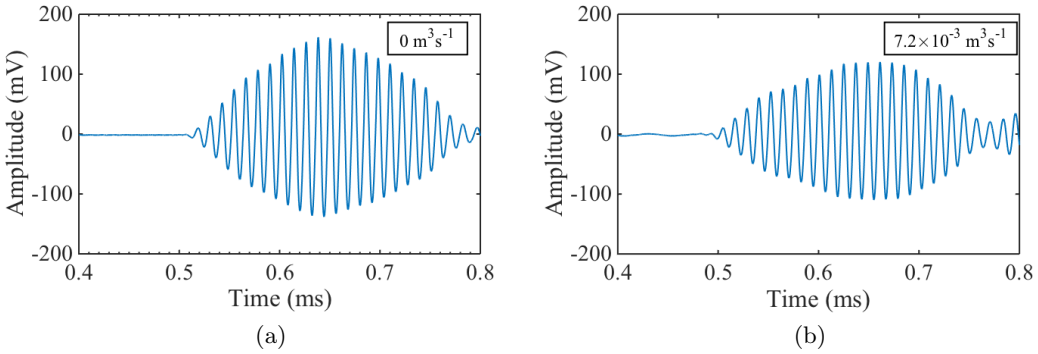

Figure 6.11: Signal from air flow measurements at (a) zero flow and (b) 7.2 m^3s^{-1}.

the pressure in the pipe increased. Fig. 6.12 shows the TOF for upstream and downstream signals as compared to the zero flow TOF.

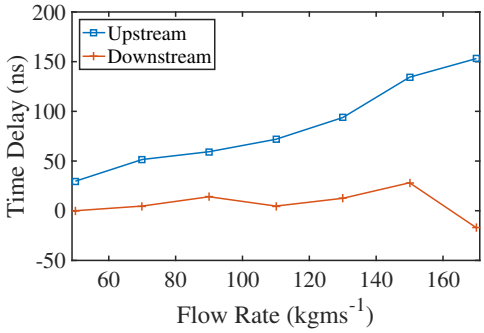

Figure 6.12: Time delay of signals compared to zero flow TOF for different mass flow rates.

However, the transducer performance was good, with large amplitude signals for low excitation voltages and very low signal distortion at high flow rates. Fig. 6.13 shows two signals at different flow rates. The transmitting transducer was excited by a 3 cycle, 100 kHz, 1 V amplitude sinusoidal wave. The receive signal was amplified by a 40 dB amplifier and averaged 16 times. Even with this low excitation voltage the single shot SNR was approximately 15 dB. Overall, the signal amplitude and SNR were higher in water compared to in air, due to the enhanced acoustic coupling into the load medium.

As can be seen from comparing the signals in Figs. 6.13a and 6.13b, the signal shape is very well retained at the higher flow rate, which made cross correlation methods for determining the time delays appropriate.

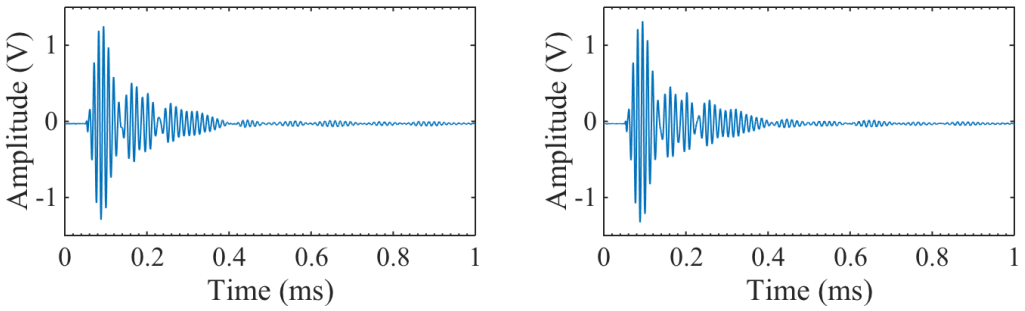

Figure 6.13: Signals from upstream measurements at (a) zero flow and (b) 120 kgms^{-1} mass flow rate.

6.4 Conclusions

The piezoelectric flexural transducers are viable for both liquid and gas flow applications at pressures under 13 bar, and potentially at higher pressures. The static pressure measurements showed that the signal amplitude changed non-linearly with pressure. For small increases in pressure < 3 bar the signal amplitude increased significantly.

In the water flow rig the signal strength and SNR were good and the signal shape distortion low, as seen in Fig. 6.13. Unfortunately, even though the transducers performed well, the experimental setup was not precise enough to allow for accurate measurements of the flow velocity. Because of the greater sound speed in water compared to in air the time delays are very small, which requires very precise determination of the ultrasound path length. The trends of the measured time delays in Fig. 6.12 indicated that the path length increased with increasing flow rate.

Chapter 7

Conclusions

7.1 Piezoelectric Flexural Transducers

The behaviour of piezoelectric flexural transducers was studied in detail. Although some work had been done to develop the theoretical models of unimorph systems[112, 113, 114], little in terms of experimental validation of a real system has been reported in the literature. Existing commercial flexural transducers are limited in operation frequency, and are only typically used in proximity and range finding applications.

The passive layer of the flexural transducer, i.e. the metal cap, was characterised separately before assembly (§4.4). By use of laser induced ultrasound the layer was excited without loading the plate. The out of plane displacement was measured and the frequency modes revealed by Fourier transform. The mode frequencies only depend on the dimensions of the cap, which allowed the tolerance of a batch to be quickly estimated. Since flexural transducers are narrowband devices, frequency matching is important, and significant amounts of time and resources can be saved by discarding unsuitable components before bonding the piezoelectric element and assembling the whole transducer.

This laser induced ultrasound characterisation also helped reveal the influence of the piezoelectric element on the flexural vibrations, both in terms of mode frequencies and mode shapes. Generally the added stiffness of the piezoelectric element increased the mode frequency, but this increase was limited by the mass loading.

A laser scanning system was developed by combining a single point laser vibrometer with the xy-stage of a 3D printer (§2.2). The setup allowed the time resolved transverse displacement or velocity of the radiating face of a transducer to be measured. By using a broadband excitation pulse, individual modes could

be separated out by use of digital frequency filters in post-processing. The results showed how the experimental mode shapes of flexural transducers differ from the theoretical mode shapes of a thin plate. Overall, the central peak was flattened and the outer antinodes had relatively greater amplitudes. From the velocity profile of the surface, the transducer directivity could be predicted by use of Huygen's principle (§1.1.3).

The possibility of using flexural transducers for flow applications was explored. The titanium transducers were operated in transmit-receive mode in air at elevated static pressure, measuring air-flow from a pressurised air supply, and in a water flow rig. The transducers performed well at higher pressures, with the signal amplitude not dropping below the amplitude measured at ambient pressure over the range tested. The air flow from a pressurised supply could be measured with reasonable precision (accuracy depending on calibration). The water flow could not be measured due to problems with the setup, but the signal amplitude and SNR were very good, which suggests that the transducers could successfully be used in this type of application.

A novel method of building an air-coupled phased array was suggested and tested (§4.4.6). The idea was that multiple flexural elements could be defined on a single metal plate by use of rigid baffle bonded to one side of the plate. Experiments showed that the baffle did sufficiently isolate the elements to give them a mode shape and mode frequency close to that of a single element flexural transducer of similar dimensions.

7.2 Electrodynamic Flexural Transducer

A novel electrodynamic flexural transducer (EDFT) was introduced (Chapter 5), that used electromagnetic coupling to generate and receive ultrasound waves in air. The transducer can be made of low cost components and is very robust. Because no piezoelectric materials are used the transducer has potential for high temperature applications.

Because the generation coil is easier to configure than a piezoelectric element there is more freedom in choice of flexural plate geometry. This allowed for the fabrication of annular flexural transducers.

The EDFTs were shown to produce high pressure outputs, but to have relatively low receive sensitivities. Even so, two transducers were shown to work well in transmit-receive mode. The transducers were shown to have a narrow bandwidth, as expected of a flexural device.

7.3 Suggested Future Work

Future research based on this thesis could take many different directions. Already the flexural array technology introduced in §4.4.6 has been greatly improved, resulting in a smaller aperture array with more elements (4×4). Even though the $\lambda/2$ criterion still has not been met, the array has already proved able to steer the main lobe accurately over a large range of angles. The first results from this array will be presented at the IEEE International Ultrasonics Symposium (IUS) in Tours, France, September 2016.

The research of single element piezoelectric flexural transducer has also continued. The idea of screen printing a piezoelectric element onto a thin metal shim to make a flexural transducer is being investigated. By directly printing the active element onto the passive layer and then curing and poling it, all bond layers have been eliminated. Also, by using bismuth titanate as the active material in the screen printing process, high temperature flexural transducers are made possible. Initial results from this type of transducer were recently presented [115].

Another area of application to which flexural transducers might be applied is that of continuous wave (CW) flow measurements. Instead of measuring the transit time of a signal pulse, the phase shift of a continuous wave between two transducers is recorded and related to the flow velocity. Piezoelectric flexural transducer, because of their narrow bandwidth and high quality factor, should be well suited for this application. In CW mode significantly higher pressure amplitudes for similar excitation voltages can be achieved.

In terms of the EDFTs the development of more sensitive designs is a priority. One possible improvement is to use a magnetostrictive material instead of aluminium as the radiating plate, to increase coupling efficiency to the generation and reception coil. Alternatively, a magnetostrictive coating could be applied to the inside of the plate. This coating could also be used as a damping layer, to increase the bandwidth of the device. In general, the use of suitable backing materials for manipulating the bandwidth of flexural transducers is a potential area of further research.

The idea of using EDFTs to make annular arrays was already suggested in §5.5. This is another topic for future work. By varying the inner and outer radii of individual annular EDFTs, they can be designed to fit inside each other, as the individual elements of an annular array, and yet have the same fundamental mode frequency. By using transducers in this configuration the active to total aperture area is increased, the sensitivity is increased, and the potential for focusing ultrasound is introduced.

Apart from the experimental work, a theory describing the coupling between the electromagnetic forces and the flexural vibrations should be developed. There was some indication that the in-plane forces from the out of plane component of the static magnetic field had an impact on the output amplitude of transducer A, which illustrates the need for a better understanding of the underlying physics of the EDFTs.

Appendix A

Conference Papers

Published conference papers by the author:

10.1109/ULTSYM.2013.0408

Flexural Mode Metal Cap Transducer Design for Specific Frequency Air Coupled Ultrasound Generation

T.J.R. Eriksson*, S.M. Dixon* and S.N. Ramadas†
*University of Warwick, UK
†Elster NV/SA, Belgium
Email: t.j.r.eriksson@warwick.ac.uk

***Abstract*—Flexural transducers are effective ultrasonic generators in fluid media, where standard piezoelectric transducers suffer a significant performance loss due to a large impedance mismatch. The flexural modes of piezoelectrically actuated metal caps are routinely used to make low frequency (typically 40 kHz) air coupled transducers for simple distance measurements. Such transducer types offer many intrinsic advantages including an integrated metal buffer for environmental shielding, good fluid coupling for generation and detection of ultrasound, and large amplitude signals for a low driving voltage. In this work, we investigate the design of arbitrary and specifically higher frequency ($>$ 100 kHz) flexural metal cap probes. The analytical theory of vibrating plates was used to determine how the geometry of the cap affects the frequencies of its normal modes. Finite element modelling (FEM) was used to simulate a more realistic system. A first set of prototype transducers was built and investigated. The prototype behaviour is in general agreement with the theoretical and FEM models, but with shifted modal frequencies. The prototype transducers have a strong mode at 140 kHz, which can be used to generate ultrasound in air.**

I. Introduction

A. Flexural Cap Transducers

Flexural transducers use the bending modes of a plate or membrane to displace the propagation medium and hence produce sound [1]. Since the plate vibrations are mechanically coupled to the medium, there is no impedance mismatch. A relatively small amount of input energy can generate large amplitude vibrations in the plate.

There are many different designs of flexure type transducers depending on their respective applications. Flexural transducers can be used as sensors [2] as well as for high power ultrasonics [3].

Fig. 1 shows a schematic diagram of the cross section of a piezoelectrically actuated metal cap flexural transducer. The piezoelectric disk inside the cap is bonded to the back of the plate. An electrical signal causes the piezoelectric element to expand, but it is constrained at the boundary to the plate, which causes the whole system to bend. The metal plate that produces the ultrasound waves is part of the cap, which also works as a protective buffer. The transducer therefore has an integrated ruggedness, which is valuable for many industrial applications.

The frequency of the vibrations and hence of the ultrasonic wave depend on the driving frequency of the electrical signal to the piezoelectric element. Large amplitude displacements

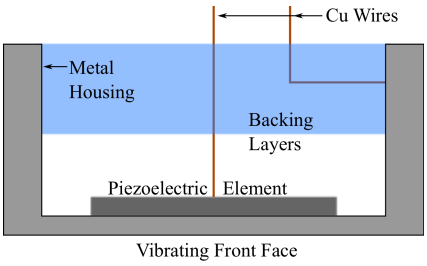

Fig. 1. Schematic diagram of a cross section of a piezoelectrically actuated flexure type transducer.

can be achieved by driving the system at resonance frequency. The resonance frequencies, i.e. the modal frequencies, of the system depend on the geometry and material of the cap, and are not related to the through thickness resonant frequencies of the piezoelectric element, which due to its small thickness are generally several orders of magnitude greater than the operational frequency of the flexural transducer.

B. Theory of Vibrating Plates

The equations describing the vibrations in circular, elliptical and rectangular plates with clamped, simply supported or free boundary conditions are derived in [4]. The general differential equation describing the transverse displacement of any thin plate regardless of shape and boundary conditions is

$$D\nabla^4 w(r,t) + \rho\frac{\partial^2 w(r,t)}{\partial t^2} = 0, \tag{1}$$

where D is the rigidity of the plate, defined in (2), w is the transverse displacement and ρ is the density. The rigidity is given by [4]

$$D = \frac{Eh^3}{12(1-\nu^2)}, \tag{2}$$

where E is Young's modulus, h is the plate thickness and ν the Poisson ratio. Solving 1 for a circular plate gives the following axisymmetric solutions

$$w(r,t) = [AJ_0(kr) + BI_0(kr)]\cos(\omega t), \tag{3}$$

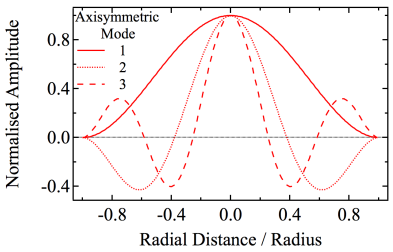

Fig. 2. Normalised amplitude of the first three axisymmetric modes of a plate clamped uniformly around the edge, from the spatial part of (3).

where $k^4 = \frac{\rho\omega^2}{D}$, J_0 and I_0 are the zeroth order Bessel function and modified Bessel function of the first kind respectively, and A and B are constant coefficients determined by the boundary conditions. The boundary conditions for a plate clamped uniformly around the edge ($r = a$) are

$$\begin{aligned} w(a,t) &= 0 \\ \left.\frac{\partial w(r,t)}{\partial r}\right|_a &= 0. \end{aligned} \tag{4}$$

Applying these boundary conditions to (3) gives the shapes of the normal modes, of which the three first harmonics are illustrated in fig. 2. These mode shapes are important for predicting the acoustic beam profile that a particular mode will produce. Prima facia, the second and third harmonic modes would produce greater side lobes compared to the fundamental mode.

The frequencies of the normal modes are given by

$$f = \frac{1}{2\pi}\left(\frac{\lambda}{a}\right)^2 \sqrt{\frac{D}{\rho h}}, \tag{5}$$

where $\lambda = ka$ is a root of (3). Remembering that D is proportional to the cube of the plate thickness, the frequency of any particular mode is inversely proportional to the radius squared and directly proportional to the thickness, for constant λ.

Two other boundary conditions of importance relate to completely free plates and simply supported plates, which are treated extensively in [4]. For the flexural transducer, described in §I-A and depicted in fig. 1, the actual boundary conditions are more complicated than any of the three mentioned. The edge of the plate is not rigidly fixed, yet its motion is impeded by the sides of the cap.

II. Methods

A. Computational Methods

Computational methods, using finite element modelling (FEM) [5], were applied to predict the properties and behaviour of the flexural transducer.

The FEM software package PZFlex was used to simulate the metal cap flexural transducer with different dimensions. Specifically, probes with plate thickness 0.1 mm $\leq h \leq$ 0.5 mm, and radii 1.9 mm $\leq a \leq$ 2.5 mm were simulated. The radius a does not include the side thickness of the probe, which for all simulations was set to 1.0 mm. The model was primarily used to look at the time varying displacement of the centre of the radiating face. By applying a short sinusoidal pulse to the piezoelectric element, the plate would vibrate at its natural frequencies, which could be found by a Fourier transform. A particular mode could then be investigated by driving the piezoelectric element with a continuous signal at the resonance frequency of that mode.

B. Experimental Methods

A first set of prototype flexure type transducer probes was made. Fig. 3 shows a 3D model of the transducer. The probe's metal cap was made from aluminium and its dimensions were:

Plate radius a = (4.5 ± 0.1) mm
Plate thickness h = (0.50 ± 0.05) mm
Side thickness = (1.0 ± 0.1) mm
Side length = (5.0 ± 0.1) mm

The piezoceramic disk had a (3.2 ± 0.1) mm radius and (0.50 ± 0.05) mm thickness. It was attached to the back of the plate, in the middle of the cap, with silver loaded epoxy.

A PolyTec laser vibrometer was used to measure the surface displacement of the radiating face of the probes. By recording the centre displacement of the probe for a short voltage pulse applied to the piezoelectric disk, the frequency spectrum was obtained by Fourier transform. By manually scanning the laser across a diameter of the probe in steps of 0.5 mm, the mode shape for a particular frequency could be determined.

The beam profile of a probe was measured with a microphone, moved in a 180° arc with the probe at its centre (see fig. 4). By varying the radius of the arc, both the near field and far field behaviour was observed. By moving the probe away from the microphone along a central line, from an initial small (<1 mm) separation, the near field amplitude variations were observed.

An impedance analyser was used to find the resonance frequencies of the flexural transducer prototypes. The phase of the impedance was used to give the frequency spectra of the transducers.

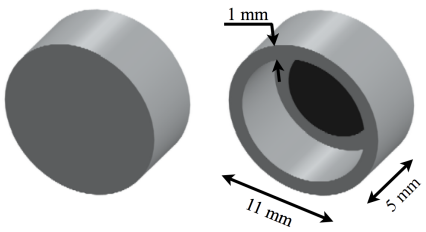

Fig. 3. 3D model, front and back view, of the piezoelectrically actuated aluminium cap flexural transducer prototype.

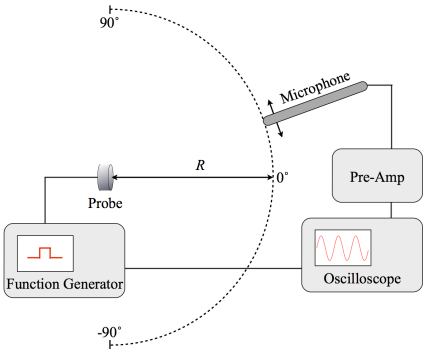

Fig. 4. Schematic diagram of the setup used to obtain the beam profile a distance R from the probe using an acoustic microphone.

III. Results

A. Flexural Transducer FEM Results

The frequency response of the fundamental mode for different radiating face radii and thicknesses is summarised in fig. 5. As predicted by plate theory, and in particular equation (5), the frequency of a specific mode increases with increasing thickness and decreases with increasing radius of the plate. However the relation between mode frequency and thickness is not linear.

Similar readings were taken for the second harmonic mode, but the results were more difficult to analyse due to mode splittings. However, some general results were obtained. For a plate with fixed radius of 2.0 mm a frequency shift from 269 kHz to 576 kHz was observed as the thickness was increased from 0.1 mm to 0.5 mm. For a fixed 0.5 mm thickness the frequency decreased from 576 kHz to 497 kHz as the radius was increased from 2.0 mm to 2.5 mm.

B. Results from Prototype Flexural Transducer Probe

Fig. 6 shows the frequency spectrum of a prototype probe with the dimensions specified in §II-B. The spectrum displays clearly separated frequency modes. The dominant mode of vibration was found at $\sim$ 140 kHz.

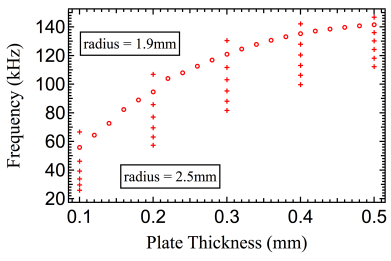

Fig. 5. Frequency of the first harmonic mode as a function of plate thickness for seven different plate radii going from 1.9 mm to 2.5 mm in steps of 0.1 mm.

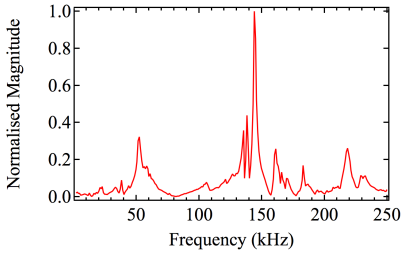

Fig. 6. Normalised magnitude frequency spectrum from FFT of centre displacement signal from a flexural transducer prototype, excited by a wideband pulse.

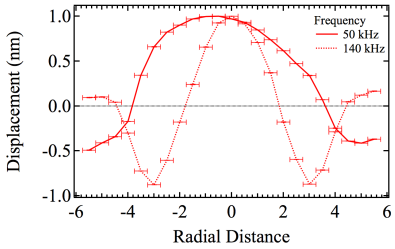

Fig. 7. Normalised peak-to-peak displacement of the first two resonant modes of the flexural transducer. The probe was excited by a continuous sinusoidal voltage of 1 V peak-to-peak. Negative values correspond to a $\frac{\pi}{2}$ phase shift in the displacement signal relative to readings with positive values.

Figs. 7 shows the mode shapes for the first and second frequency peaks at 50 kHz and 140 kHz respectively. The probe was driven with a continuous 1 V peak-to-peak sinusoidal signal at the resonance frequencies of the respective modes. There is reasonable agreement between these two mode shapes and the two first axisymmetric mode shapes predicted for a clamped plate (see fig. 2). The maximum displacement amplitude of the higher frequency mode was greater than that of the lower mode.

A FEM model with the dimensions of the prototypes was made for comparison. The frequency spectrum is shown in fig. 8. There is qualitative agreement between this spectrum and the spectrum in fig. 6, but the second harmonic mode appears shifted. In the FEM model the second harmonic mode had a resonance frequency close to 180 kHz, and the fundamental mode was found at 50 kHz.

C. Beam Profile of the Flexural Transducer

Fig. 9 shows the far field beam profile from a prototype transducer being driven at 140 kHz.

The air pressure amplitude decreases with separation from the ultrasound source due to attenuation, but in the near field there will be local amplitude maxima and minima. The end of the near field and beginning of the far field can be defined as the point of the last pressure maximum [6]. Fig. 10 shows the peak-to-peak pressure for a source to microphone separation

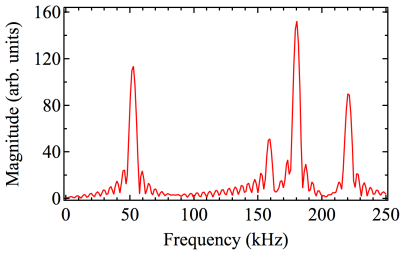

Fig. 8. FFT of centre displacement signal from FEM model of the flexural transducer.

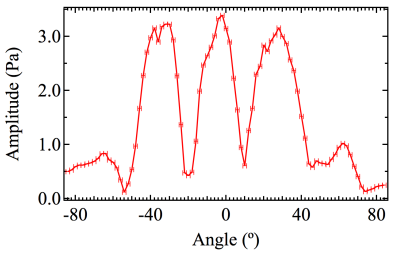

Fig. 9. Far field beam profile from a flexural transducer prototype operating in the second harmonic mode at 140 kHz.

of up to 9 mm. The peak separation should tend towards $\frac{\lambda}{2}$ as the separation between the transducer and the microphone decreases. The separation between the first two maxima is 1.23 mm, which gives $\lambda = 2.46$ mm. The frequency of sound equals the driving frequency of the transducer. This gives an estimation of the sound velocity in air $c = \lambda f = 342$ ms^{-1}, which is in good agreement with accepted values for sound in air at room temperature.

D. Impedance Analysis Results

The impedance phase of the prototype flexural transducer is shown in fig. 11. The peaks in the phase correspond well to the peaks in the Fourier spectrum obtained from measuring the displacement of the radiating face of the transducer (see fig. 6).

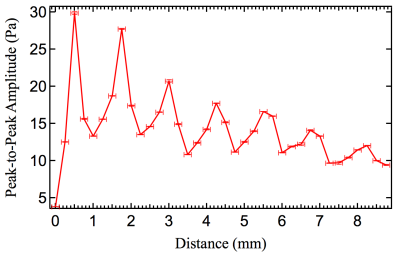

Fig. 10. Peak-to-peak amplitude variation with separation between source and microphone.

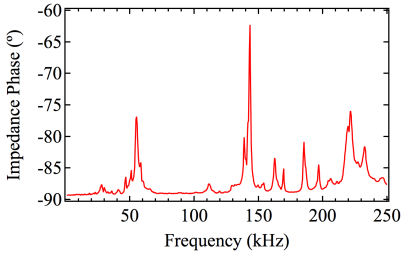

Fig. 11. Phase of the impedance of a prototype flexural transducer, showing good agreement with the frequency spectrum in fig. 6.

IV. Conclusion

Flexure type metal cap probes can effectively be used to generate ultrasound in air. The frequency of the sound produced depends on the geometry of the cap, and especially on the dimensions of the radiating face. A driving signal of a few volts peak-to-peak can produce large displacements on the order of 10^2 nm.

The FEM results showed, in agreement with the theory for clamped plate vibrations, that higher frequency transducer can be made by reducing the radius of the radiating face. A thicker plate also increases the frequency, but only to the limit where the cap starts to behave like a bulk transmitter instead of a flexing membrane.

References

[1] C.P. Germano. Flexure Mode Piezoelectric Transducers. *"IEEE Trans. Audio Electroacoust."*, AU19(1):6–12, 1971.

[2] W. Manthey, N. Kroemer, and V. Magor. Ultrasonic transducers and transducer arrays for applications in air. *Meas. Sci. Technol.*, 3:249–261, 1992.

[3] A. Barone and J.A. Gallegoj. Flexural vibrating free-edge plates with stepped thicknesses for generating high directional ultrasonic radiation. *J. Acoust. Soc. Am.*, 51(3):953–959, 1972.

[4] A.W. Leissa. *Vibration of Plates*. U.S. Government Press, Washington, 1969.

[5] W. Friedrich, H.T. Kaarmann, and R. Lerch. Finite element modeling of acoustic radiation from piezoelectric phased array antennas. In *IEEE 1990 Ultrasonics Symposium : Proceedings, Vols 1-3*, volume 2 of *Ultrasonics Symposium*, pages 763–767, New York, 1990. IEEE.

[6] G.L. Gooberman. *Ultrasonics: Theory and Application*. English University Press, London, 1968.

Metal Cap Flexural Transducers for Air-Coupled Ultrasonics

T.J.R. Eriksson[*,†], S. Dixon[*] and S.N. Ramadas[*]

[*]*Warwick University, UK*
[†]*t.j.r.eriksson@warwick.ac.uk*

Abstract. Ultrasonic generation and detection in fluids is inefficient due to the large difference in acoustic impedance between the piezoelectric element and the propagation medium, leading to large internal reflections and energy loss. One way of addressing the problem is to use a flexural transducer, which uses the bending modes in a thin plate or membrane. As the plate bends, it displaces the medium in front of it, hence producing sound waves. A piezoelectric flexural transducer can generate large amplitude displacements in fluid media for relatively low excitation voltages.

Commercially available flexural transducers for air applications operate at 40 kHz, but there exists ultrasound applications that require significantly higher frequencies, e.g. flow measurements. Relatively little work has been done to date to understand the underlying physics of the flexural transducer, and hence how to design it to have specific properties suitable for particular applications.

This paper investigates the potential of the flexural transducer and its operating principles. Two types of actuation methods are considerd: piezoelectric and electrodynamic. The piezoelectrically actuated transducer is more energy efficient and intrinsically safe, but the electrodynamic transducer has the advantage of being less sensitive to high temperature environments. The theory of vibrating plates is used to predict transducer frequency in addition to front face amplitude, which shows good correlation with experimental results.

INTRODUCTION

Flexural Cap Transducers

Flexural transducers use the bending modes of a plate or membrane to displace the propagation medium and hence produce sound waves [1]. Since the plate vibrations are mechanically coupled to the medium, there is no acoustic impedance mismatch. A relatively small amount of input energy can generate large amplitude vibrations in the plate.

There are many different designs of flexural transducers depending on their respective applications. Flexural transducers can be used as sensors [2] as well as for high power ultrasonics [3]. Flexural transducers are commercially available, and the technology is well established, being used in ultrasonic parking sensors.

Fig. 1 shows a schematic diagram of the cross section of a metal cap piezoelectric flexural transducer. When an electric field is applied across the piezoelectric element it will try to expand, but because it is constrained at the boundary to the metal cap, it will cause the system to bend instead.

The active element in fig. 1 can be replaced by a spiral coil of wire. The current in the coil induces a magnetic field $\overrightarrow{B}$ in the front plate of the metal cap, which generates a current density $\overrightarrow{j}$. The current in the cap interacts with the magnetic field to produce a Lorentz force $\overrightarrow{F} = \overrightarrow{j} \times \overrightarrow{B}$ [4], which sets the plate in vibration. The metal cap is therefore a necessary part for ultrasonic generation whilst also providing an integrated ruggedness, which is valuable for many industrial applications. The generation method is similar the one used for electromagnetic acoustic transducers (EMATS)[5], but without the static magnetic field. A static magnetic field can however be introduced, and is necessary for receiving ultrasound.

Large amplitude displacements can be achieved by driving the system at resonance frequency. The resonance frequencies, i.e. the modal frequencies, of the system depend on the geometry and material of the cap.

Theory of Vibrating Plates

The general equation describing the transverse displacement of a thin plate is [6]

$$D\nabla^4 w(\overrightarrow{x},t) + \rho h \frac{\partial^2 w(\overrightarrow{x},t)}{\partial t^2} = 0, \tag{1}$$

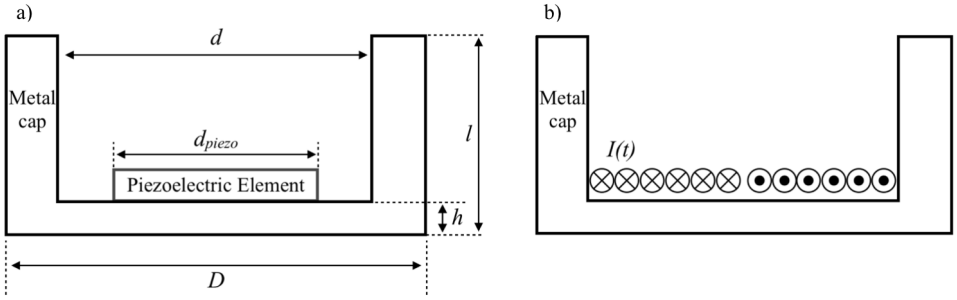

FIGURE 1. Schematic diagrams of the cross section of two metal cap flexural transducers, which use a) a piezoelectric element and b) a current carrying spiral coil for excitation. The thickness of the piezoelectric element should be of similar size or smaller than the front face, to allow for flexing. For the same reasons, d_{piezo} should be significantly larger than the thickness of the piezoelectric element.

where D is the rigidity of the plate, defined in (2), w is the transverse displacement, ρ is the volume density, and h is the plate thickness. The rigidity is given by

$$D = \frac{Eh^3}{12(1-\nu^2)}, \tag{2}$$

where E is Young's modulus and ν the Poisson ratio. For a full solution of (1) for an edge clamped circular plate see [6].

The frequencies of the normal modes are given by

$$f = \frac{1}{2\pi}\left(\frac{\lambda}{a}\right)^2 \sqrt{\frac{D}{\rho h}}, \tag{3}$$

where $\lambda = ka$ is a root of the solution to (1). Remembering that D is proportional to the cube of the plate thickness, the frequency of any particular mode is inversely proportional to the radius squared and directly proportional to the thickness, for a given eigenvalue λ.

Solving (1) with the appropriate boundary conditions gives the shapes of the vibration modes. The modes are labeled (m,n), where m is the number of nodal radii and n the number of nodal diameters of the mode. The boundary conditions for an edge clamped plate are not strictly applicable to the flexural transducer illustrated in fig. 1. The sides of the cap will restrict the motion along the edge of the vibrating plate, but not completely stop it. However, the edge clamped plate is a good approximation, which gives useful insight into the behaviour of the flexural transducer.

METHODS

The finite element method (FEM) [7], was used to predict the properties and behaviour of the flexural transducer. The FEM software package PZFlex was used to simulate the metal cap flexural transducer, when excited by a piezoelectric element or by a time varying pressure load. Using a pressure load resembles the electrodynamic generation to some extent, since it is a form of non-contact generation. By applying a broadband excitation pulse, the plate would vibrate at its natural frequencies, which could be found by Fourier transform. A particular mode could then be investigated by driving the transducer with a continuous signal at the resonance frequency of that mode.

A PolyTec laser vibrometer was used to measure the surface displacement of the radiating face of the transducers. The system was set up to scan the whole front face in steps of 0.3 mm, in order to determine both mode shape and frequency. A schematic diagram of the setup is shown in fig. 2. Different transducers were used for piezoelectric and electrodynamic generation, since there was no easy way to switch between the two generations methods in a single metal cap.

The dimensions of the cap in the FEM model and the prototypes were: Inner diameter $d = 9.0$ mm, outer diameter $D = 11.0$ mm, front face thickness $h = 0.5$ mm.

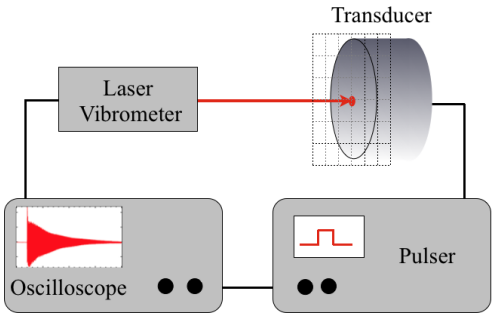

FIGURE 2. Schematic diagram of setup used to scan the front face of the transducer. When using a piezoelectric element to generate, an arbitrary function generator was used as pulser, and for electrodynamic generation an EMAT pulser was used.

RESULTS

Flexural Transducer FEM Results

The frequency spectrum of the FEM modelled flexural transducer is presented in fig. 3. The spectrum was obtained from the Fourier transform of the displacement signal from the front face of the metal cap, when excited by a broadband pulse, using electrodynamic generation. The displacement was measured at a point slightly off-centre, in order to capture the frequency peaks corresponding to non-axisymmetric modes, i.e. modes with one or more nodal diameters $(m,n>0)$.

The first peak in the spectrum corresponds to the fundamental mode (0,0), and is located at 50 kHz. The calculated values from (3) for this mode are 42 kHz and 62 kHz, using the outer and the inner radius for a respectively. The second peak at 100 kHz corresponds to the first non-axisymmetric mode (0,1). The (1,0) mode is split into three peaks at 160 kHz, 180 kHz and 220 kHz. The peak at 390 kHz represents the third axisymmetric mode (2,0). The other peaks can similarly be associated with the theoretical vibration modes, by looking at the mode shape of the transducer at the location of the peak.

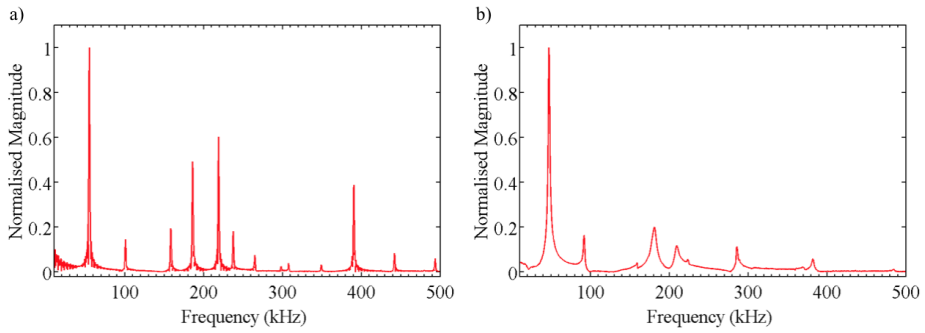

FIGURE 3. Normalised frequency spectra from a) FEM model and b) experimentally measured displacement signal from prototype electrodynamic flexural transducer

Results from Prototype Flexural Transducer

Figure 3 shows the frequency spectra of a prototype transducer with the dimensions specified in the methods section.

The locations of the mode frequencies are in good agreement with the FEM results, even though the relative amplitudes of the peaks do not agree. The amplitudes however depend on the specific generation method as well as the position on the front face of the transducer where the displacement signal was recorded. It is encouraging to see the three way splitting of the (1,0) mode, that was also observed in the FEM model results.

Figure 4 shows the measured (1,0) and (2,0) mode shapes and their theoretical counterparts. The measured frequencies of these modes are180 kHz and 390 kHz respectively. The other modes present in the frequency spectrum (see fig. 3) show similar correspondence between experimental and theoretical mode shapes. In general there is good agreement between the experimentally measured results and the theoretically calculated results.

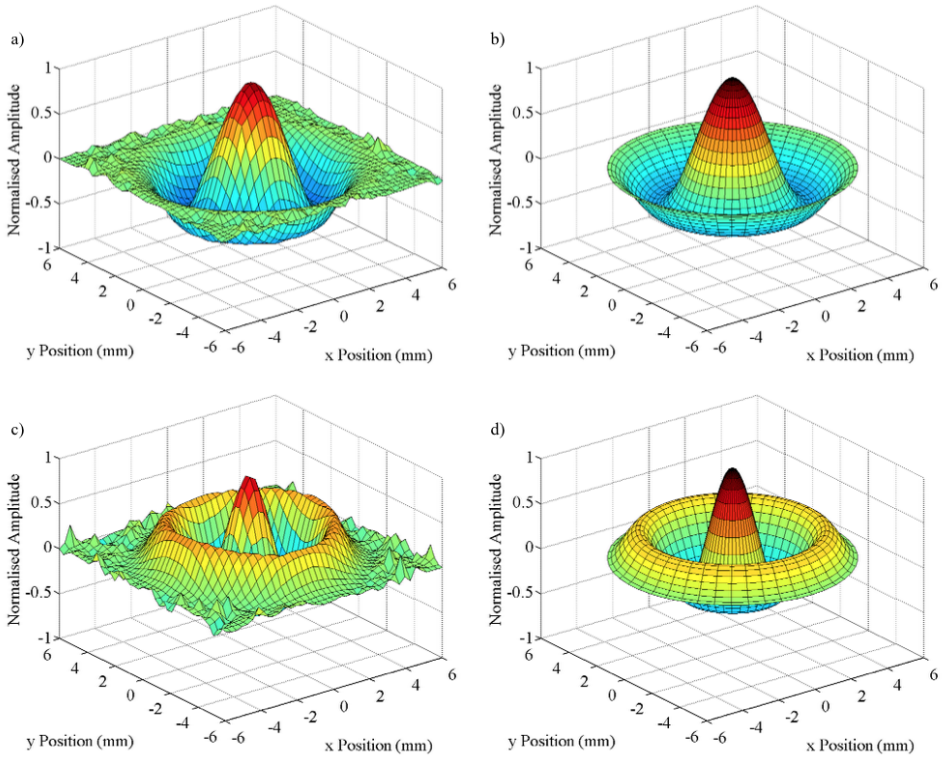

FIGURE 4. a) Experimental mode (1,0) at 180 kHz, b) theoretical shape of mode (1,0), c) experimental shape of mode (2,0) at 390 kHz, and d) theoretical shape of mode(2,0).

CONCLUSION

The metal cap flexural transducers can be designed to operate at specific frequencies with specific vibration modes. They show potential as an alternative ultrasound generation method in air and liquids.

Metal cap flexural transducers show good agreement with the analytical theory of edge clamped circular plates. The theory can therefore be used to quickly predict the frequency and vibration mode shape of a transducer of known dimensions. The transducer has an inner and outer diameter values, which can both be used in the theory to give an upper and lower bound on any mode frequency. The frequency band between the bounds grows larger for higher modes, making them harder to predict accurately using an analytical solution. For the fundamental mode a lower bound of 42 kHz and and upper bound of 62 kHz were calculated for the particular flexural cap model. The measured fundamental mode was found in between these values at 50 kHz.

10.1109/ULTSYM.2014.0250

Air-Coupled Flexural Electrodynamic Acoustic Transducers

T.J.R. Eriksson, M. Laws, S.M. Dixon and S.N. Ramadas
University of Warwick, UK
Email: t.j.r.eriksson@warwick.ac.uk

***Abstract*—Flexural transducers use the bending modes in a plate or membrane to produce sound in low acoustic impedance media. Traditionally, piezoelectrically actuated flexural transducers have been used to generate ultrasound with large amplitude for a relatively low excitation voltage. In this work, the use of electrodynamic forces generated by a current carrying coil is investigated, as an alternative method for generating ultrasound by flexural vibrations. Using a coil instead of a piezoelectric element makes the transducer easier to manufacture, and able to operate at high temperatures. The analytical theory of vibrating plates as well as finite element modelling was used to predict transducer behaviour, i.e. mode frequencies and shapes of the vibrating front face. Prototype transducers were made from aluminium with a pancake copper coil at the back for generation. A Polytec laser vibrometer was used to measure the front face displacement of these prototype transducers. The displacement measurements revealed a frequency spectrum with narrowband (∼3 kHz full width half maximum) modal frequency peaks, and a dominant fundamental mode at ∼50 kHz. The spectrum is in good agreement with calculated frequency values, and the experimental mode shapes are similar to those predicted by theory.**

I. Introduction

A. Flexural Cap Transducers

Flexural transducers use the bending modes of a plate or membrane to displace the propagation medium and hence produce sound [1]. Since the plate vibrations are mechanically coupled to the medium, there is no acoustic impedance mismatch. A relatively small amount of input energy can generate large amplitude vibrations in the plate. There are many different designs of flexure type transducers depending on their respective applications. Flexural transducers can be used as sensors [2] as well as for high power ultrasonics [3].

Fig. 1 shows a schematic diagram of the cross section of a metal cap flexural (EDAT). The current in the coil induces a magnetic field $\overrightarrow{B}$ in the front plate of the metal cap, which generates a current density $\overrightarrow{j}$. The current in the cap interacts with the magnetic field to produce a Lorentz force $\overrightarrow{F} = \overrightarrow{j} \times \overrightarrow{B}$[4], which sets the plate in vibration. The metal cap is therefore a necessary part for ultrasonic generation whilst also providing an integrated ruggedness, which is valuable for many industrial applications.

Large amplitude displacements can be achieved by driving the system at resonance frequency. The resonance frequencies, i.e. the modal frequencies, of the system depend mainly on the geometry and material of the cap.

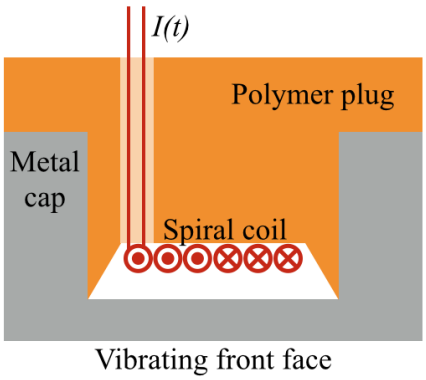

Fig. 1: Schematic diagram of a cross section of a metal cap flexural electrodynamic acoustic transducer.

B. Theory of Vibrating Plates

The flexural transducer, because of its thin front face and semi-rigid sides, can be approximated by an edge clamped plate. The general equation describing the transverse displacement of a thin plate is [5]

$$D\nabla^4 w(\overrightarrow{x},t) + \rho h \frac{\partial^2 w(\overrightarrow{x},t)}{\partial t^2} = 0, \quad (1)$$

where D is the rigidity of the plate, defined in (2), w is the transverse displacement and ρ is the volume density. The rigidity is given by [5]

$$D = \frac{Eh^3}{12(1-\nu^2)}, \quad (2)$$

where E is Young's modulus, h is the plate thickness and ν the Poisson ratio. Solving (1) for a circular plate gives the following solutions

$$w(r,\theta,t) = [AJ_n(kr) + BI_n(kr)]\cos(n\theta)\cos(\omega t), \quad (3)$$

where $k^4 = \frac{\rho\omega^2}{D}$, J_n and I_n are the Bessel function and modified Bessel function of the first kind respectively, and A and B are coefficients determined by the boundary conditions. The boundary conditions for a plate clamped uniformly around

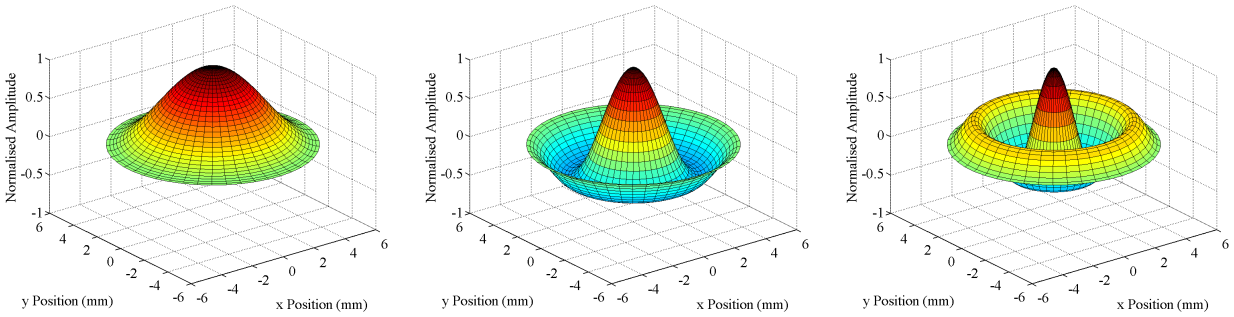

(a) Fundamental mode (0,0) (b) Second axisymmetric mode (1,0) (c) Third axisymmetric mode (2,0)

Fig. 2: First three axisymmetric theoretical mode shapes of an edge clamped circular plate.

the edge ($r = a$) are

$$w(a,t) = 0 \qquad \left.\frac{\partial w(r,\theta,t)}{\partial r}\right|_a = 0. \tag{4}$$

Applying these boundary conditions to (3) gives the shapes of the vibration modes, of which the three first axisymmetric harmonics are illustrated in fig. 2. The dimensions of the plate were chosen to match those of the prototype transducer that was later made and tested.

The frequencies of the normal modes are given by

$$f = \frac{1}{2\pi}\left(\frac{\lambda}{a}\right)^2 \sqrt{\frac{D}{\rho h}}, \tag{5}$$

where $\lambda = ka$ is a root of (3). Remembering that D is proportional to the cube of the plate thickness, the frequency of any particular mode is inversely proportional to the radius squared and directly proportional to the thickness, for a given eigenvalue λ.

The boundary conditions in (4) are not strictly applicable to the flexural transducer illustrated in fig. 1. The edges of the cap will restrict the motion along the edge, but not completely stop it. However, the edge clamped plate is a good approximation, which gives useful insight into the behaviour of the flexural transducer.

C. Annular Caps

An alternate geometry, which may be useful for flexural transducers, is that of an annular plate, a plate with a hole in the centre. Such a geometry could allow the development of annular flexural transducer arrays or allow other types of sensor, for example a temperature or pressure sensors, to be incorporated into the transducer.

The theory which may be used to describe such an annular plate is very similar to that used for circular, modified to include additional boundary conditions for the inner radius, b. For the simplest case, uniformly clamped on both the inner and outer edge, the boundary conditions are the same as those given in (4) but for both $r = a$, the outer radius, and $r = b$, the inner radius. The resulting solutions are dependent only on the thickness of the plate, h, and the ratio of inner and outer radii, b/a. A schematic diagram of an annular flexural EDAT is shown in fig. 3.

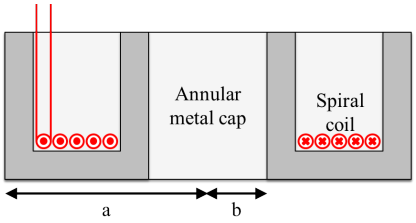

Fig. 3: Schematic diagram of a cross section of an annular metal cap flexural electrodynamic acoustic transducer.

II. Methods

Computational methods, using finite element modelling (FEM) [6], were applied to predict the properties and behaviour of the flexural transducer.

The FEM software package PZFlex was used to simulate the metal cap flexural transducer when excited by a time varying pressure load. By applying a broadband excitation force, the plate would vibrate at its natural frequencies, which could be found by a Fourier transform of the front face displacement data. A particular mode could then be investigated by driving the piezoelectric element with a continuous signal at the specific resonance frequency of that mode.

A Polytec laser vibrometer was used to measure the surface displacement of the radiating face of the transducers, when they were excited by an EMAT pulser. The system was set up to scan the whole front face in steps of 0.3 mm, in order to determine both mode shape and frequency.

The dimensions of the cap in the model and the of prototypes were: inner radius = 4.5 mm, outer radius = 5.5 mm,

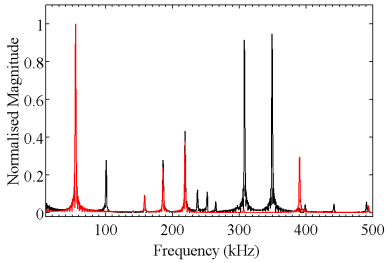

Fig. 4: Normalised magnitude frequency spectra from FFT of the centre (red) and off-centre (black) displacement signals, from the FEM transducer model.

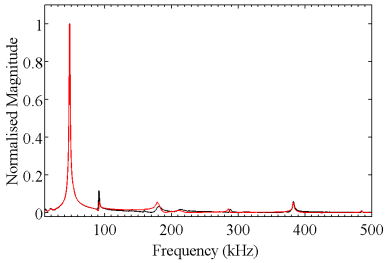

Fig. 5: Normalised magnitude frequency spectra from FFT of centre (red) and off-centre (black) displacement signals from a flexural transducer prototype, excited by a wideband pulse.

front face thickness = 0.5 mm, and the length of the side of the cap = 5.0 mm.

Additionally, an annular cap with an internal radius of 7 mm, external radius of 17 mm, front face thickness on 0.5 mm, and side length of 10.0 mm prototype was manufactured ans studied together with the simple circular cap design.

III. Results

A. Flexural Transducer FEM Results

The frequency spectra from two different points on the vibrating front face are shown in fig. 4. The spectrum obtained from the displacement signal from the centre of the transducer doesn't show the non-axisymmetric mode frequency peaks, since they have at least one nodal diameter going through the centre, a line through the centre of the plate with zero displacement. These modes are revealed in the second spectrum, which is obtained from a displacement measurement away from the centre of the disc.

The first peak in the spectrum corresponds to the fundamental mode (0,0), and is located at 50 kHz. The calculated values from (5) for this mode are 42 kHz and 62 kHz, using the outer and the inner radius for a respectively. The second peak at 100 kHz corresponds to the first non-axisymmetric mode (0,1). The (1,0) mode is split into three peaks at 160 kHz, 180 kHz and 220 kHz. The peak at 390 kHz represents the third axisymmetric mode (2,0). The other peaks can similarly be associated with the theoretical vibration modes, by looking at the mode shape of the transducer at the location of the peak.

B. Results from Prototype Flexural Transducers

Fig. 5 shows the frequency spectra of a prototype transducer with the dimensions specified in §II. Similar to the spectra from FEM the displacement signals from two points on the transducer face were Fourier transformed to obtain the frequency spectra.

The locations of the mode frequencies are in good agreement with the FEM results, even though the relative amplitudes of the peaks do not agree. The amplitudes however depend on the specific generation method as well as the position on the front face of the transducer where the displacement signal was recorded. It is encouraging to see the three way splitting of the (1,0) mode, that was observed in the FEM model results (see fig. 4).

TABLE I: Analytically Calculated (0,0) Modes

Internal Radius (mm)	External Radius (mm)	Frequency of (0,0) Mode (kHz)
17.0	6.5	26.3
16.5	6.5	27.3
17.0	7.0	29.0
16.5	7.0	30.3

Fig. 6 shows the three first axisymmetric modes, achieved by frequency filtering the displacement signal from the flexural EDAT. The frequencies of these modes are 50 kHz, 180 kHz and 390 kHz, respectively.

Fig. 7 shows both the analytically calculated and experimentally measured (0,0) mode, for the annular cap described previously. Similar to the circular cap, there are several sets of radii which must be considered when attempting to calculate frequency at which a cap would be expected to resonate, due to the thickness of the sides of the cap. As such, four pairs of radii must be considered, each giving slightly different resonant frequencies, given in Table I.

The experimentally measured (0,0) mode was found to have a frequency of 28.4 kHz, approximately in the centre of the values given in Table I, similar to what was found for the case of a circular cap.

IV. Conclusion

The flexural EDAT provides an alternative method of ultrasound generation, using the induced self interacting magnetic field of a current carrying spiral coil, to actuate the flexing front face of the transducer. A greater amount of energy is needed for generation, but the flexural EDAT has the potential of operating at higher temperatures than the piezoelectrically

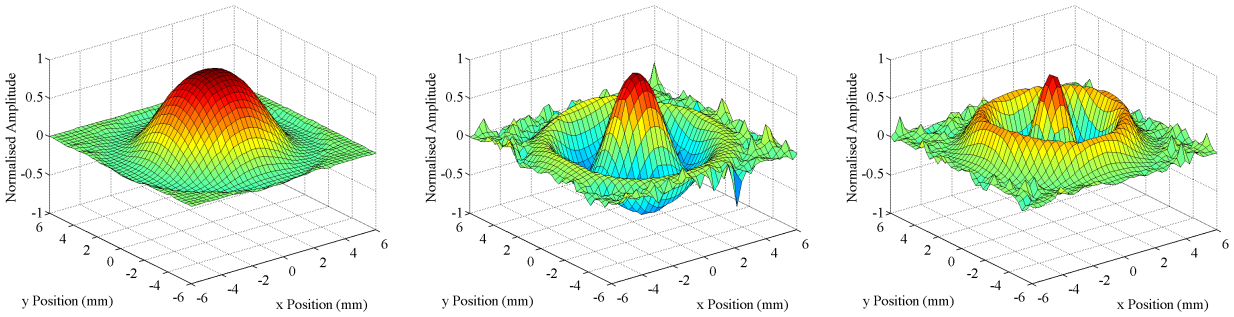

(a) Fundamental mode (0,0) at 50 kHz (b) Second axisymmetric mode (1,0) at 180 kHz (c) Third axisymmetric mode (2,0) at 390 kHz

Fig. 6: Normalised displacement amplitude of the first three axisymmetric modes of the flexural transducer at a) 50 kHz, b) 180 kHz and c) 390 kHz.

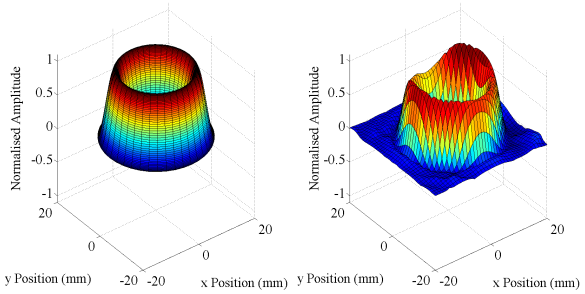

Fig. 7: (left) Analytically calculated, (0,0) mode shape for the annular cap at 27.3 kHz. (right) Experimentally measured (0,0) mode at 28.4 kHz.

actuated transducer. Also, by not having a piezoelectric element the manufacturing process is simplified, and there is no problem of the active element debonding over time.

The initial results from the prototype transducers show good agreement with both the theoretically predicted behaviour of an edge clamped circular plate, as well as the results from the FEM. When calculating the mode frequency, using (5), the radius can be set to $a =$ outer radius or $a =$ inner radius of the transducer, giving a lower and upper frequency limit, respectively. The measured mode frequencies were all located within these limits, which allows us to use the theory to quickly predict resonances of a transducer. It has also been shown that similar analytical modelling allows the resonant frequencies of annular caps to be predicted accurately.

Using a pancake coil and standard EMAT pulser for generation causes the transducer to vibrate mainly in the fundamental mode. Using other coil configurations and pulse shapes could allow for mode selectivity. The ultrasonic signal is very narrowband, due to the ringing of the cap, but could potential be broadened by use of electronic and physical damping.

REFERENCES

[1] C.P. Germano. Flexure Mode Piezoelectric Transducers. *"IEEE Trans. Audio Electroacoust."*, AU19(1):6–12, 1971.

[2] W. Manthey, N. Kroemer, and V. Magor. Ultrasonic transducers and transducer arrays for applications in air. *Meas. Sci. Technol.*, 3:249–261, 1992.

[3] A. Barone and J.A. Gallegoj. Flexural vibrating free-edge plates with stepped thicknesses for generating high directional ultrasonic radiation. *J. Acoust. Soc. Am.*, 51(3):953–959, 1972.

[4] J. Griffiths. *Introduction to Electrodynamics*. Prentice-Hall International, London, 3rd edition, 1999.

[5] A.W. Leissa. *Vibration of Plates*. U.S. Government Press, Washington, 1969.

[6] W. Friedrich, H.T. Kaarmann, and R. Lerch. Finite element modeling of acoustic radiation from piezoelectric phased array antennas. In *IEEE 1990 Ultrasonics Symposium : Proceedings, Vols 1-3*, volume 2 of *Ultrasonics Symposium*, pages 763–767, New York, 1990. IEEE.

10.1109/ULTSYM.2015.0047

Flexural Transducer Arrays for Industrial Non-Contact Applications

T.J.R. Eriksson*, S.N. Ramadas*†, A. Unger‡, M. Hoffman††, M. Kupnik‡ and S.M. Dixon*
*University of Warwick, UK
†Elster NV/SA, Belgium
‡ Technische Universität Darmstadt, Germany
†† BTU Cottbus-Senftenberg, Germany
Email: t.j.r.eriksson@warwick.ac.uk

***Abstract*—A new method of constructing robust air-coupled flexural ultrasound arrays is suggested, and results from a prototype transducer are presented. The flexural elements are defined on a single sheet of metal by bonding a baffle structure to the back of the sheet. Piezoelectric elements were attached directly to the metal plate in the centre of the holes in the baffle. The aim was to find if the baffle could sufficiently separate the elements, such that each element behaved like a flexural transducer with radius equal to the radius of the holes in the baffle. By measuring the front face displacement of the array the vibration mode of individual elements could be characterised and compared to those of a single element transducer. In general the baffle sufficiently separated the flexural elements, such that the vibration modes observed corresponded to those of an edge clamped plate with a radius 1.5 mm larger than that of the holes in the baffle. This is a small shift, which is explained by the outer boundary being less well defined for the array elements, compared to a single element flexural transducer.**

I. Introduction

Flexural transducers use the bending modes in a thin plate to generate and receive ultrasound in low impedance media. A typical flexural transducer will have a thin piezoelectric disc rigidly bonded to a thin metal plate, or the inside of a cap. When the piezoelectric element is excited it expands, but because it is constrained along the surface in contact with the metal plate the system becomes stressed and deforms. It is this deflection of the metal plate that pushes the loading medium, and hence generates sound. The effective impedance is much lower than the acoustic impedance of the metal material itself, which allows the system to efficiently couple to lower impedance media. This also allows the transducer to be operated at lower voltages, which is important in many real-world applications.

Previous work on single element flexural transducers [1] have looked at mode shapes and frequencies, as a function of plate geometry. Although traditionally the fundamental vibration mode is used for ultrasonic transduction (excluding high power ultrasonics), it was shown that higher axisymmetric modes could be used to transmit higher frequency signals. The denotation of vibration modes in this paper was adopted from [2], where (m, n) denotes a mode with m nodal radii (excluding the edge) and n nodal diameters, as illustrated in Fig. 1. The fundamental mode is hence $(0, 0)$, with a mode frequency $f = f_{0,0}$. The flexural transducers can be modelled with a good level of accuracy using thin plate theory [2]. The front face of the transducer is then assumed to behave like a thin, circular, edge clamped plate. From the theory both mode shapes and mode frequencies can be predicted. Though this gives a good starting point for transducer design, more accurate model results are generally obtained from finite element (FE) methods.

Air-coupled ultrasonics has gained interest over the years as more non-contact applications are discovered. For example, inspection of composite materials has motivated the development of air-coupled transducers. The development of micromachined ultrasonic transducers such as CMUTs [3] and PMUTs [4] has also driven the recent development of air-coupled phased array technology [5]. Both CMUTs and PMUTs have been used effectively for phased array ultrasonics, and the transducer design outlined in this paper could represent an industrially robust, macroscopic alternative to these technologies. A similar design for a non-phased array, immersion transducer has recently been presented in [6].

II. Design

A small number of elements, 3x3, was chosen for the first array prototype, as it was made as a proof of concept. The element dimensions, $d = 10.4$ mm and $h = 0.25$ mm, were chosen to correspond to those of a single element transducer previously investigated [1], with a vibration mode around 100 kHz that can be used for transduction. Hence, previous results from the single transducer could be used for comparison, to evaluate if the individual array elements were sufficiently separated.

Unlike the single element flexural transducer, which used a titanium plate, the array was made using a stainless steel sheet. Stainless steel, like titanium, is corrosion resistant and

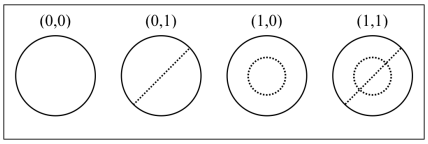

Fig. 1: The four first vibration modes of a circular plate, with dashed lines denoting nodes.

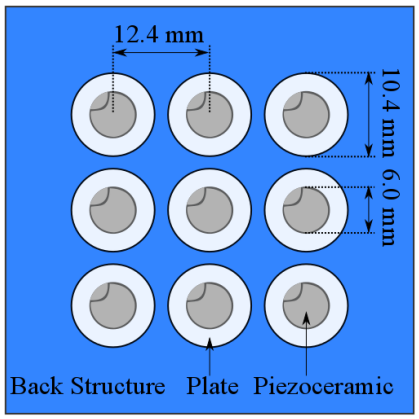

(a)

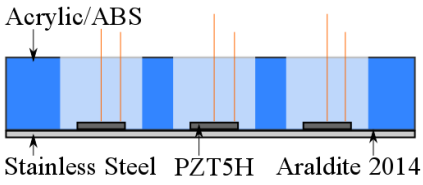

(b)

Fig. 2: a) Bottom view schematic diagram of flexural array with dimensions. b) Crossectional sideview schematic diagram of flexural array transducer with labeled materials.

in general a suitable material for industrial applications. It has greater rigidity than titanium, which does reduce the transduction efficiency, but the overall behaviour is not significantly different between the two. For example an edge clamped, circular plate with the dimensions listed above has a fundamental frequency of $f_{0,0} = 23.2$ kHz for titanium and $f_{0,0} = 22.3$ kHz for stainless steel.

A baffle was bonded to the stainless steel sheet. The radius of the holes in the baffle define the radius of the array elements. For the first prototype a 3 mm thick acrylic plate, with laser cut holes, was used. In later versions a 3D printed ABS plastic back plate was used. Both methods of defining the flexural elements provide flexibility in terms of dimensions and layout.

Piezoelectric discs made of PZT5H from PI Germany, with a 0.25 mm thickness were used as the electromechanically active layer of the transducer elements. FE modelling, using PZFlex (Weidlinger Associates Inc., USA) software package, was used to find the optimal radius of the piezoelectric element. The model consisted of an axisymmetric flexural cap transducer operating in air, excited with a fixed voltage pulse for varying piezo radii. Fig. 3 shows the maximum central displacement as a function of the piezoelectric disc radius for mode (1,0). From the model it was found that the optimal radius of the piezoelectric disc for generating ultrasound using the (1,0) vibration mode was $r \simeq 3$ mm, which roughly corresponds to the radius of the second antinode. In general the electromechanical coupling as a function of piezo coverage depends on the specific mode used for transduction.

In order to avoid using conductive epoxy to bond the piezoelectric discs to the plate, which has previously been found to give insufficient adhesion, piezos with wrap around electrodes were used. Hence, each element had two electrical connections, with ground on the bonded side.

The main benefits of the proposed design is its inherent robustness, gained from having a single piece of metal in contact with the loading medium, and the ease of manufacturing that is a result of not having to build the flexural elements individually before assembling them into an array.

III. Construction Process

The baffle was designed using the CAD software SolidWorks. The first version of the baffle, for which the results are reported in this paper, was laser cut out of a transparent acrylic sheet. Later versions of the baffle were printed using a commercial, layer-by-layer, 3D printer in ABS plastic. The baffle was bonded to a stainless steel plate using Araldite-2014 two component epoxy. Both the plate and the baffle were cleaned with a degreasing agent before bonding. A second 3D structure, designed to hold the piezoelectric elements, that fitted inside the baffle was printed. The piezodiscs were placed in this structure. A thin layer of Araldite-2014 was placed on the ground electrodes. The baffle with the metal plate was fitted onto the structure with the piezodiscs, such that the grounded side of the elements were pushed against the inside of the steel plate. The epoxy was cured under pressure at room temperature. Electric leads were soldered to each element and connected to individual coaxial cables with BNC connectors. The finished array is schematically shown in Fig. 2, and a picture is shown in Fig. 4.

IV. Methods

A Polytec laser vibrometer was used to measure the out of plane displacement of the array elements. The transducer was placed on a computer controlled xy stage to scan the whole front face displacement. By saving the time data for

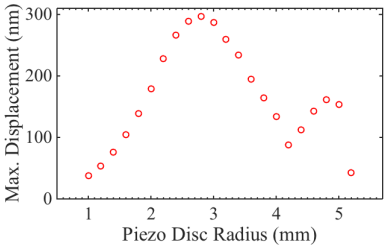

Fig. 3: Max. centre displacement from FE model of axisymmetric single element flexural transducer, plotted against radius of the piezoelectric disc.

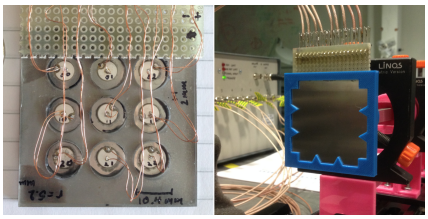

Fig. 4: Back and front view of the finished array with the laser cut acrylic baffle on the back.

each point the dynamics of the vibrations could be analysed on a fundamental level.

A broadband acoustic microphone (BK 4138-A-015) was used to measure the absolute pressure output from the transducer. The pressure along the central line perpendicular to the transducer front face was measured when each individual element was driven separately and when groups of elements were excited together.

V. Results

The result reported below are from a prototype transducer array with a laser cut acrylic baffle, but tests using 3D printed ABS for the baffle have indicated no large difference in performance. Fig. 5 shows the maximum displacement of the array as the central element was excited. The element was excited by a 3 cycle sinusoidal signal at 100 kHz and 5 Vpp. From the surface plot it is seen that the displacement is mostly constrained to the area defined by the baffle, and that the vibration mode is (1,0). There was significant cross talk, with displacement amplitudes of neighbouring, inactive elements reaching -12 dB. Fig. 6 shows the displacement at the centre of three elements, when one of them is being driven.

Fig. 7 shows the maximum displacement plotted against radius for the central element in the array, as well as for a single element flexural transducer for comparison. It is seen that the apparent element size of the array element is larger, with a radius approximately 1.5 mm greater, than the single element transducer. The displacement amplitude of the single

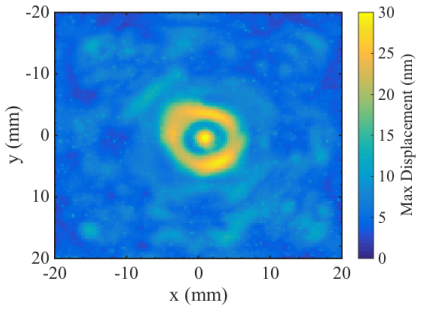

Fig. 5: Max. front face displacement of flexural array transducer when the centre element is excited.

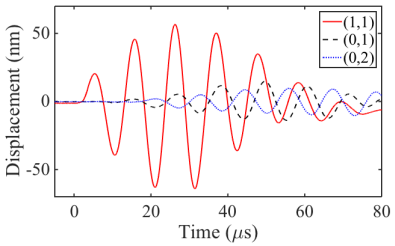

Fig. 6: Centre displacement signal from three elements, when one element (1,1) is excited, showing the level of mechanical crosstalk.

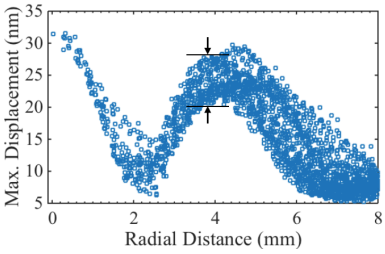

(a)

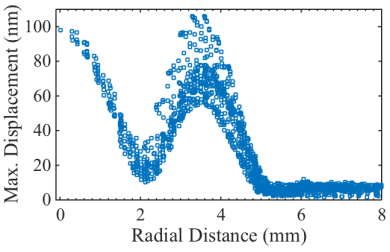

(b)

Fig. 7: Max. displacement plotted as a function of the distance from the centre of the element, for a) the centre element of the array, and b) a single element flexural transducer with an inner radius of 5.2 mm.

element transducer is greater than that of the array, which is due to the single element transducer having a titanium plate instead of a stainless steel plate. The vertical width of the distribution, indicated in Fig. 7a at an arbitrary point, reflects how axisymmetric the vibrations are. For a pure axisymmetric vibration mode the distribution would follow a single line with zero width.

Fig. 8 shows the maximum displacement of the array, when all elements are driven in phase. The excitation pulse is a three cycle tone burst, centred around 100 kHz. In order not to saturate the laser vibrometer, which happens around 150 nm, the power output from the phased array pulser system was set to 0.5%. The results indicate that there is good consistency between most of the elements. From Fig. 8 it is seen how the

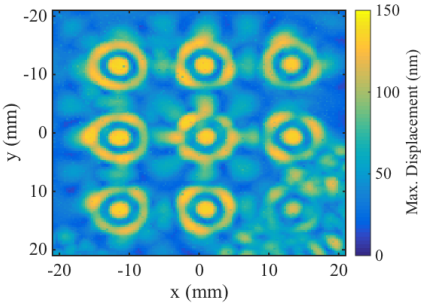

Fig. 8: Max. front face displacement of flexural array transducer when all elements are excited simultaneously.

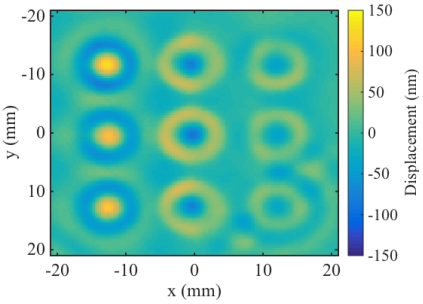

Fig. 10: Instantaneous front face displacement of the flexural array when phased to produce a 5 degree steering angle.

element in the lower right corner is less well defined than the others, and surrounded by high displacement peaks that are not part of the (1,0) vibration mode. This is due to locally weak bonding between the baffle and the steel plate. The high displacement peaks around this element are associated with areas with trapped air in the bond layer. Hence it can be concluded that bond strength and consistency are important for the performance of the individual elements and of the array as a whole.

Fig. 9 shows the absolute pressure from an array, with one element being excited and a row of three elements excited respectively. The pressure was measured a distance of 24 cm from the centre of the array. The transducer was driven with a 3 cycle sinusoidal, 100 kHz, 10 Vpp, signal. The output from individual elements is similar, as the amplitude from the row is approximately three times greater than that from a single element.

Some initial steering tests by phasing the array were carried out. Fig. 10 shows a snapshot of the array displacement, when the elements were phased to produce 5 degree steering. The maximum pressure amplitude could successfully be shifted off-centre by small angles, but large grating lobes were present. This was expected given the relatively large element spacing, and the small number of array elements.

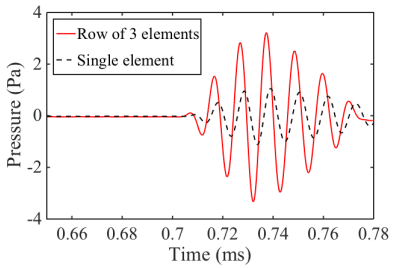

Fig. 9: Absolute pressure from a flexural array transducer.

VI. Conclusion

In conclusion, this method of making flexural transducer arrays, whereby a baffle is bonded to a single sheet of metal, shows promising results. The elements are sufficiently isolated to act as individual flexural elements, with modes similar to those of a single transducer in terms of shape and frequency. There is significant mechanical crosstalk between elements, which is a problem further research would benefit from solving.

For flexural transducers, because the element size affects the resonance frequencies, it is not feasible to maintain the $\frac{\lambda}{2}$ criteria. Hence, there will be grating lobes, as an artefact of the constructive interference at multiple angles of emission. There are techniques in terms of element placement, e.g. random arrays, which reduces the grating lobe amplitude, and which would be applicable to the the type of flexural array that has been presented.

VII. Acknowledgements

This project has received funding from Elster and the European Unions FP7 research and innovation program under Grant Agreement Number 612118. The contents of this paper are under the sole responsibility of the authors and the EU does not take any liability according to Article 29.5 of the General Model Grant Agreement.

References

[1] T.J.R. Eriksson, S.N. Ramadas and S.M. Dixon, "Experimental and Simulation Characterisation of Flexural Vibration Modes in Unimorph Ultrasound Transducers," Ultrasonics, accepted 24 Sep. 2015.

[2] A.W. Leissa, *Vibration of Plates* (U.S. Government Press, Washington, 1969), pp. 1–8.

[3] I. Ladabaum, X.C. Jin, H.T. Soh, A. Atalar and B.T. Khuri-Yakub, "Surface Micromachined Capacitive Ultrasonic Transducers," IEEE Trans. Ultrason. Ferroelectr. Freq. Control **45**, 678–690 (1998).

[4] F. Akasheh, T. Myers, J.D. Fraser, S. Bose and A. Bandyopadhyay, "Development of Piezoelectric Micromachined Ultrasonic Transducers," Sens. and Actuators, A **111**, 257–287 (2004).

[5] W. Manthey, N. Kroemer and V. Magor, "Ultrasonic Transducers and Transducer Arrays for Applications in Air," Meas. Sci. Technol. **3**, 249–261 (1992).

[6] A.S. Savoia, B. Mauti, G. Caliano and N. Lamberti, "A Low Frequency Broadband Flexural Mode Ultrasonic Transducer for Immersion Applications," in: 2014 IEEE International Ultrasonics Symposium.

Bibliography

[1] L. E. Kinsler, *Fundamentals of acoustics*. New York: Wiley, 4 ed., 2000.

[2] R. T. Beyer and S. V. Letcher, *Physical Ultrasonics*. New York: Academic Press, 1969.

[3] C. H. Stolze, "A history of the divergence theorem," *Historical Mathematics*, vol. 5, no. 4, pp. 437–442, 1978.

[4] K. F. Herzfeld and T. A. Litovitz, *Absorption and dispersion of ultrasonic waves*. London: Academic Press, 1959.

[5] J. D. N. Cheeke, *Fundamentals and applications of ultrasonic waves*. Boca Raton: CRC Press, 2012.

[6] H. Young and R. Freedman, *University physics with modern physics*. San Francisco: Pearson Education, 12 ed., 2008.

[7] G. R. Harris, "Review of transient field theory for a baffled planar piston," *Journal of the Acoustical Society of America*, vol. 70, no. 1, pp. 10–20, 1981.

[8] G. Benny, G. Hayward, and R. Chapman, "Beam profile measurements and simulations for ultrasonic transducers operating in air," *Journal of the Acoustical Society of America*, vol. 107, no. 4, pp. 2089–2100, 2000.

[9] J. D. N. Cheeke, *Fundamentals and Applications of Ultrasonic Waves*. London: Taylor & Francis, 2002.

[10] T. E. Gómez Alvarez-Arenas, "Acoustic impedance matching of piezoelectric transducers to the air.," *IEEE Transactions on Ultrasonics, Ferroelectrics and Frequency Control*, vol. 51, no. 5, pp. 624–633, 2004.

[11] T. Gomez, F. Montero de Espinosa, M. Moner-Girona, E. Rodriguez, A. Roig, E. Molins, J. Rodriguez, S. Vargas, and M. Esteves, "Low-impedance and

low-loss customized materials for air-coupled piezoelectric transducers," in *2001 IEEE International Ultrasonics Symposium*, vol. 2, pp. 1077–1080, IEEE, 2001.

[12] A. J. Mulholland, N. Ramadas, R. I. O'Leary, A. C. S. Parr, G. Hayward, A. Troge, and R. A. Pethrick, "Enhancing the performance of piezoelectric ultrasound transducers by the use of multiple matching layers," *IMA Journal of Applied Mathematics*, vol. 73, no. 6, pp. 936–949, 2008.

[13] S. Kelly, G. Hayward, and T. E. Gómez Alvarez-Arenas, "Characterization and assessment of an integrated matching layer for air-coupled ultrasonic applications," *IEEE Transaction on Ultrasonics, Ferroelectrics and Frequency Control*, vol. 51, no. 10, pp. 1314 –1323, 2004.

[14] R. E. Newnham, L. J. Bowen, K. A. Klicker, and L. E. Cross, "Composite piezoelectric transducers," *Materials and Design*, vol. 2, no. 2, pp. 93–106, 1980.

[15] G. Hayward and A. Gachagan, "An evaluation of 1-3 connectivity composite transducers for air-coupled ultrasonic applications," *Journal of the Acoustical Society of America*, vol. 99, no. 4, p. 2148, 1996.

[16] M. I. Haller and B. T. Khuri-Yakub, "Micromachined 1-3 composites for ultrasonic air transducers," *Review of Scientific Instruments*, vol. 65, no. 6, pp. 2095–2098, 1994.

[17] T. Gururaja and R. Panda, "Current Status and Future Trends in Ultrasonic Transducers for Medical Imaging Applications," *1998 IEEE International Symposium on Applications of Ferroelectrics*, pp. 223–228, 1998.

[18] Z. Xia, R. Gerhard-Multhaupt, W. Künstler, A. Wedel, and R. Danz, "High surface-charge stability of porous polytetrafluoroethylene electret films at room and elevated temperatures," *Journal of Physics D: Applied Physics*, vol. 32, no. 17, pp. L83–L85, 1999.

[19] Y. Cao, Z. Xia, G. Yuan, H. Zhang, H. Lin, and J. Zhu, "Numerical study of space charge dispersive transport in non-polar electrets," in *9th International Symposium on Electrets Proceedings*, pp. 139–144, IEEE, 1996.

[20] J. Lekkala, R. Poramo, K. Nyholm, and T. Kaikkonen, "EMF force sensor - a flexible and sensitive electret film for physiological applications," *Medical and Biological Engineering and Computing*, vol. 34, pp. 3–4, 1996.

[21] G. M. Sessler and J. Hillenbrand, "Electromechanical response of cellular electret films," *Applied Physics Letters*, vol. 75, no. 21, pp. 3405–3407, 1999.

[22] T. E. Gómez Alvarez-Arenas, "Air-coupled piezoelectric transducers with active polypropylene foam matching layers," *Sensors (Switzerland)*, vol. 13, no. 5, pp. 5996–6013, 2013.

[23] H. Kawai, "The piezoelectricity of poly (vinylidene fluoride).," *Journal of Applied Physics*, vol. 8, pp. 975–976, 1969.

[24] W. Manthey, N. Kroemer, and V. Magori, "Ultrasonic transducers and transducer arrays for applications in air," *Measurement Science and Technology*, vol. 3, no. 3, pp. 249–261, 1992.

[25] H. Wang and M. Toda, "Curved PVDF airborne transducer," *IEEE Transactions on Ultrasonics, Ferroelectrics and Frequency Control*, vol. 46, no. 6, pp. 1375–1386, 1999.

[26] M. Toda, "Cylindrical PVDF film transmitters and receivers for air ultrasound," *IEEE Transactions on Ultrasonics, Ferroelectrics and Frequency Control*, vol. 49, no. 5, pp. 626–634, 2002.

[27] I. Ladabaum, X. Jin, H. T. Soh, A. Atalar, and B. T. Khuri-Yakub, "Surface micromachined capacitive ultrasonic transducers," *IEEE Transactions on Ultrasonics, Ferroelectrics and Frequency Control*, vol. 45, no. 3, pp. 678–690, 1998.

[28] U. Demirci, A. S. Ergun, O. Oralkan, M. Karaman, and B. T. Khuri-Yakub, "Forward-viewing cmut arrays for medical imaging," *IEEE Transactions on Ultrasonics, Ferroelectrics, and Frequency Control*, vol. 51, no. 7, pp. 887–895, 2004.

[29] D. W. Schindel and D. A. Hutchins, "Applications of micromachined capacitance transducers in air-coupled ultrasonics and nondestructive evaluation," *IEEE Transactions on Ultrasonics, Ferroelectrics and Frequency Control*, vol. 42, no. 1, pp. 51–58, 1995.

[30] I. J. O'Sullivan and W. M. D. Wright, "Ultrasonic measurement of gas flow using electrostatic transducers," *Ultrasonics*, vol. 40, no. 1-8, pp. 407–411, 2002.

[31] P. C. Eccardt and K. Niederer, "Micromachined ultrasound transducers with improved coupling factors from a CMOS compatible process," *Ultrasonics*, vol. 38, no. 1, pp. 774–780, 2000.

[32] M.-C. Ho, M. Kupnik, K. K. Park, and B. T. Khuri-Yakub, "Long-term measurement results of pre-charged CMUTs with zero external bias operation," in *2012 IEEE International Ultrasonics Symposium*, pp. 89–92, IEEE, 2012.

[33] F. Akasheh, T. Myers, J. D. Fraser, S. Bose, and A. Bandyopadhyay, "Development of piezoelectric micromachined ultrasonic transducers," *Sensors Actuators, A Phys.*, vol. 111, no. 2-3, pp. 275–287, 2004.

[34] K. Smyth and S.-g. Kim, "Analytical Equivalent Circuit Model for Piezoelectric Micromachined Ultrasonic Transducers," *IEEE Transactions on Ultrasonics, Ferroelectrics and Frequency Control*, vol. 62, no. 4, pp. 744–765, 2015.

[35] C. Tan, Y. Yuan, X. Dong, and F. Dong, "Oilwater two-phase flow measurement with combined ultrasonic transducer and electrical sensors," *Measurement Science and Technology*, vol. 27, no. 12, p. 125307, 2016.

[36] L. Lynnworth and Y. Liu, "Ultrasonic flowmeters: Half-century progress report, 19552005," *Ultrasonics*, vol. 44, Supplement, pp. e1371 – e1378, 2006. Proceedings of Ultrasonics International (UI05) and World Congress on Ultrasonics (WCU).

[37] W. Wright, D. Hutchins, D. Jansen, and D. Schindel, "Air-coupled Lamb wave tomography.," *IEEE Transactions on Ultrasonics, Ferroelectrics and Frequency Control*, vol. 44, no. 1, pp. 53–9, 1997.

[38] P. A. Fomitchov, A. K. Kromin, S. Krishnaswamy, and J. D. Achenbach, "Imaging of damage in sandwich composite structures using a scanning laser source technique," *Composites Part B: Engineering*, vol. 35, no. 6-8, pp. 557–562, 2004.

[39] S. Flores and M. Vossiek, "A Robust Air-Coupled Ultrasonic Piezoelectric-Carbon-Fiber-Reinforced-Polymer Transducer for Mobile Robot Navigation," *2014 IEEE International Ultrasonics Symposium*, no. 01, pp. 858–861, 2014.

[40] T. Dahl, J. L. Ealo, H. J. Bang, S. Holm, and P. Khuri-Yakub, "Applications of airborne ultrasound in human-computer interaction," *Ultrasonics*, vol. 54, no. 7, pp. 1912–1921, 2014.

[41] T. G. Dahl, H. J. Bang, and T. Kavli, "Touchless user interfaces," 2015. European Patent EP 2956840 A1.

[42] T. L. Szabo, *Diagnostic ultrasound imaging : inside out*. Oxford: Elsevier/Academic Press, 2 ed., 2014.

[43] A. McNab and M. J. Campbell, "Ultrasonic phased arrays for nondestructive testing," *NDT International*, vol. 20, no. 6, pp. 333–337, 1987.

[44] B. W. Drinkwater and P. D. Wilcox, "Ultrasonic arrays for non-destructive evaluation: A review," *NDT and E International*, vol. 39, no. 7, pp. 525–541, 2006.

[45] S. Harput and A. Bozkurt, "Ultrasonic Phased Array Device for Acoustic Imaging in Air," *IEEE Sensors Journal*, vol. 8, no. 11, pp. 1755–1762, 2008.

[46] L. Azar, Y. Shi, and S. C. Wooh, "Beam focusing behavior of linear phased arrays," *NDT and E International*, vol. 33, no. 3, pp. 189–198, 2000.

[47] J. H. Lee and S. W. Choi, "A parametric study of ultrasonic beam profiles for a linear phased array transducer.," *IEEE Transactions on Ultrasonics, Ferroelectrics and Frequency Control*, vol. 47, no. 3, pp. 644–50, 2000.

[48] L. W. Schmerr, *Fundamentals of Ultrasonic Nondestructive Evaluation: A Modeling Approach*. Springer US, 1998.

[49] B. D. Steinberg, *Principles of aperture and array system design : including random and adaptive arrays*. New York: Wiley, 1976.

[50] W. Hendricks, "The totally random versus the bin approach for random arrays," *IEEE Transactions on Antennas and Propagation*, vol. 39, no. 12, pp. 1757–1762, 1991.

[51] O. Martínez-Graullera, C. J. Martín, G. Godoy, and L. G. Ullate, "2D array design based on Fermat spiral for ultrasound imaging.," *Ultrasonics*, vol. 50, no. 2, pp. 280–9, 2010.

[52] C. Scruby and L. Drain, *Laser Ultrasonics Techniques and Applications*. CRC Press, 1990.

[53] J.-P. Monchalin, "Optical Detection of Ultrasound," *IEEE Transactions on Ultrasonics, Ferroelectrics and Frequency Control*, vol. 33, no. 5, pp. 485–499, 1986.

[54] M. B. Klein, G. D. Bacher, A. Grunnet-Jepsen, D. Wright, and W. E. Moerner, "Homodyne detection of ultrasonic surface displacements using two-wave mixing in photorefractive polymers," *Optical Communications*, vol. 162, no. 1, pp. 79–84, 1999.

[55] C. Li, D. A. Hutchins, and R. J. Green, "Short-range ultrasonic digital communications in air," *IEEE Transactions on Ultrasonics, Ferroelectrics and Frequency Control*, vol. 55, no. 4, pp. 908–918, 2008.

[56] S. P. Kelly, R. Farlow, and G. Hayward, "Applications of through-air ultrasound for rapid NDE scanning in the aerospace industry," *IEEE Transactions on Ultrasonics, Ferroelectrics and Frequency Control*, vol. 43, no. 4, pp. 581–591, 1996.

[57] A. Gachagan and G. Hayward, "Characterization of Air-Coupled Transducers," *IEEE Transactions on Ultrasonics, Ferroelectrics and Frequency Control*, vol. 43, no. 4, pp. 678–689, 1996.

[58] G. Kirchhoff, "Über das Gleichgewicht und die Bewegung einer elastischen Scheibe.," *Journal für die reine und angewandte Mathematik*, vol. 40, pp. 51–88, 1850.

[59] J. N. Reddy, *Theory and Analysis of Elastic Plates and Shells*. CRC Press, 2 ed., 2006.

[60] A. W. Leissa, *Vibration of plates*. Washington: U.S. Government Press, 1969.

[61] G. B. Arfken, H.-J. Weber, and F. E. Harris, *Mathematical Methods for Physicists: A Comprehensive Guide*. Oxford: Academic Press, 7 ed., 2012.

[62] O. C. Zienkiewicz, R. L. Taylor, and J. Zhu, *The Finite Element Method: Its Basis and Fundamentals*. Butterworth-Heinemann, 2005.

[63] W. Heywang, K. Lubitz, and W. Wersing, *Piezoelectricity : evolution and future of a technology*. Berlin: Springer, 2008.

[64] Q.-H. Qin, *Green's Function and Boundary Elements of Multifield Materials*. Oxford: Elsevier, 1 ed., 2007.

[65] Q.-H. Qin, *Advanced mechanics of piezoelectricity*. Beijing: Higher Education Press, 2013.

[66] S. P. Timoshenko and J. N. Goodier, *Theory of elasticity*. London: McGraw Hill, 3 ed., 1970.

[67] C. Kittel, *Introduction to solid state physics*. New Jersey: John Wiley & Sons, Inc., 8 ed., 2005.

[68] J. Fialka and P. Beneš, "Comparison of methods for the piezoelectric coefficients measurement," *Control Instrumentation*, vol. 62, no. 5, pp. 1047–1057, 2013.

[69] "IEEE standard on piezoelectricity," *IEEE std*, no. 176, 1987.

[70] S. Sherrit, H. D. Wiederick, B. K. Mukherjee, and M. Sayer, "An accurate equivalent circuit for the unloaded piezoelectric vibrator in the thickness mode," *Journal of Physics D: Applied Physics*, vol. 30, no. 16, pp. 2354–2363, 1997.

[71] M. G. M. Guan and W.-H. L. W.-H. Liao, "Studies on the circuit models of piezoelectric ceramics," *2004 IEEE International Conference on Information Acquisition*, pp. 26–31, 2004.

[72] A. S. Savoia, B. Mauti, G. Caliano, and N. Lamberti, "A low frequency broadband flexural mode ultrasonic transducer for immersion applications," *2014 IEEE International Ultrasonics Symposium*, pp. 2591–2594, 2014.

[73] T. Eriksson, S. Ramadas, A. Unger, M. Hoffman, M. Kupnik, and S. Dixon, "Flexural transducer arrays for industrial non-contact applications," in *2015 IEEE International Ultrasonics Symposium*, pp. 1–4, IEEE, 2015.

[74] E. Konetzke, M. Rutsch, M. Hoffmann, A. Unger, R. Golinske, D. Killat, S. N. Ramadas, S. Dixon, and M. Kupnik, "Phased array transducer for emitting 40-kHz air-coupled ultrasound without grating lobes," in *2015 IEEE International Ultrasonics Symposium*, pp. 1–4, IEEE, 2015.

[75] T. J. R. Eriksson, M. Laws, S. M. Dixon, and S. N. Ramadas, "Air-coupled flexural electrodynamic acoustic transducers," in *2014 IEEE International Ultrasonics Symposium*, pp. 1021–1024, 2014.

[76] T. J. R. Eriksson, M. Laws, L. Kang, Y. Fan, S. N. Ramadas, and S. Dixon, "Experimental Evaluation of Three Designs of Electrodynamic Flexural Transducers," *Sensors*, vol. 16, p. 1363, 2016.

[77] M. Hirao and H. Ogi, *EMATs for Science and Industry: Noncontacting Ultrasonic Measurements*. Boston, MA: Springer US, 2003.

[78] M. Seher and R. Challis, "The electrical properties of a planar coil electromagnetic acoustic transducer and their implications for noise performance," *Measurement Science and Technology*, vol. 27, no. 2, p. 25102, 2016.

[79] N. Siakavellas, "Two simple models for analytical calculation of eddy currents in thin conducting plates," *IEEE Transactions on Magnetics*, vol. 33, no. 3, pp. 2245–2257, 1997.

[80] D. J. Griffiths, *Introduction to electrodynamics*. London: Prentice Hall, 3 ed., 1999.

[81] J. Poltz, "On eddy currents in thin plates," *Archiv für Elektrotechnik*, vol. 66, no. 4, pp. 225–229, 1983.

[82] H. Tsuboi and K. Kunisue, "Eddy current analysis of thin plates taking account of the source current distributions and its experimental verifications," *IEEE Transactions on Magnetics*, vol. 27, no. 5, pp. 4020–4023, 1991.

[83] H. Wheeler, "Formulas for the Skin Effect," *Proceeding of the IRE*, vol. 30, no. 9, pp. 412–424, 1942.

[84] K. L. McAughey, *High precision measurements for NDE using electromagnetic sensors*. PhD thesis, University of Warwick, Coventry, 2015.

[85] X. Jian, S. Dixon, R. S. Edwards, and J. Morrison, "Coupling mechanism of an EMAT," *Ultrasonics*, vol. 44, no. SUPPL., pp. 653–656, 2006.

[86] R. Ribichini, F. Cegla, P. Nagy, and P. Cawley, "Experimental and numerical evaluation of electromagnetic acoustic transducer performance on steel materials," *NDT and E International*, vol. 45, no. 1, pp. 32–38, 2012.

[87] L. Kang, S. Dixon, K. Wang, and J. Dai, "Enhancement of signal amplitude of surface wave EMATs based on 3-D simulation analysis and orthogonal test method," *NDT and E International*, vol. 59, pp. 11–17, 2013.

[88] S. Dixon, C. Edwards, and S. B. Palmer, "High accuracy non-contact ultrasonic thickness gauging of aluminium sheet using electromagnetic acoustic transducers," *Ultrasonics*, vol. 39, no. 6, pp. 445–453, 2001.

[89] B. W. Maxfield, A. Kuramoto, and J. K. Hulbert, "Evaluating EMAT designs for selected applications," *Material Evaluation*, vol. 45, no. 10, pp. 1166–1183, 1987.

[90] T. J. R. Eriksson, S. N. Ramadas, and S. M. Dixon, "Experimental and simulation characterisation of flexural vibration modes in unimorph ultrasound transducers," *Ultrasonics*, vol. 65, pp. 242–248, 2016.

[91] D. Rueter and T. Morgenstern, "Ultrasound generation with high power and coil only EMAT concepts," *Ultrasonics*, vol. 54, no. 8, pp. 2141–2150, 2014.

[92] F. Gustafsson, "Determining the initial states in forward-backward filtering," *IEEE Transactions on Signal Processing*, vol. 44, no. 4, pp. 988–992, 1996.

[93] T. Edwards, "Discrete Wavelet Transforms : Theory and Implementation," tech. rep., Stanford University, 1992.

[94] V. Matz, R. Šmíd, M. Kreidl, and C. Republic, "Comparison of De-Noising Methods used for EMAT Signals," in *European Conference on Non-Destructive Testing*, (Berlin), pp. 1–7, 2006.

[95] R. Baker, "Turbine and related flowmeters: I. Industrial practice," *Flow Measurement and Instrumentation*, vol. 2, no. 3, pp. 147–161, 1991.

[96] R. C. Baker, "Turbine flowmeters: II. Theoretical and experimental published information," *Flow Measurement and Instrumentation*, vol. 4, no. 3, pp. 123–144, 1993.

[97] J. T. Bergervoet and F. J. Oostendoys, "Flow straightener for a turbine-wheel gasmeter," 1997. US Patent 5,596,152.

[98] R. C. Baker, *Flow Measurement Handbook*. Cambridge: Cambridge University Press, 2000.

[99] B. E. Noltingk, *Instrumentation reference book*. Butterworth-Heinemann, 1995.

[100] K. O. Plache, "Coriolis gyroscopic meter," *Mech. Eng.*, vol. 101, no. 3, pp. 36 – 41, 1979.

[101] P. J. Herzl, "Coriolis-type mass flowmeter," 1986. US Patent 4,691,578.

[102] R. C. Baker, "Coriolis flowmeters: industrial practice and published information," *Flow Measurement and Instrumentation*, 1994.

[103] D. J. Acheson, *Elementary fluid dynamics*. Oxford: Clarendon Press, 1990.

[104] A. Kolin, "An Electromagnetic Flowmeter. Principle of the Method and its Application to Bloodflow Measurements," *Experimental Biology and Medicine*, vol. 35, no. 1, pp. 53–56, 1936.

[105] A. Kolin, "An A.C. Induction Flow Meter for Measurement of Blood Flow in Intact Blood Vessels," *Experimental Biology and Medicine*, vol. 46, no. 2, pp. 235–239, 1941.

[106] J. A. Shercliff, *The theory of electromagnetic flow-measurement*. Cambridge: Cambridge University Press, 1962.

[107] M. Bevir, "Theory of induced voltage electromagnetic flowmeasurement," *IEEE Transactions on Magnetics*, vol. 6, no. 2, pp. 315–320, 1970.

[108] T. Amare, "Design of an electromagnetic flowmeter for insulating liquids," *Measurement Science and Technology*, vol. 10, no. 8, pp. 755–758, 1999.

[109] D. Marioli, C. Narduzzi, C. Offelli, and D. Petri, "Digital Time-of-Flight Measurement for Ultrasonic Sensors," *IEEE Transactions on Instrumentation and Measurement*, vol. 41, no. 1, pp. 93–97, 1992.

[110] R. C. Baker, T. Wang, P. I. Moore, and A. Nurse, "Observations on the design and development of a water flow rig related to calibration in the manufacturing process," *Flow Measurement and Instrumentation*, vol. 17, no. 3, pp. 171–178, 2006.

[111] R. C. Baker, D. P. Gautrey, D. V. Mahadeva, S. D. Sennitt, and A. J. Thorne, "Case study of the electrical hardware and software for a flowmeter calibration facility," *Flow Measurement and Instrumentation*, vol. 29, pp. 9–18, 2013.

[112] J. Yang, H. Zhou, and S. Dong, "Analysis of plate piezoelectric unimorphs," *IEEE Transactions on Ultrasonics, Ferroelectrics and Frequency Control*, vol. 53, no. 2, pp. 456–462, 2006.

[113] Y. H. Y. Huang and W. H. W. Huang, "Modeling and analysis of circular flexural-vibration-mode piezoelectric transformer," *IEEE Transactions on Ultrasonics, Ferroelectrics and Frequency Control*, vol. 57, no. 12, pp. 2764–2771, 2010.

[114] Y. Huang and W. Huang, "Research on the displacement function and equivalent circuit of circular flexural vibration mode piezoelectric ceramic composite

transducers," *IEEE Transactions on Ultrasonics, Ferroelectrics and Frequency Control*, vol. 60, no. 1, pp. 218–234, 2013.

[115] S. Burrows, S. N. Ramadas, T. Eriksson, L. Kang, A. Unger, M. Kupnik, and S. Dixon, "High temperature flexural ultrasonic transducer for non-contact measurement applications," in *2015 IEEE International Symposium on Applications of Ferroelectrics, International Symposium on Integrated Functionalities, Piezoelectric Force Microscopy Work*, (Darmstadt), IEEE, 2016.